

AD-A279 849



DTIC  
ELECTE  
MAY 31 1994  
S F D

ALT'93

International Symposium on  
Advanced Laser Technologies

November 8 - 13, 1993  
Prague, Czech Republic

DAJA 45-93-M-0461

Selected Papers

This document has been approved  
for public release and sale; its  
distribution is unlimited

1388 94-16144

94 5 27 104

## Session 1.

Laser-stimulated processes  
in media and at interfaces.

|                    |                                     |
|--------------------|-------------------------------------|
| Accession For      |                                     |
| NTIS CRA&I         | <input checked="" type="checkbox"/> |
| DTIC TAB           | <input type="checkbox"/>            |
| Unannounced        | <input type="checkbox"/>            |
| Justification      |                                     |
| By <i>form 50</i>  |                                     |
| Distribution       |                                     |
| Availability Codes |                                     |
| Dist               | Avail and/or Special                |
| <i>A-1</i>         |                                     |

# Laser-annealing of thin semiconductor films

J.Boneberg, J.Nedelcu, E.Bucher, P.Leiderer  
Universität Konstanz, 78464 Konstanz, Germany

## ABSTRACT

Optical reflectivity and transmissivity measurements have been used to investigate the dynamics of melting and recrystallisation of thin films of Si and Ge after laser-annealing with a ns Nd:YAG-laser pulse. We report on temperature dependent changes of the reflectivity of the liquid phase above and below the melting point and on various nucleation and solidification scenarios in thin films, depending on the energy density of the annealing laser.

## 1. INTRODUCTION

The interaction of semiconductor surfaces with intense laser radiation is a long-standing topic, which has led to a number of interesting phenomena. In particular, the melting and subsequent resolidification of a thin surface layer on bulk semiconductors has been investigated in detail.<sup>1,2</sup> One aim of this "laser annealing" procedure was to remove defects in the crystal structure of the semiconductor introduced, e.g., by ion implantation. Apart from this application, the processes occurring during the rapid temperature quench of a thin liquid layer are interesting also from the fundamental point of view, for example with respect to the processes which limit the velocity of crystal growth.

In this work we report on laser-induced melting and solidification of thin films of Si and Ge, investigated by optical reflection and transmission measurements with nanosecond time resolution. The intention was to study the liquid phase at temperatures above the melting point  $T_m$ , as well as the dynamics of nucleation of crystallites from the melt and the formation of metastable phases, such as amorphous Si. Laser annealing experiments allow to achieve very high cooling rates ( $dT/dt \geq 10^{10}$  K/s) and large supercooling of the liquid phase down to temperatures of the order of  $T_m/2$ , and thus make experimental ranges accessible which by other means are difficult to reach.<sup>3</sup>

Optical measurements appear very suitable for these studies, because the reflection and transmission properties differ strongly between the respective phases, and in addition in each phase also depend on the temperature. Starting from crystalline Si at 300 K, e.g., the reflection coefficient  $R$  (at  $\lambda = 632.8$  nm and perpendicular incidence) increases from 36% to a value of 42% at the melting temperature  $T_m = 1680$  K. Upon the appearance of the liquid phase, which is metallic,  $R$  jumps up to 70%, and then slowly decreases again as the temperature is raised further.<sup>4</sup> For thin films additional temperature dependences of  $R$  appear as a result of the interference of light reflected from the film surface and the interface between film and substrate.

## 2. LIQUID PHASE

In the experiments to be described here the semiconductor surfaces were irradiated with the light of a pulsed Nd:YAG laser operating in the frequency doubled mode ( $\lambda = 532 \text{ nm}$ ) at a pulse width of 5 ns and energies up to 100 mJ per pulse.

We present first some results for the surface of bulk semiconductors. Fig. 1a shows a snapshot of a circular patch of liquid Si, molten by the Nd:YAG laser beam, taken at a time  $t = 30 \text{ ns}$  after the laser pulse. The liquid phase appears bright here, due to its higher reflectivity. In order to obtain this picture, part of the incident Nd:YAG beam was split off, passed through a delay line and shifted in frequency by means of stimulated Raman scattering (see Fig. 1b). This light was then guided at the sample surface, where it was reflected and, after passing through an color filter which rejected the stray light of the high intensity primary beam, recorded by a video camera. The time evolution of the molten spot can in this way be monitored by varying the delay line of the probe pulse for successive pulses. The temporal resolution of the snapshot, given by the length of the probe pulse, was 5 ns.

*Fig. 1a: ns-photograph of a laser-molten Si layer on bulk Si. The picture was taken 30 ns after the primary pulse.*

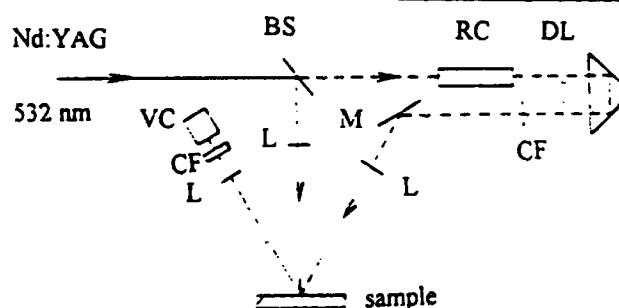
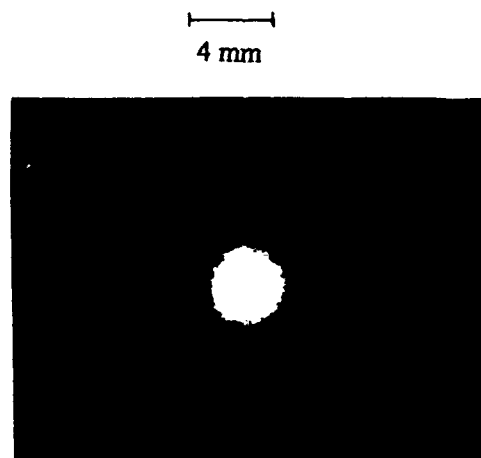


*Fig. 1b: Experimental set-up for ns photography*

|                  |                |                  |
|------------------|----------------|------------------|
| BS: beamsplitter | RC: Raman cell | DL: delay line   |
| VC: video camera | M: mirror      | L: lens          |
|                  |                | CF: color filter |

Since in the following we are mainly interested in the processes at the centre of the primary beam, we show results obtained with a slightly modified set-up (Fig.2). The probe beam is now supplied by a low power cw-laser, focussed to a diameter of  $10\text{ }\mu\text{m}$ , much smaller than the size of the primary beam of typically  $0.5\text{ mm}$ . The specularly reflected light at the wavelength  $633\text{ nm}$  was detected by a pin diode (risetime  $< 1\text{ ns}$ ) and registered by a fast digital storage oscilloscope (HP54111D). In order to obtain as much information as possible from each laser pulse, we used in general several probe lasers at various wavelengths simultaneously, all focussed to the same spot and diameter. Moreover in the case of thin film samples we measured in addition to the reflectivity of the surface (henceforth designated as  $R_s$ ) also the reflectivity of the film-substrate interface  $R_i$ , and the transmissivity of the sample. Interference filters in front of the pin diodes suppressed contributions of the Nd:YAG light to the measured signals.

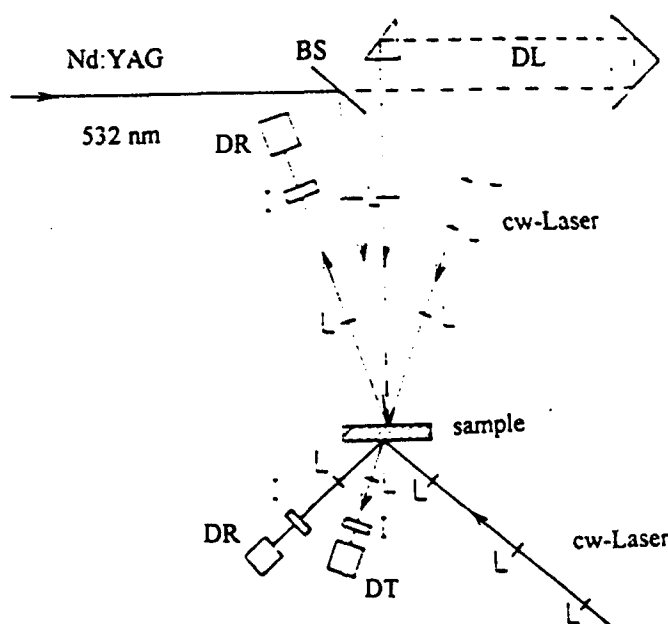


Fig.2: Experimental set-up for the time-resolved reflectivity and transmissivity experiments

BS: beam splitter      DT: diode for transmission      L: lens  
I: interference filter      DR: diode for reflection      DL: delay line

## 2.1 SINGLE PULSE EXPERIMENTS

Fig.3 shows the time-resolved reflectivity  $R_s$  for the wavelength  $633\text{ nm}$  during laser-annealing of bulk Si and Ge with different energy densities of the pulse laser. Upon melting of the surface a drastic increase of the reflectivity is observed, indicating the change from the semiconducting solid to the

metallic liquid phase. As long as a liquid layer with a thickness larger than approximately two times the absorption length ( $d_{ab} \approx 10 \text{ nm}$ )<sup>5</sup> exists at the surface the reflectivity remains constant at the high metallic value. After solidification  $R$  decreases on a  $\mu\text{s}$ -timescale towards the starting point as the temperature drops.

Using such measurements we can obtain the melting time (the duration of the high reflectivity phase) for different energy densities (Fig.4). This measurement can be compared with the results of heat flow calculations based on the finite difference method.<sup>6</sup> Fig.4 shows excellent agreement between our calculation (solid line in Fig.4) and experiment as long as the energy density of the laser pulse is below  $1.2 \text{ J/cm}^2$ . At higher energy densities the calculation leads to systematically smaller melting times (see below). This deviation at higher energy densities suggests that there may be a temperature effect on the reflectivity properties of the liquid. We have therefore examined the temperature dependence of  $R_S$  using the double pulse experiment, discussed in the following chapter.

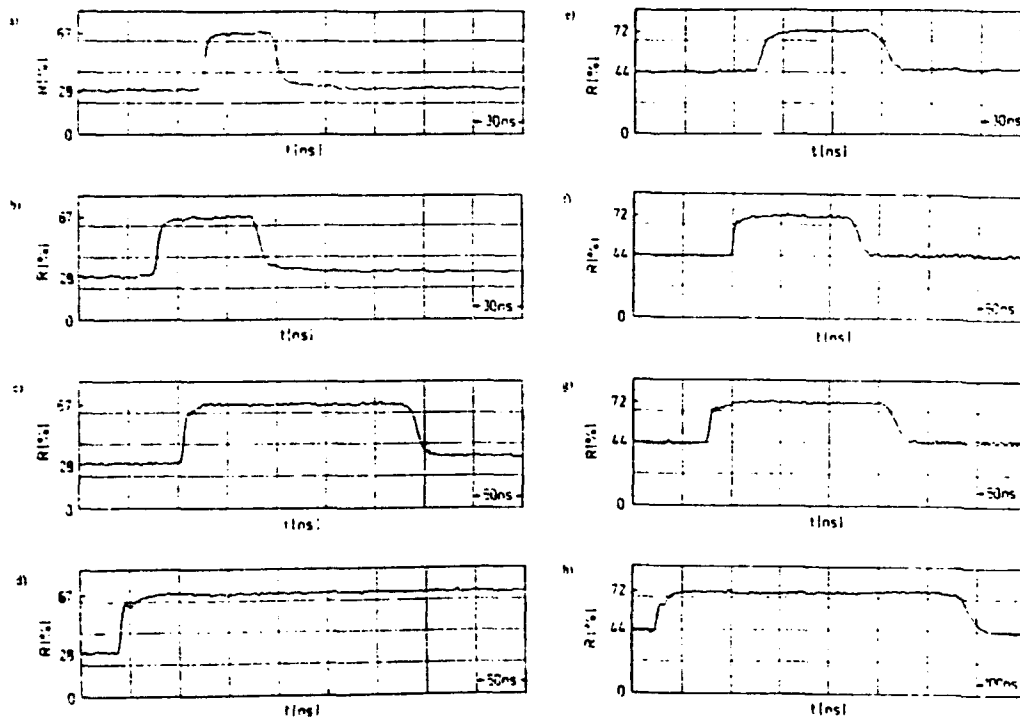


Fig.3: Time-resolved reflectivity  $R_S$  ( $\lambda = 633 \text{ nm}$ ) at different energy densities:  
target: Si    a)  $0.9 \text{ J/cm}^2$    b)  $1.0 \text{ J/cm}^2$    c)  $2.0 \text{ J/cm}^2$    d)  $2.3 \text{ J/cm}^2$   
          Ge    e)  $0.6 \text{ J/cm}^2$    f)  $0.75 \text{ J/cm}^2$    g)  $0.9 \text{ J/cm}^2$    h)  $1.3 \text{ J/cm}^2$

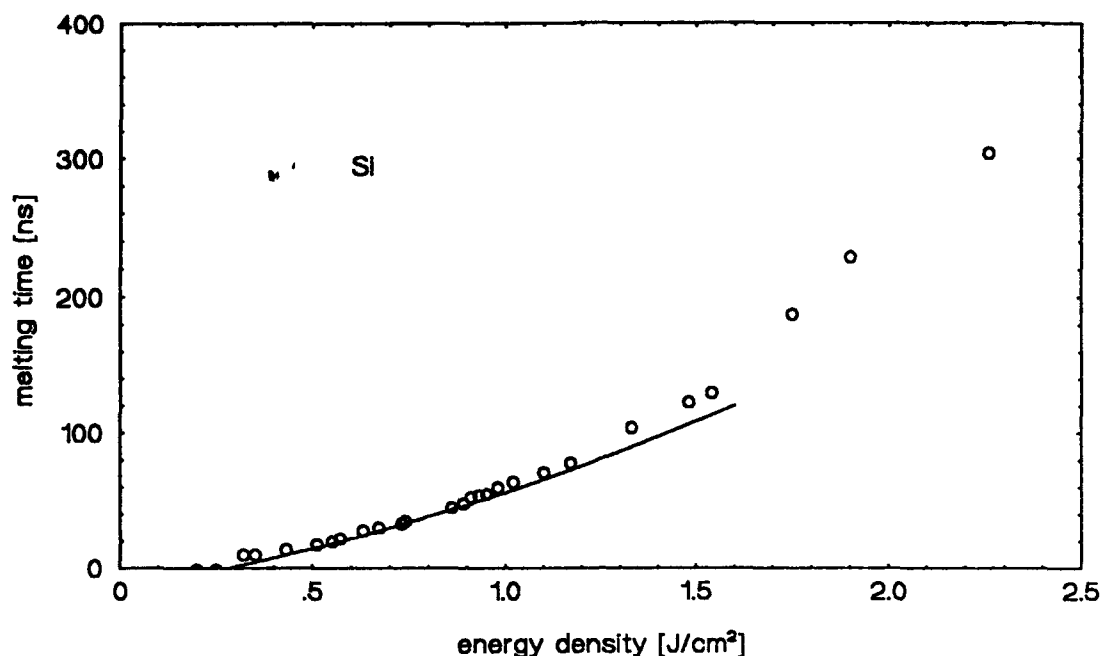


Fig.4: Melting time of Si as function of the energy density of the annealing laser  
solid line: calculated      circles: measured

## 2.2 DOUBLE PULSE EXPERIMENT

In principle, information about the laser-induced change of the surface temperature and reflectivity in the liquid state can be obtained from single pulse experiments. However, the double pulse measurements described here are interpreted more readily: The leading pulse generates a molten layer thick compared to the penetration depth of the laser light, so that the second pulse - which is the one to be analyzed in detail - is absorbed under well-defined conditions. Moreover, the effects due to heating the liquid surface are relatively subtle and thus in a single pulse experiment are easily obscured by the huge change in the reflectivity upon melting. By contrast, in a double pulse experiment these two processes are well separated, since the second pulse arrives with a delay of several ten ns.

In the examples given below for Si the energy density of the first pulse was held fixed at  $E_1 = 1.0 \text{ J/cm}^2$ , whereas the energy density of the delayed pulse was varied. In Fig.5a-d four reflectivity curves  $R_s$  are plotted for  $E_2 = 0, 0.5, 1.4$ , and  $1.8 \text{ J/cm}^2$ , respectively. Fig.5a, which represents the

effect of laser heating by the first pulse alone, shows that at the given energy density a molten layer is created which exists for 55 ns, in good agreement with previous work<sup>2</sup>. In the trace of Fig.5b, the reflectivity appears not to be affected within the experimental resolution as the delayed pulse (whose position is marked by an arrow) hits the surface. Nevertheless, the additional energy input due to the second pulse manifests itself in an increased lifetime of the high reflectivity liquid phase, 125 ns in this case. As the energy of the second pulse is further increased, however, the heating of the liquid surface leads to a clearly discernible dip in the reflectivity (e.g.  $\Delta R = 3.4\%$  at  $E_2 = 1.4 \text{ J/cm}^2$  in Fig.5c). This dip becomes even more pronounced at higher energies, reaching  $\Delta R = 9\%$  at  $E_2 = 1.8 \text{ J/cm}^2$  (Fig.5d). Similar results have been found for Ge.

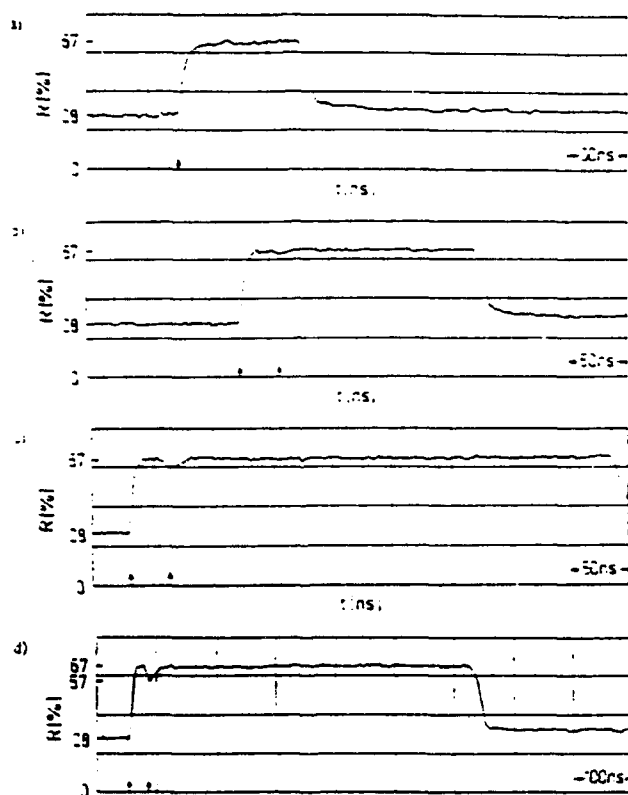


Fig.5: Time-resolved reflectivity  $R_s$  ( $\lambda = 633 \text{ nm}$ ) of Si in double pulse experiments  
 $I_1 = 1.0 \text{ J/cm}^2$  in all cases,  $I_2 = 0.0 \text{ J/cm}^2$  (a),  $0.9 \text{ J/cm}^2$  (b),  $1.5 \text{ J/cm}^2$  (c),  $1.9 \text{ J/cm}^2$  (d)  
 Laser pulses are marked by arrows



Using both the results from the heat diffusion calculation and the energy dependence we can infer the temperature effect on the reflectivity of liquid Si (Fig.6). As it appears Si in the molten state does not behave like a simple Drude metal; the data suggest that the density of free electrons, respectively the plasma frequency, is not constant but increases with temperature (for details see Ref.7).

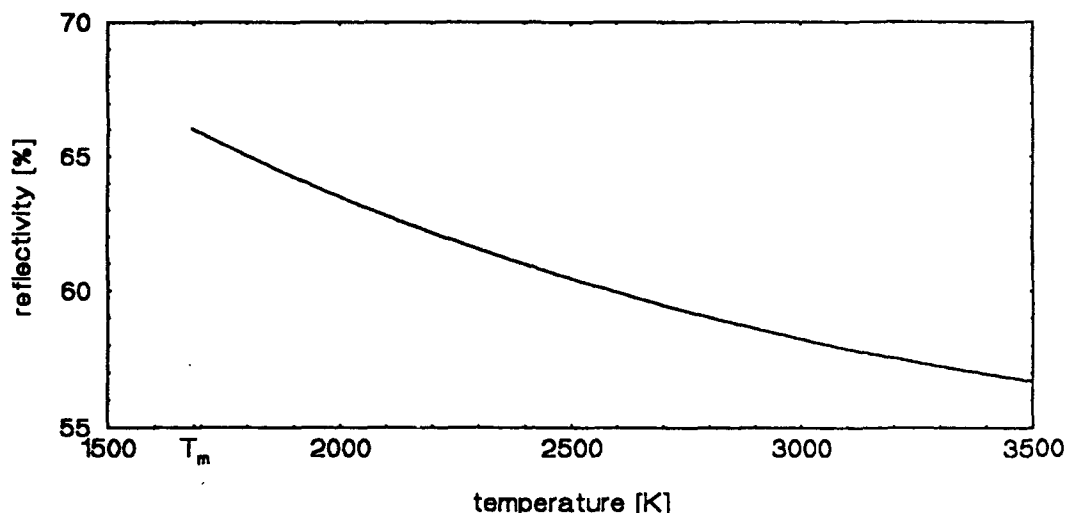


Fig.6: Calculated reflectivity ( $\lambda = 633$  nm) of liquid Si above the melting point  $T_m$  as a function of temperature

The decrease of the reflectivity with increasing temperature explains the discrepancy between heat flow calculations and measurements (Fig.4): At higher energy densities the temperature of the surface increases considerable, the reflectivity drops and therefore the absorption and the melting time increase.

We want to point out an observation at even higher temperatures which might be interpreted as a metal-insulator transition in liquid Si.<sup>8</sup> In these measurements, which have been made with *thin Si films* (cf. part3), the reflectivity and transmissivity were determined simultaneously at two probe wavelengths 633 nm and 488 nm. While at energy densities discussed so far the reflectivity remained at a high value upon melting (cf. Fig.10), it is observed in Fig.7 that at even higher energy density the reflectivity drops below 10% after a quick increase up to the reflectivity of the molten Si. The transmissivity, on the other hand, which had been zero in the liquid phase for the measurements at lower energy densities, now increases above 90%. Thus the film in this state behaves rather as a transparent dielectric than a liquid metal. This behavior might result from thermal expansion upon heating, and is in line with a metal-insulator transition at sufficiently small electron densities.

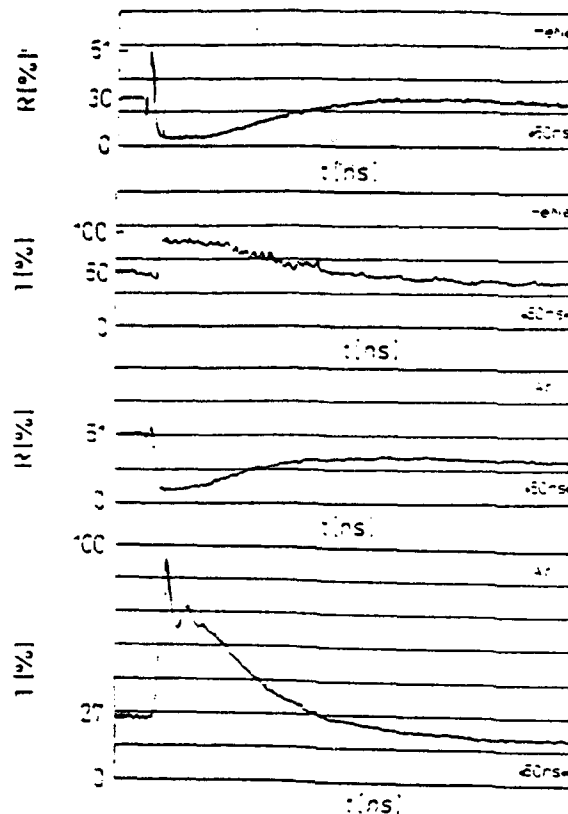


Fig.7: Time-resolved reflectivity and transmissivity ( $\lambda = 633 \text{ nm}$  and  $488 \text{ nm}$ ) of a thin Si-film ( $d = 125 \text{ nm}$ ) on a quartz glass substrate at an energy density of  $400 \text{ mJ/cm}^2$

### 3. SOLIDIFICATION SCENARIOS ON THIN SI-FILMS

The samples used here were polycrystalline Si films with a thickness of  $125 \text{ nm}$  on  $1 \text{ mm}$  quartz glass substrates. The experimental results can be divided into three regimes, depending on the energy density of the annealing-laser: 3.1) heating without melting, 3.2) partial melting and 3.3) complete melting of the Si film.

#### 3.1 HEATING OF THE SOLID PHASE

As long as the energy density of the annealing laser pulse is sufficiently low ( $E < E_{\text{thres}} = 170 \text{ mJ/cm}^2$ ) the film does not melt. In the experimental curve shown in Fig.8 the energy density of the laser pulse is just below  $E_{\text{thres}}$ . The surface reflectivity  $R_s$  decreases from  $70\%$  to  $30\%$  and the reflectivity

on the substrate side  $R_i$  decreases from 50% to 40% during the laser pulse. Both increase back to the starting value on a time scale of 200 ns. The observed reflectivity changes are due to an interference effect in the thin film and can be interpreted by means of the temperature dependence of the optical constants of crystalline Si.<sup>10,11</sup> Calculations of the reflectivity from thin film optics agree very well with the observed reflectivity changes.

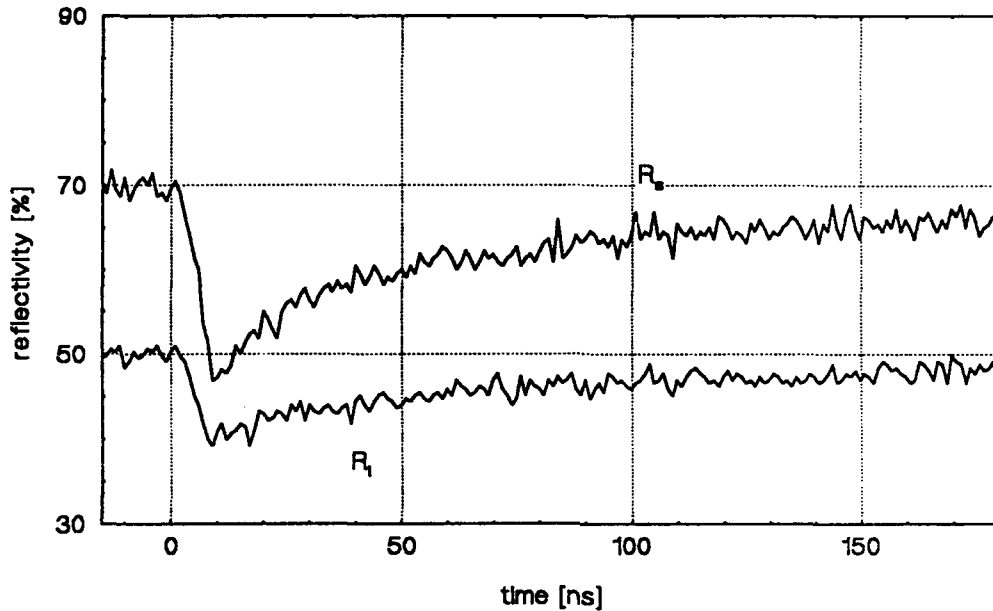


Fig.8: Time-resolved reflectivity ( $R_s$  at 633 nm and  $R_i$  at 488nm) of a thin Si film ( $d = 125$  nm) at an energy density of  $I=160$  mJ/cm<sup>2</sup>, just below the threshold of melting

### 3.2 PARTIAL MELTING OF THE SI-FILM

As the energy density is increased above  $E_{thres}$  a surface layer of the Si-film is melted. The surface reflectivity  $R_s$  (Fig.9) shows first a decrease and then rises to a plateau value during the laser pulse. For several ns  $R_s$  is constant then before it decreases once again. Afterwards  $R_s$  relaxes back to the starting value. This behavior is easily interpreted:  $R_s$  decreases first with increasing temperature as we have seen in 3.1. Upon melting the reflectivity rises to the reflectivity of liquid Si.  $R_s$  is then constant as long as a liquid layer is present at the surface with a thickness  $d_l \geq 2 d_{ab}$ . With further decreasing thickness of the liquid layer  $R_s$  decreases to the reflectivity of the hot solid Si near the melting point as shown in the previous chapter.

The reflectivity of the substrate interface  $R_i$  decreases first as the layer is heated as shown in 3.1. As the boundary liquid-solid approaches the substrate  $R_i$  increases until a maximum value is reached. From the fact that the reflectivity of liquid Si is not reached one can conclude that a thin layer of Si next to the interface was not melted. The solidification proceeds from the unmelted Si layer towards the surface and  $R_i$  approaches the value of hot solid Si at the melting point.

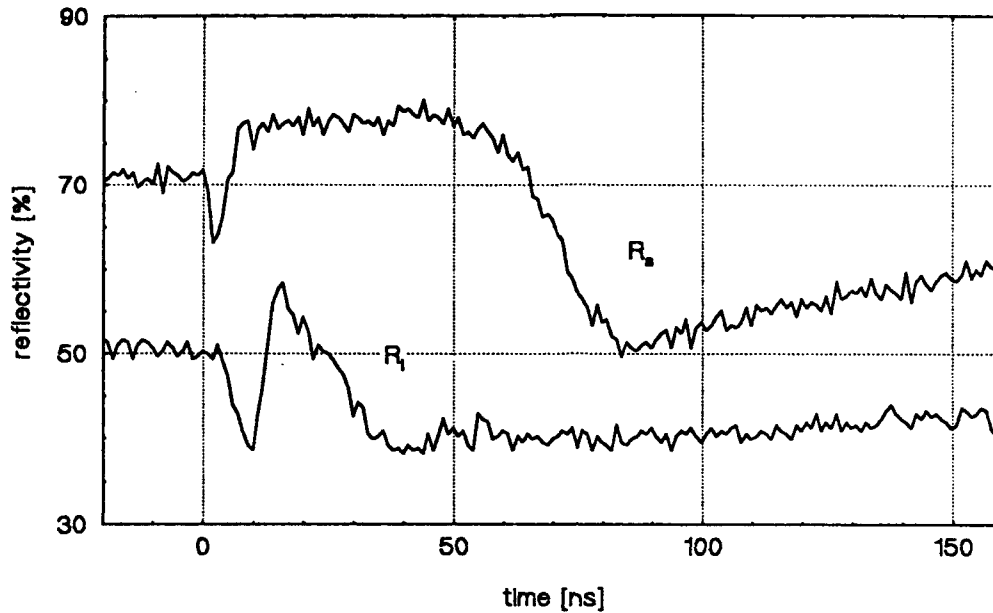


Fig.9: Time-resolved reflectivity ( $R_s$  at 633 nm and  $R_i$  at 488nm) of a thin Si film ( $d = 125$  nm) at an energy density  $I = 240$  mJ/cm<sup>2</sup>

### 3.3 COMPLETE MELTING OF THE SI-FILM

Upon complete melting of the Si film the solidification scenario changes from heterogeneous nucleation and solidification starting from the liquid-solid interface, as outlined above, towards homogeneous nucleation in the supercooled liquid. We start the discussion of the homogeneous nucleation phenomena with the highest energy density that we used in this experiment:

Fig.10 shows the reflectivity curves for an energy density 360 mJ/cm<sup>2</sup>. Compared to Fig.9  $R_s(t)$  exhibits an additional very pronounced feature. Between the plateau that we related to the liquid Si surface and the region where the solid Si cools down there exists a second plateau with a reflectivity below the value of liquid Si. Moreover the  $R_i$  curve now displays a region (between  $t = 20$  and 70 ns) where the reflectivity is nearly constant.

Stiffler and Thompson<sup>3</sup> proposed the following model for this behavior: During the first plateau the liquid Si cools down to a temperature several hundred degrees below the melting point. Homogeneous nucleation throughout the film initiates solidification and therefore a decrease in the reflectivity. The latent heat released upon solidification raises the temperature towards the melting point, where further solidification is stopped. The layer consists now of solid Si in a liquid matrix and has a reflectivity which is smaller than the reflectivity of liquid Si alone. The complete solidification proceeds then from the substrate towards the surface.  $R_s$  therefore shows a second plateau, until the complete solidification reaches the surface layer.

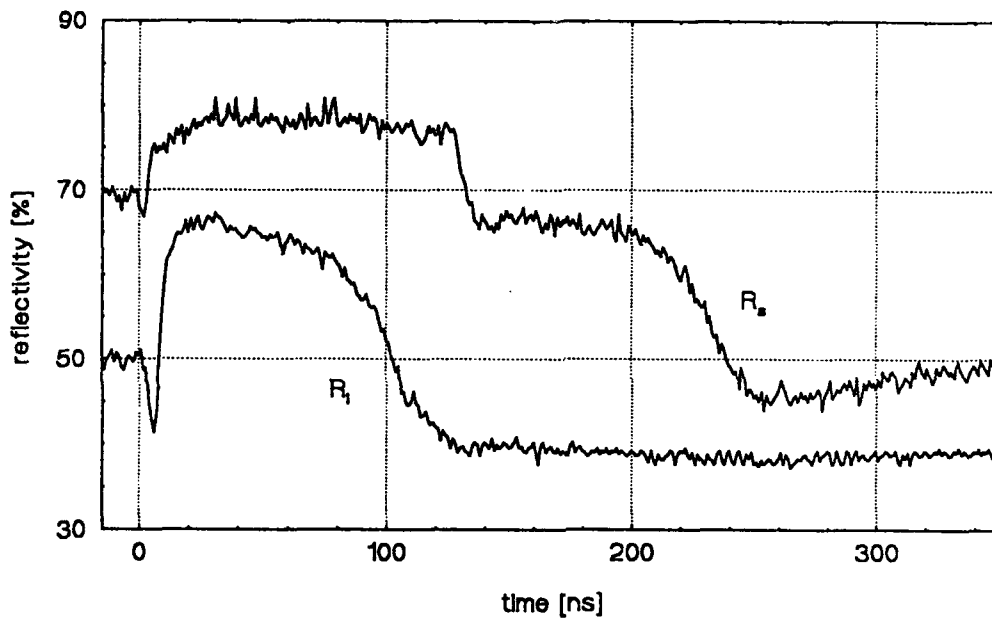


Fig.10: Time-resolved reflectivity ( $R_s$  at 633 nm and  $R_i$  at 488 nm) on a thin Si film ( $d = 125$  nm) at the energy density  $I = 360$  mJ/cm<sup>2</sup>

This model of Stiffler and Thompson is in good accord with the  $R_s$  curve in Fig.10. Yet additional information is obtained from our simultaneous measurement of  $R_i$ . The steep decrease of  $R_i$  occurs about 25 ns earlier than the decrease of  $R_s$ . One can conclude that the homogeneous nucleation and solidification proceeds from the substrate towards the surface. Furthermore there is no second plateau in  $R_i$ , indicating that solidification at the substrate side is completed in one step. From the result that the solidification at the surface is a two-step process we get the information that during the partial solidification a gradient in the solidified volume exists across the layer.

We will now return to smaller energy densities until we reach  $E_{compl}$ , where the thin film is just melted completely. In terms of supercooling this procedure means that we increase the supercooling now: The highest quenchrates - and therefore supercoolings - are achievable at the highest heat fluxes into the substrate. As the heat flux into the substrate decreases with time, caused by the decrease of the temperature gradient, somewhat surprisingly the smallest energy density ( $E_{compl}$ ) yields the maximum supercooling. A calculation based on heat flux considerations yields values well beyond 500 K for the maximum supercooling achieved in our experiments.

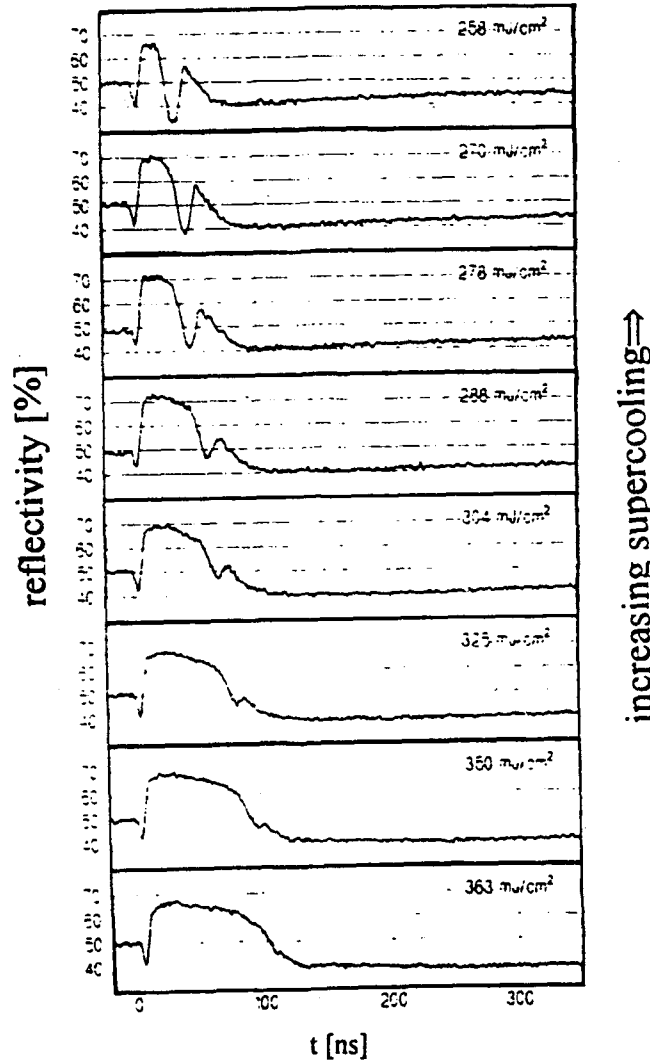


Fig.11: Time-resolved reflectivity ( $R_i$  at 488nm) of a thin Si-film ( $d = 125$  nm). Decreasing energy density corresponds to increasing supercooling

From thermodynamical reasons at high supercooling the nucleation of crystalline as well as the nucleation of amorphous Si is possible.<sup>3</sup> Upon proceeding to larger undercooling an additional peak arises in the  $R_i$  curves (Fig. 11). In our interpretation this peak is connected with a transient formation of amorphous Si. As the temperature of the Si layer is raised above the melting point of amorphous Si  $T_{m,a}$  (1435 K)<sup>3</sup> amorphous regions are melted and  $R_i$  increases. Upon crystallisation  $R_i$  decreases once again. The optical properties of the Si layer at room temperature after the annealing process does not show any change which could be attributed to the *permanent* formation of amorphous Si. This observation is in agreement with the measurements of Sameshima and Usui<sup>12</sup> who found permanent amorphisation only at film thicknesses below 18 nm.

The  $R_s$  curves show the effect of remelting as well, but in somewhat modified form: The remelting does not increase continuously with the supercooling. We suppose that the latent heat released upon nucleation on the substrate side alters the nucleation on the surface side, which always takes place some tens of ns later.

Regarding the temperature dependence of the reflectivity the measurements on thin liquid Si films confirm the observation of part 2: At the end of the laser pulse the temperature of the liquid reaches its maximum. As the temperature decreases the reflectivity increases (cf.  $R_s$  in Fig. 10 between  $t = 5$  and 35 ns). During the following undercooling no further increase of  $R_s$  can be observed (cf.  $R_s$  in Fig. 10 between  $t = 35$  and 120 ns). On the contrary  $R_s$  decreases again in contrast to the expectations of a simple Drude-metal (a similar feature can be found in the conductivity of liquid Si<sup>9</sup>). This behavior can be understood if one assumes (as we already did in part 2 and in Ref. 7) that, apart from a temperature dependent change of the collision frequency, the density of the free electrons in the melt is temperature dependent as well: The density of free electrons is decreasing with decreasing temperature. This change of the electron density becomes the dominant effect at temperatures below the melting temperature. As a result  $R(T)$  has a maximum at temperatures around the melting point.

#### 4.SUMMARY

In summary we have shown that liquid Si and Ge show temperature dependent optical properties, which have to be considered in model calculations of the heat balance in laser-annealing. The temperature dependence of the optical properties is not given by a simple Drude behavior but has an additional contribution of a the temperature dependent change of the electron density. At high temperatures we observe an optical behavior, which suggests a metal - insulator transition in the liquid.

Concerning the solidification phenomena we have shown that the simultaneous measurement of the reflectivity from the surface and the substrate side gives comprehensive information about nucleation and solidification in thin films. Regions of heterogeneous and homogeneous nucleation as well as transient amorphisation and the influence of the temperature gradient across the film could be resolved.

## 5.ACKNOWLEDGEMENTS

We would like to thank M.O.Thompson for a day of stimulating discussion and for providing a preprint of his recent work prior to publication. This work was supported by Zentrum II für Energieforschung at the University of Konstanz.

## 6.REFERENCES

1. J.M.Poate Laser Annealing of Semiconductors, Academic Press, New York, 1982
2. D.H.Auston, J.A.Golovchenko, A.L.Simons, R.E.Slusher, P.R.Smith, C.M.Surko, and T.N.C.Venkatesan, Dynamics of Laser Annealing, Laser Solid Interactions and Laser Processing, AIP, New York, 1979
3. S.R.Stiffler, M.O.Thompson, P.S.Peercy, "Supercooling and Nucleation of Silicon after Laser Melting", *Phys.Rev.Lett.*, vol.60,24, pp. 2519-2522, 1988
4. M.O.Lampert, J.M.Koebel, P.Siffert, "Temperature dependence of the reflectance of solid and liquid silicon", *J.Appl.Phys.*, vol.52,8, pp. 4975-4976, 1981
5. G.E.Jellison, Jr. and D.H.Lowndes, "Measurements of the Optical Properties of Liquid Silicon and Germanium Using Nanosecond Time-Resolved Ellipsometry", *Appl.Phys.Lett.*, vol.51,5, pp. 352-354, 1987
6. P.Baeri, S.U.Campisano, G.Foti, and E.Rimini, "A Melting Model for Pulsing-Laser Annealing of Implanted Semiconductors", *Appl.Phys.*, vol 50,2, pp. 788-797, 1979
7. J.Boneberg, O.Yavas, B.Mierswa, P.Leiderer, "Optical Reflectivity of Si above the Melting Point", *phys.stat.sol.(b)*, vol.174, pp.295-300, 1992
8. V.A.Batanov, F.V.Bunkin, A.M.Prokhorov, V.B.Fedorov, "Evaporation of metallic targets caused by intense optical radiation", *Soviet Physics JETP*, vol.36,2, pp.311-322, 1973
9. M.J.Uttormark, M.O.Thompson, S.R.Stiffler, P.S.Peercy, "Conductance of Undercooled Liquid Silicon", unpublished
10. K.Murakami, K.Takita, K.Masuda, "Measurement of Lattice Temperature during Pulsed-Laser Annealing by Time-Dependent Optical Reflectivity", *Jap.J.Appl.Phys.*, vol.20,12, pp.L867-870, 1981
11. G.E.Jellison, Jr. and F.A.Modine, "Optical absorption of silicon between 1.6 and 4.6 eV at elevated temperatures", *Appl.Phys.Lett.*, vol.41,2, pp.180-182, 1982
12. T.Sameshima, S.Usui, "Pulsed laser-induced amorphization of silicon films", *J.Appl.Phys.*, vol.70,3, pp.1281-1289, 1991



## Resonance photodesorption of atoms from a surface of solids

A.M.Bonch-Bruevich, S.G.Przhibelskii, and V.V.Khromov

S.I.Vavilov All-Russian Research Center, St-Petersburg, Russia

### ABSTRACT

The principal experimental data are reported and the models are developed for the photodesorption of alkali atoms from a surface of transparent dielectrics and for their photodetachment from own metals.

### 1. RESONANCE PHOTODESORPTION FROM A SURFACE OF SAPPHIRE

#### 1.1. Introduction

It should be noted that despite the rich history of the photodesorption studies the simplest one-electron atomic system on the surface of transparent dielectric has not been studied yet. Nevertheless, this system is attractive in many respects. First, it is the simplest system, in which photodesorption of atoms is similar to photodissociation of molecules in a gas, the process extensively studied and often referred to when the results of atoms' photodesorption studies are analyzed. Second, the presence of strong desorbed atoms' absorption lines allows to use simple available highly-sensitive optic methods of their detection.

We have studied the desorption of alkali atoms, mostly of sodium atoms, from a single crystalline sapphire surface, which is chemically inactive to atomic vapors and transparent in the atomic absorption region.<sup>1-3</sup> Most of experiments were performed under the conditions of dynamic equilibrium between the gas and adsorbed atomic phases.

Sodium atoms desorbed by optical radiation were detected by their luminescence excited by continuous radiation of a dye laser in the region of the resonance  $3S - 3P$  transition or by absorption of probing laser light propagated parallel to the surface. The sensitivity of the recording scheme,  $10^4 - 10^5 \text{ cm}^{-3}$ , allowed measurements with a single shot of the desorbing laser. In addition, sufficiently high temporal resolution,  $10^{-8}$  sec, and recording the absorption and luminescence signals at a controllable distances from the surface made it possible to measure not only the efficiency but the photodesorption kinetic properties (time-of-flight spectra) as well.

#### 1.2. Experimental results

Measurements of the absorption spectrum of sodium atoms adsorbed on sapphire showed sodium to be adsorbed in the atomic rather than in the molecular<sub>2</sub> form, with the atom itself considerably retaining its individuality, namely, its valence electron

being strongly disturbed by the sapphire surface remains to be localized near the ionic core. It reveals from the fact that though its resonance line in the course of adsorption broadens into a comparatively wide,  $2000\text{ cm}^{-1}$ , structureless band, which center,  $645\text{ nm}$ , is shifted towards the long-wave spectral region with the respect to the free atomic line, the adsorption crosssection in the band center is  $3 \cdot 10^{-16}\text{ cm}^2$  and the crosssection integrated over the spectrum is close to that of free atom (see Fig.1). The experimental adsorption energies were found to be  $0.6$  and  $0.7\text{ eV}$  for sodium and cesium atoms, respectively, which considerably exceeds the usual values for physical adsorption. At small values of the surface coverage, the surface atomic concentration  $N$  can be well approximated by the Langmuir formula

$$N = R N_0 \exp E/kT$$

where  $N_0$  is the volume atomic concentration,  $R$  is the characteristic size of the atom-surface interaction region, and  $E$  is the adsorption energy. When volume concentration of atoms increases, the surface atomic concentration undergoes saturation without reaching the limiting value which corresponds to close packing. During this process no molecular form is observed on the surface. Both mentioned circumstances make us assume that, first, the atoms in high concentrations undergo a rather strong lateral interaction (which prevents formation of molecules), and, second, the crystal surface is not all uniform. Only its smaller,  $10\%$ , part is able to adsorb atoms with the adsorption energy  $0.6 - 0.7\text{ eV}$  revealed in the experiment. This result is in good agreement with the well-known fact about the higher energies of gold atoms adsorbed on the step boundaries and on dislocations of  $\text{NaCl}$  surface. In addition, comparison of interatomic distance,  $5\text{ a.u.}$ , in a sapphire lattice and average diameter of radial wave functions of the sodium atom  $S$ -ground and  $P$ -excited states ( $8.4$  and  $12\text{ a.u.}$ , respectively) shows that the interaction between them has a significantly many-particle character. Note, that we have also observed on the sapphire surface a chemical<sup>5</sup> form of  $\text{Na}$  atom adsorption with the adsorption energy  $2.4\text{ eV}$ . We explain it by the anion vacancies present on the surface;

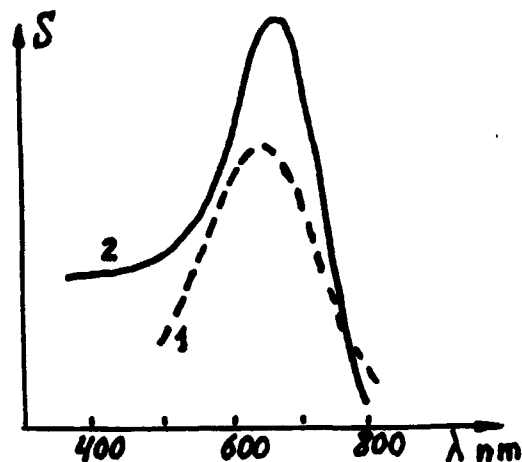


Fig.1. The absorption (1) and photodesorption (2) spectra of sodium atoms adsorbed on sapphire.

their concentration is rather low and does not exceed  $10^{10} - 10^{11}$   $\text{cm}^{-2}$ .

As stated in Ref.2, excitation of adsorbed atom by optical radiation results in its small probability desorption (with quantum yield being equal  $10^{-3}$  and  $10^{-5}$  for sodium and cesium atoms, respectively) with its kinetic energy considerably exceeding the thermal surface energy, but making only a small part of the desorbing photon energy. The velocity distribution of atoms escaping the surface was found to be close to that of Maxwellian with the effective temperature proportional to the energy of desorbed photons, not depending on the incident radiation flux density (see Fig.2).

The positions of maxima and the widths of the photodesorption spectrum are similar to those of the adsorbed atoms' absorption spectrum; certain distinctions between them occur only in the UV, where the photodesorption efficiency does not change (Fig.1).

By the kinetic measurements of surface adatoms' concentration disturbed by the intense optical radiation, we determined the sticking coefficient,  $10^{-2}$ , of atoms impacting the surface, and the rate of the vibration energy transfer from the adsorbed atom to the substrate (the value of the Langmuir frequency factor is  $10^{11} \text{ sec}^{-1}$ ). We have also estimated for surface diffusion process the value, 0.1 eV, of the activation energy.

### 1.3 Model of photodesorption process

On the basis of the whole complex of experimental results we have developed the model of photodesorption process, which can be described as follows. Absorption of photon by an atom results in an immediate change in the interaction potential of an atom with nearest environment, thus leading collective oscillations in the adsorbed complex. In a time of an atom vibration period in the potential well occurs a nonradiative transition of an atom to the ground electronic state with the transfer of excitation energy to the kinetic energy of sodium atom and of large number of substrate particles. The large number of particles participating in the absorbed energy redistribution makes process to have a

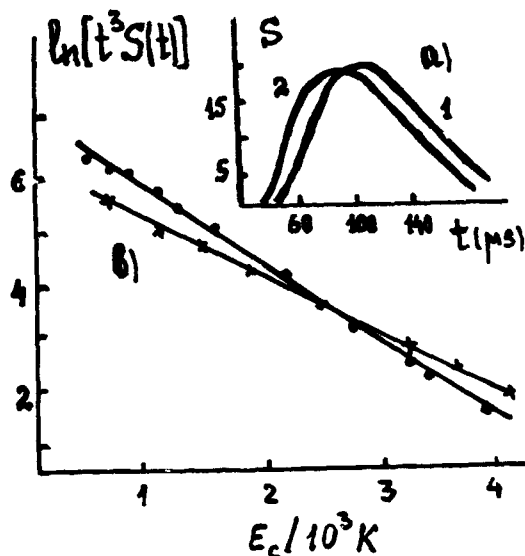


Fig.2. The time-of-flight (a) spectra of sodium atoms desorbed by the second (1) third (2) harmonic radiations of neodymium laser; comparison of the obtained spectra with the Maxwell distribution (b) assuming the effective temperatures, in K: 750(1) and 1000(2)- solid lines; crosses denote experimental values.

statistical character. Assuming in the adsorption complex the uniform distribution of released energy on all degrees of freedom makes us possible to evaluate that its portion which falls directly to the sodium atom and then to calculate both the probability of atom photodesorption and the kinetic energy distribution of the desorbed atoms (the effective temperature of the desorbed flux).

The results agree well with the achieved experimental data both for sodium atoms and for cesium atoms (the low quantum yield of the later is explained by the large size of the electronic cloud).

The suggested model sufficiently good describes all the processes observed in the experiment, namely, the energy distribution of desorbed atoms, the photodesorption spectrum, the growth of the effective temperature and photodesorption quantum yield with desorbing photon energy, etc.

Besides, this model naturally answers the question which often emerges in photodesorption studies, namely, in what way in the apparently one-photon and nonequilibrium process there occurs the Maxwellian thermal energy distribution of desorbed particles that has an effective temperature often considerably higher than the surface temperature.

It should be noted that in the limit of the suggested model the photodesorption quantum yield is determined by statistical probability for adatom to acquire in the course of its electronic excitation the energy, which is higher than the binding surface energy. Most of adatoms thus acquire the energy insufficient for desorption but considerably exceeding the activation energy, 0.1 eV, for the surface diffusion. Thus, in a certain sense, the new effect, light-induced migration of atoms along the crystal surface, is predicted by this model. Indirect proofs of the effect have been obtained in Ref.6 and its further studies seem to be rather interesting and promising, especially not for perfect, but for real surfaces.

The suggested photodesorption model is certainly a merely phenomenological. It does not take into account, for example, the photodesorption effect of structural and physical crystal properties, of crystal surface and bulk phonon spectra, and crystal actual vibration modes etc. It would be desirable to extend the class of studied objects with the aim to ascertain both the regularities of the atoms photodesorption phenomena and distinctions between the studied objects.

## 2. PHOTODETACHMENT OF SINGLE ATOMS FROM A SURFACE OF METAL

### 2.1 General comments

By resonance photodesorption studies, a new effect, photodetachment of sodium atoms from a surface of own metal, was discovered by us.<sup>1,7-8</sup> As found, optical illumination of freshly-prepared metallic film results in an emission of free atoms, besides the known photoemission of electrons. A linear

incident optical power dependence of the effect and low quantum yield,  $10^{-10}$  relative to the incident flux, give unambiguous evidence that the nature of the discovered phenomena is nonthermal.

To the moment this effect was discovered by us, the photodesorption from metal was known to exist only for a small number of simple molecules desorbing from surfaces of heavy-melted metals under the excitation of molecule core electrons by fast electrons, and by far UV or soft X-Ray radiations. As is evident from simple energy considerations, as well as because of the desorbed atom prior to desorption being not foreign for this metal surface, the discovered mechanism must significantly distinct from those known before. The principal properties of the discovered effect have been therefore studied by us.

## 2.2 Principal regularities of atom photodetachment from own metal surface

As shown in Fig.3, the photodetachment spectrum of sodium atoms is fundamentally determined by spectral variations of optical metal properties, that are responsible for the magnitude of the light electric field on the surface. The dependence abruptly increases when the incident radiation frequency appears close to the plasma frequency. Moreover, even photodetachment spectrum normalized by the square strength of the light field on the surface is not similar to the spectrum of the real part of high-frequency conductivity (Fig.3-b). This warrants the conclusion that photodetachment process does not depend on the principal energy dissipation mechanisms in the metal volume.

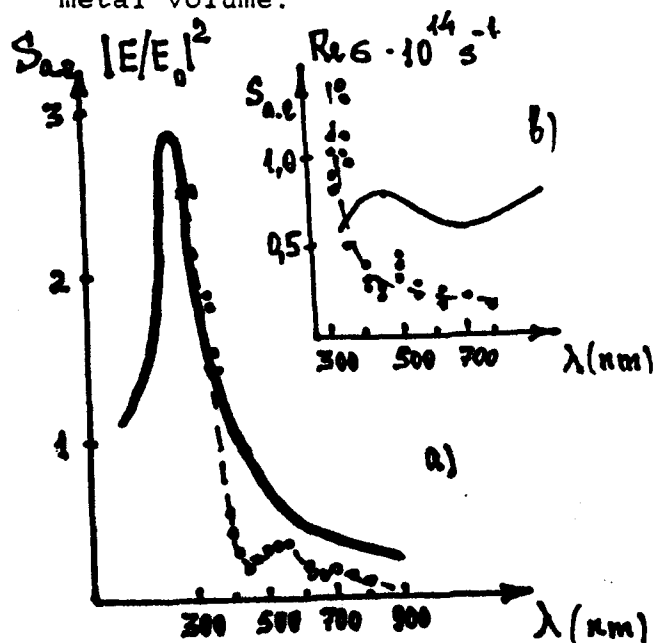


Fig.3.a) The photodetachment spectrum of sodium atoms (dashed) and ratio of the field square amplitude on the metal surface and that of the incident wave (solid); b) The atom photodetachment spectrum normalized by the square field amplitude on the surface (dashed) and the real part of the high-frequency conductivity of sodium metal (solid).

The photodetachment spectrum was also studied for atoms desorbed from island metallic films by authors of Ref.9, but the measurements were performed in a rather narrow spectral range, in which the spectrum turned out to be similar to the plasmon excitation spectrum in the metallic clusters. This made them to explain the observed effect by one of the probable plasmon decay channels. Our measurements evidence that the spectral photodetachment properties for both island and continuous metal films are determined only by the resonance enhancement of the surface field in the region of the plasmon frequencies, not giving direct information about the photodetachment mechanism.

By a number of the experiments it was shown that photodetachment event from the metal surface depends on the presence of surface structural defects; atoms in common sites cannot be detached by optical radiation. The energy of their formation allowing for entropy factor is  $2E = (0.25 \pm 0.05)$  eV, and their concentration at room temperature is  $10^{13} \text{ cm}^{-2}$ , exponentially decreasing with temperature. The nature of these defects is not so far established by us. It may be single atoms in positions near the steps or at the flat surface areas.

In Ref.10 it was shown that introduction of great number of structural defects by evaporating atoms onto the metal film cooled to the nitrogen temperature results in a marked increase in photodetachment efficiency and electronic emission quantum yield, as well as in the metal work function (from 2.31 to 2.36 eV).

The later both facts testify the electronic density in the vicinity of the structural defects to be enhanced. The extra charge of the defect was estimated to be  $g = 0.03$  e. The energy spectrum of desorbed atoms has been detected in several works,<sup>8,9,11</sup> but effective temperatures of these atoms estimated by different authors are significantly different, from 0.4 - 0.5 eV in Ref.8 to the value below the surface temperature in Ref.11. This fact can be explained both by weakness of the effect itself and by use of the different measuring techniques. The technique used by us allowed to do time-of-flight spectral measurements with the single shot of the desorbing laser, whose pulse length was  $10^{-8}$  sec, the signal-noise ratio was 20, and the temporal resolution reached  $10^{-8}$  sec at a full signal length in the course of the spectral measurements being equal 150 s.

The energy distribution of the detached atoms was shown to correlate well with the Maxwellian energy distribution assuming a 700 K effective temperature and deforming by fast electronic excitation quenching near the surface.<sup>8</sup> The experimental spectrum was similar to the spectrum calculated on the assumption that the life time,

$$t = t_0 \exp (x/\alpha),$$

of the excitation localized on the desorbed atom is low compared to the escaping time and rapidly increases with distance from

the surface. Here  $t_0$  is the excitation life time on the surface, and  $\alpha$  is the characteristic size of the atom-surface interaction region. This assumption means photodetachment quantum yield to exponentially depend on the time, in which the adsorbed atom exists in the surface potential region. This time is, in its turn, inversely proportional to the atomic velocity, resulting in a rather unusual form

$$S(t) = t^{-3} \exp(-ml^2/2kTt^2 - t\alpha/t_0)$$

of the time-of-flight-spectrum, in which there are no contribution of slow velocity atoms, so that the most probable velocity corresponding to a 700 K effective temperature of the desorbed flux is 0.2 eV. Here,  $m$  is the mass of sodium atom,  $l$  is the distance between the metal surface and place of detection. Figure 4 illustrates that the best similarity of the calculated and experimental spectra is achieved at  $\alpha = 1\text{\AA}$  and  $t_0 = 10^{-14}$  sec. The latter value slightly exceeds the usual estimates of electronic life times in the metal volume.

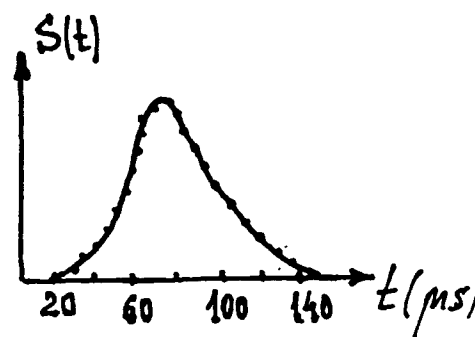


Fig.4. The time-of-flight-spectrum of sodium atoms detached from the metal surface by a 530-nm pulsed laser radiation(solid); crosses denote the calculated spectrum assuming the parameters given in the text.

### 2.3 The suggested photodetachment model

An elementary event including photoelectronic excitation and transfer of its excitation energy to the desorption energy has not been satisfactory described yet. This situation results from a complexity of many-particle process and a variety of ways for its implementation. The most widespread approach to an interpretation of this process as well as the desorption process excited by electronic impact (see, for example the review and the literature, available in Ref.12) is the molecular terms method in which the relaxation of adatom motion is assumed. The method includes two photodetachment processes; the first assumes direct excitation of complex into repulsive state, in conformity with the photodissociation mechanism of molecules, the second assumes transfer of excitation energy from adcomplex to the desorbing atom to result from electronic delectation in the adcomplex.

Since only structurally detached surface atoms whose binding with surface is weaker than binding of atoms in common sites, make contribute to the detachment process, these atoms,

in a certain sense, are foreign for this surface. We suggest that there exists for these structural defects an electronic localization in the ground and excited states, with the life time of their excitation slightly exceeding the excitation life time in the volume.

The observed energy spectrum of the desorbed atoms and the Maxwell velocity distribution deformed by the absence of slowly escaping atoms, are similar; therefore, the photodetachment mechanism can be described as follows. An atom transferred to the excited state, begins its motion from the metal surface. Only those atoms can escape the region of surface attraction that in a period of time  $t = 3 \cdot 10^{-14}$  sec have not relaxed to the ground state. The experimental atomic photodetachment cross section are determined to be  $10^{-23}$  cm<sup>2</sup>.

A reasonable dimension, 4 - 5 Å, was calculated for the quenching region by assuming that the cross section of original electronic photoexcitation event is of the order of  $10^{-16}$  -  $10^{-17}$  cm<sup>2</sup> value, typical of the continuous spectra, and only quenching of electronic excitation near the surface is responsible for the small value of the photodetachment cross section.

It should be noted that such processes as the charge transfer and the surface states effect capable to result in an localization of excitations cannot be discussed in the limit of this model.

In addition, similar photodetachment processes have been recently observed also for gold, aluminum, and silver surfaces.<sup>13,14</sup>

It may be a hope, that further photodetachment studies will result in a better understanding of the process and provide important information about the structure and dynamics of the metal surface.

#### ACKNOWLEDGMENTS

The work is supported by the Russian Foundation of the Fundamental Investigations.

#### REFERENCES

1. I. N. Abramova, E. B. Aleksandrov, A. M. Bonch-Bruevich, V. V. Khromov, "Photostimulated desorption of metal atoms from transparent dielectrics", JETP Lett, vol.39, n. 4, pp.203-205, 1984.
2. A. M. Bonch-Bruevich, Yu. N. Maksimov, V. V. Khromov, "Variations of absorption spectrum of sodium atoms due to their adsorption on sapphire surface", Opt. and Spectrosc., v.58, n. 6, pp.1392-1395, 1985.
3. A. M. Bonch-Bruevich, T. A. Vartanyan, A. V. Gorlanov, Yu. N. Maksimov, S. G. Przibelskii, V. V. Khromov, "Photodesorption of sodium from a sapphire surface", Sov. Phys. JETP, v. 70, pp. 604-612, 1990.
4. A. Zangwill, *Physics at Surfaces*, Cambridge University Press,



England, 1988.

5. A. M. Bonch-Bruevich, T. A. Vartanyan, Yu. N. Maksimov, and V. V. Khromov, "Photodesorption of chemically adsorbed sodium atoms from a sapphire", *Poverkhnost*, v.5, pp. 102-107, 1992.
6. A. I. Plekhanov, V. P. Safonov, and G. G. Telegin, in *Abstracts of VII All-Union Conference on Interaction of Optical Radiation with Material*, v. 2, pp. 95-96, Leningrad, 1990.
7. A. M. Bonch-Bruevich, Yu. N. Maksimov, S. G. Przhibelskii, and V. V. Khromov, "Photoemission of neutral atoms from metal surface", *Sov. Phys. JETP*, v. 65, pp.161-167, 1987.
8. A. M. Bonch-Bruevich, T. A. Vartanyan, Yu. N. Maksimov, S. G. Przhibelskii, and V. V. Khromov, "Photodetachment of atoms from continuous metallic surfaces", *Sov. Phys. JETP*, v.70, pp.993-999, 1990.
9. W. Hoheisel, K. Jungman, M. Vollmer, R. Wedenauer, and F. Trager, "Desorption stimulated by laser excitation of surface plasmons" *Phys. Rev. Lett.*, v.60, n. 6, pp.1649-1653, 1988.
10. A. M. Bonch-Bruevich, T. A. Vartanyan, S. G. Przhibelskii, and V. V. Khromov, "Charge state of the structural defects of metal surface", *Sov. Phys. Dokl.*, v. 36, pp.772-773, November 1991.
11. H. G. Rubahn, in *Laser Spectroscopy and Photochemistry of Metal Surfaces*, Eds. W. Ho and H.-L. Dai, World Scientific, 1993.
12. V. N. Ageev, O. P. Burmistrova, Yu. A. Kuznetsov, *Uspeki Fiz. Nauk*, "Desorption stimulated by the electronic excitation", v. 158, pp. 158- 181, 1989.
13. M. J. Shea, R. N. Compton, in *Laser-Ablation Mechanisms and Applications*, Eds. J.C. Miller and R. F. Naglund, Springer Lecture Notes in Physics, n389, pp.234-238, 1991.
14. R. H. Ritchie, J. R. Manson, and P. M. Echenique, in *Laser Ablation-Mechanisms and Applications*, Eds. J. C. Miller and R. F. Naglund, Springer Lecture Notes in Physics, n. 389, pp.239-243, 1991.

Formation of ohmic contacts to Si and InP by  
the laser-stimulated diffusion methods

G.N.Mikhailova, A.V.Chankin, E.N.Lubnin, A.L.Mikhailichenko, A.S.Seferov

General Physics Institute, Moscow, Russia

A.Yu.Bonchik, S.G.Kiyak, A.V.Pokhmuskaya

Institute of Applied Problems of Mechanics and Mathematics,  
L'vov, Ukraine

V.K.Jain

Solid State Physics Laboratory, Delhi, India

ABSTRACT

Pulsed  $\text{Nd}^{+3}$  laser and 100W cw  $\text{CO}_2$  laser have been used to form ohmic contacts to p-Si. The contact region consists of a layered structure of  $\text{Ag}(5\mu\text{m})/\text{Pd}(300\text{\AA})/\text{Ti}(1200\text{\AA})/\text{p-Si}$ . 1kW cw  $\text{CO}_2$  laser was applied to obtain ohmic contacts on  $\text{Au}/\text{Au-Ge:Ni}/\text{n-InP}$  structure. Secondary Ions Mass-Spectroscopy (SIMS), Electron Auger Spectroscopy (AES) and I-V dependence measurements were carried out, and these results are presented. High-quality ohmic contacts with the resistivity of  $5 \times 10^{-5} \Omega \cdot \text{cm}^2$  can be achieved using cw  $\text{CO}_2$  laser.

1. INTRODUCTION

The general tendency of the modern microelectronics is a transfer from the bulk semiconductor elements to planar technologies. Comparing the recent works on creating the ohmic contacts to semiconductors <sup>1-8</sup> with earlier papers <sup>9-11</sup> shows that the most commonly used technique is now a rapid thermal annealing, its typical times range from 10 s to 5 min, temperatures are 400-1100 °C. The long-duration annealing for several hours is now used comparatively seldom. Obviously, it is connected with the diffusive spread of miniature elements created on the semiconductor crystal.

The element arrangement density in microelectronics is permanently growing, the thickness of the working layers of semiconductor devices are diminishing. Creation of electronic elements of submicron sizes and reproducible parameters are of great interest in microelectronics. The main limiting operations are here formation of perfect interfaces, small-area p-n junctions, bases of transistors, contacts and conducting strips. Usual thermal diffusion methods are not suitable for submicron dimensions. Laser processing is an attractive technology used in microelectronics. So, laser solid-phase doping of semiconductors was found to be an excellent technique for fabrication of submicron doped layers in silicon <sup>1,2,7,12</sup>, as well as for A<sup>III</sup>B<sup>V</sup> group of semiconductors <sup>3-8,13</sup>.

Laser can be considered as an excellent tool in microelectronics technologies. Its radiation can be brought to a desirable place, exposure is precise, the beam is stable and homogeneous. A low divergency of the beam gives a possibility to focus the radiation onto small spots: there is a possibility of direct "drawing". The ability to change the wavelength is also a great advantage: specific substances can be processed. These factors provide completely new technological capabilities.

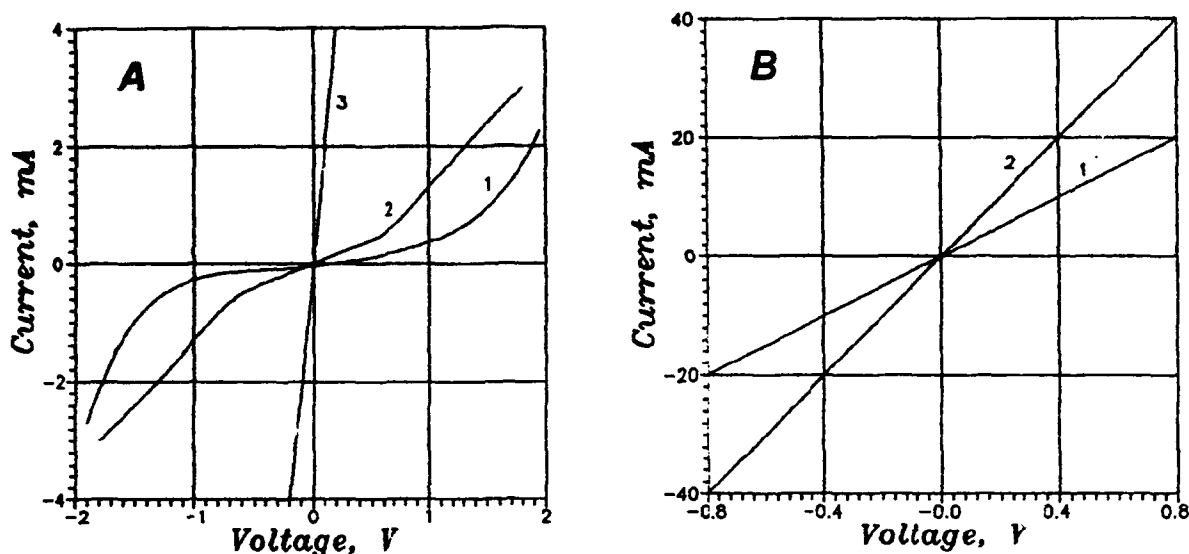


Figure 1. I-V characteristics of p-Si:Ti/Pd/Ag contacts:

(A) 1) before irradiation; 2) after irradiation with 4 pulses of  $\text{Nd}^{+3}$  laser (energy density  $36.0 \text{ J/cm}^2$ , pulse duration  $1.2 \text{ ms}$ ); 3) after irradiation with 10 pulses of Q-switched  $\text{Nd}^{+3}$  laser (energy density  $5.0 \text{ J/cm}^2$ , pulse duration  $80 \text{ ns}$ );

(B) after  $\text{CO}_2$ -laser irradiation with the intensity of  $45 \text{ W/cm}^2$ ; 1)  $15 \times 1.75 \text{ s}$ , irradiation from the front side of the sample; 2)  $5 \times 1.5 \text{ s}$ , irradiation from the back side of the sample.

There are two basic methods of laser doping. The solid-phase doping regime is realized using the continuous laser radiation. Usually  $\text{CO}_2$ -lasers are used <sup>7,8,11,12</sup>, in <sup>13</sup> a continuous YAG: $\text{Nd}^{+3}$  laser was applied. This regime is close to a fast thermal annealing method. It allows to properly control the diffusive process and is rather easily theoretically treated.

The laser liquid-phase doping method is much less controlled. Here short-pulse (usually Q-switched) lasers are used <sup>6,11,13</sup>. The liquid-phase regime is characterized by the sample surface melting under the influence of laser radiation. During the pulse action the great temperature gradients - up to  $10^9 \text{ K/cm}$  - rise in the sample, significant stresses appear in the material. The diffusion processes develop under substantially inequilibrium conditions, it is aggravated with phase transitions in the surface region of semiconductor. In this case it is very difficult to control the diffusion, and an adequate theoretical calculation is a very complicated problem. The laser liquid-phase method has the only principal advantage, but a great one: a unique locality of the effect. All the absorbed laser pulse energy is released as a heat in a strictly limited region of semiconductor. Diffusive temperature spread does not exceed  $10 \text{ }\mu\text{m}$  during the typical pulse duration of  $\sim 100 \text{ ns}$ . There is a possibility to process very small surface areas without affecting the whole semiconductor crystal, and it is of a great practical interest.

Both methods of laser annealing are successfully used for creating ohmic contacts to semiconductors <sup>6-8,11-13</sup> and, of course, they are very promising for application in the microelectronics technology.

## 2. CONTACTS TO p-Si

### 2.1. Experimental

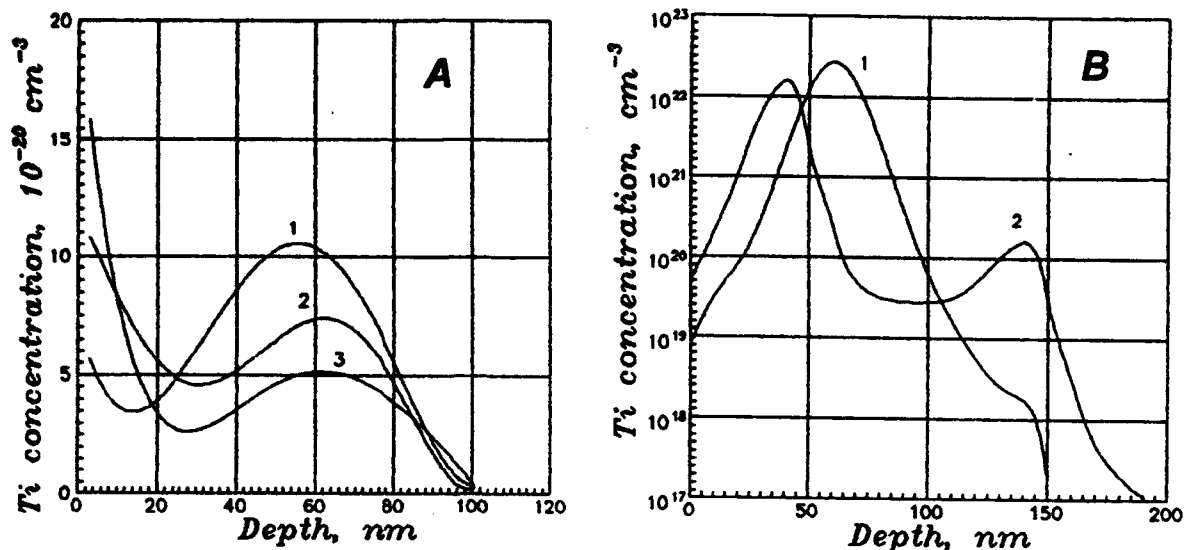


Figure 2. Depth profiles of Ti distribution in p-Si:Ti/Pd/Ag contacts after laser doping (obtained by SIMS method). Irradiation regimes:

(A) 1) 5 pulses of Q-switched  $\text{Nd}^{+3}$  laser, energy density  $6.0 \text{ J/cm}^2$ , pulse duration 80 ns, contact is ohmic, but surface of the sample is slightly damaged; 2) 10 pulses of Q-switched  $\text{Nd}^{+3}$  laser, energy density  $5.0 \text{ J/cm}^2$ , pulse duration 80 ns, contact is ohmic; 3) 4 pulses from  $\text{Nd}^{+3}$  laser, energy density  $36.0 \text{ J/cm}^2$ , pulse duration 1.2 ms, contact is nonohmic.

(B) irradiation by  $\text{CO}_2$ -laser with the intensity of  $45 \text{ W/cm}^2$ ; 1)  $15 \times 1.75 \text{ s}$ , irradiation from the front side of the sample, contact is ohmic; 2)  $5 \times 1.5 \text{ s}$ , irradiation from the back side of the sample, contact is ohmic.

Contact metallic structure  $5 \mu\text{m Ag}/300 \text{ \AA Pd}/1200 \text{ \AA Ti}$  was deposited by thermal evaporation onto wafer of p-type Si (100) doped with boron concentration of  $1 \cdot 10^{16} \text{ cm}^{-3}$ . Wafer was patterned lithographically and was then divided into several small samples for contact annealing using various techniques.

We have used two substantially different methods of laser-stimulated diffusion. Method of liquid-phase diffusion was harnessed using the irradiation either with several  $\text{Nd}^{+3}$ -laser pulses of millisecond duration ( $\lambda = 1.06 \mu\text{m}$ , energy density was up to  $40 \text{ J/cm}^2$ ) or with several 80-nanosecond pulses of Q-switched  $\text{Nd}^{+3}$ -laser (energy density - up to  $6 \text{ J/cm}^2$ ). Irradiation was carried out in air. Laser radiation was homogenized by special diffuser. Careful masking of the semiconductor's surface was necessary to avoid its damage, because silicon has a small reflectivity at the wavelength of  $1.06 \mu\text{m}$  in comparison with the metal film. The high quality of the contact surface is important, because inhomogeneities cause abrupt increase of absorption and contact damage.

Solid-phase diffusion method was harnessed using 100W cw  $\text{CO}_2$  laser ( $\lambda = 10.6 \mu\text{m}$ ). Samples were placed into a vacuum chamber. Pressure was about  $5 \cdot 10^{-5} \text{ Torr}$ . Contacts were irradiated either from the front or from the back side of the samples with several pulses of 1.5-1.75 s duration.

I-V characteristics were obtained by simple measurements between the pairs of 5 mm-spaced contacts with the size of  $1 \times 5 \text{ mm}^2$ .

The depth distribution of the titanium dopant was investigated by Secondary Ions Mass-Spectroscopy (SIMS) using SIMS-Lab setup. We used  $\text{O}^{+2}$  primary ions with the energy of 4 keV and current density of  $1 \mu\text{A/cm}^2$ . Essential advantages of  $\text{O}^{+2}$  ions application for sputtering the solid samples is an increase of ionization degree and

a decrease of element detection threshold. Moreover, the homogenization level is stabilized and this is important for a complex structural analysis. We used a scanning regime for sample sputtering in area of  $500 \times 500 \mu\text{m}^2$ . The secondary ions were collected from the region with the diameter of  $70 \mu\text{m}$  in the center of the sputtered area to avoid the crater effect. Composition profiles were recorded as time functions for the  $\text{Ti}^{+48}$  secondary ions current intensity. The conversion from the current intensity to the atom concentration was made using the reference silicon samples with preknown titanium content. The depth of sputtering was determined applying the Talystep profile register. We also registered an output of  $\text{Ti}^{+96}$  cluster ions to increase the reliability of the measurements. Comparison has shown an identity of profiles for  $\text{Ti}^{+48}$  secondary ions and  $\text{Ti}^{+96}$  cluster ions.

## 2.2 Results and discussion

Ohmic contacts were successfully formed by both methods. Fig.1 represents the I-V characteristics of the samples before and after the irradiation.

Ten 80-ns pulses from Q-switched  $\text{Nd}^{+3}$ -laser with the energy density of  $5.0-5.5 \text{ J/cm}^2$  produced ohmic contacts with a good reproducibility. Ohmic behaviour of I-V characteristics is exhibited at the current density up to  $0.2 \text{ A/cm}^2$ . SIMS analysis (Fig.2) shows a pronounced presence of titanium at a depth of about 60 nm.

We obtained low-quality ohmic contacts using  $\text{Nd}^{+3}$ -laser with a pulse duration of 1.2 ms and energy density of  $40 \text{ J/cm}^2$ . An increase of the number of pulses gave no positive effect. We suppose that the contacts oxidize during a relatively long pulse in air. Analysis confirms a pronounced presence of oxygen in the surface layers of the samples.

Ohmic contacts of the best quality were formed by the solid-phase laser-stimulated diffusion method using cw  $\text{CO}_2$  laser with the power density of  $45 \text{ W/cm}^2$ . Fifteen pulses with the duration of 1.75 s were necessary for the front irradiation. Five 1.5 s pulses were enough to obtain excellent ohmic contacts at irradiation from the back side of the samples. The time between the pulses was about 1 min to avoid overheating. The measurements of the I-V characteristics show a high quality of the contacts: the resistivity is smaller by two orders of magnitude in comparison with the contacts obtained by the liquid-phase method. The ohmic character of I-V characteristics is exhibited up to the current density of  $1.4 \text{ A/cm}^2$ . SIMS analysis shows that both the titanium concentration and diffusion depth are significantly larger in the case of the solid-state method. The local maximum in the titanium distribution profile is explained by mechanical stress gradients which take place in the samples during heating. Such maxima were observed earlier under similar irradiation conditions.

## 3.CONTACTS TO n-InP

### 3.1.Experimental

By cathode vacuum evaporation the  $\text{Au}(2500 \text{ \AA})/95\% \text{ Au:Ge-5\%Ni}(700 \text{ \AA})$  structure was deposited on n-InP wafers ( $n=10^{16}-10^{17} \text{ cm}^{-3}$ ). 1kW power cw  $\text{CO}_2$  laser (with the wavelength of  $10.6 \mu\text{m}$ ) was used for the irradiation of semiconductors from the back side in the vacuum chamber (pressure was  $10^{-6}$  Torr). The duration of laser action was 1 s. The whole sample was irradiated uniformly.

### 3.2.Results and discussion

The depth distribution of chemical elements was investigated by means of Electron Auger Spectroscopy (AES) using JAMP-10s (JEOL) setup. The electric properties of the formed contacts were studied by the chemical etching method.

Fig.3 shows the AES data obtained after irradiating the conductive  $\text{Au/Au:Ge-Ni}$  structure on InP. One can see that insignificant mixture of contact elements took place excluding Ni, which replaced In in the depth up to about 600  $\text{\AA}$  in the surface layer of the semiconductor. A complex profile of Ni in-depth distribution (namely, there are two

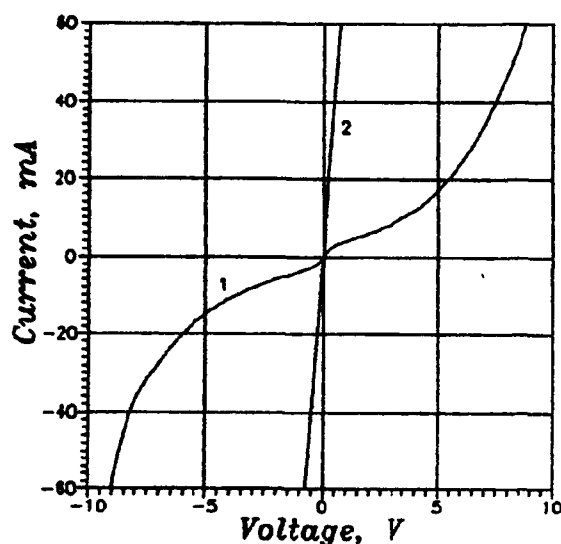


Fig 3.

Figure 3. I-V characteristics of Au/Au:Ge-Ni/n-InP contacts before irradiation (1) and after CO<sub>2</sub>-laser irradiation with an intensity of 400 W/cm<sup>2</sup> during 1 s (2). Figure 4. Depth profiles of element distribution obtained by AES method in ohmic contacts Au/Au:Ge-Ni/n-InP formed under the influence of CO<sub>2</sub>-laser radiation with an intensity of 400 W/cm<sup>2</sup> during 1 s; 1 - Au, 2 - Ge, 3 - Ni, 4 - In, 5 - P.

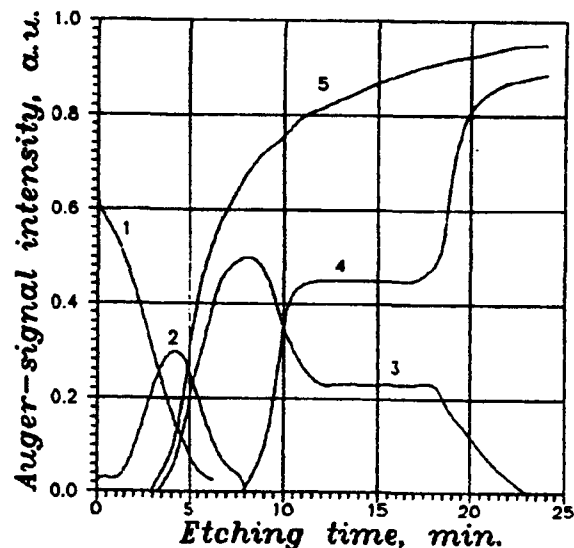


Fig 4.

typical parts, looking like a bell and plateau) indicates a nontrivial mechanism of impurity diffusion. However, we could not connect this fact with the laser effect, because the similar results were obtained by Wang, Parker et al. at pulsed thermal impurity diffusion into InP after a short thermal annealing<sup>5</sup>. Mentioned above authors understood the complex form of Ni profile by the properties of annealed single InP crystals. We consider that this explanation is valid for the laser treatment as well. I-V curves for the contacts to InP are shown in Fig.4. Typical nonlinear rectifying characteristics after the laser irradiation were transformed to a straight line. At the same time the resistivity of the contacts reduced to the value of about  $5 \cdot 10^{-5} \Omega \cdot \text{cm}^2$ , which is consistent with the requirements for the ohmic contacts to InP.

#### 4. CONCLUSIONS

The experiments demonstrate good possibilities for the formation of the reproducible high-quality ohmic contacts to p-Si:Ti/Pd/Ag and n-InP:Ni-Au-Ge/Au structures using the laser stimulated diffusion methods, especially the solid-phase one applying cw CO<sub>2</sub>-laser radiation.

#### 5. REFERENCES

1. M. Sekine, N. Itoh et al., "0.4  $\mu\text{m}$  contact with lower resistivity metallization technology for ULSI applications", Extend. Abstr. 1992 Int. Conf. Solid State Device and Mater., Tsukuba, Aug., 26-28, 1992, pp.184-186.
2. Cho Hyun-Choon, Paek Su-Huon et al., "Electrical characteristics of TaSi<sub>2</sub>-p<sup>+</sup>-Si and TiSi<sub>2</sub>-p<sup>+</sup>-Si contacts formed by rapid thermal annealing", *Thin Solid Films*, 221, N1-2, pp.201-206, 1992.

3. Y.S.Tang, C.D.Wilkinson, C.Jeynes, "Pd / Ti bilayer contacts to heavy doped polycrystalline silicon", *J. Appl. Phys.*, 72, N1, pp.311-312, 1992.
4. H.J.Takata, Tanahashi Kiwamu et al., "Thermally stable non-gold ohmic contacts to n-type GaAs", *J. Appl. Phys.*, 72, N9, pp.3570-3577, 1992.
5. K.Wang, S.M.Parker, C.Cheng, J.Long, "Diffusion in InP using evaporated  $Zn_3P_2$  films with transient annealing", *J. Appl. Phys.*, 63, N6, pp.2104-2109, 1988.
6. Z.L.Liau, N.L.DeMeo et al., "Redistribution of implanted Zn in InP after Q-switched laser annealing and the related specific contact resistance", in: *Laser and electron beam processing of materials*, ed. by C.W.White, P.S.Peersy, Academic Press, New York, 1980, pp.500-505.
7. A.Yu.Bonchik, A.V.Chankin, S.G.Kiyak, E.N.Lubnin, G.N.Mikhailova et al., "Direct doping of impurities into Si, GaAs, InP and ohmic contacts formation using high power cw  $CO_2$  laser", Abstr. of E-MRS '91, Spring Meeting, Strasbourg, 1991, E-V / P64.
8. A.Yu.Bonchik, S.G.Kiyak, G.N.Mikhailova, A.V.Pokhmurskaya, "Formation of ohmic contacts to InP by the laser diffusion method", *Kratkie Soobsheniya po fizike FIAN (Russian journal)*, N7-8, pp. 35-38, 1993.
9. V.L.Rideout, "A review of the theory and technology for ohmic contacts to group III-V compound semiconductors", *Solid-State Electronics*, Vol.18, N6, pp.541-550, 1975.
10. A.G.Milnes and D.L.Feucht, *Heterojunctions and metal-semiconductor junctions*, Academic Press, New York, 1972.
11. R.S.Pounds, M.A.Saifi, W.S.Hahn, "Formation of ohmic contacts to III-V semiconductors using a laser beam", *Solid-State Electronics*, Vol.17, N3, pp.242-249, 1974.
12. A.M.Prokhorov, A.Yu.Bonchik et al., "Laser solid-phase doping of semiconductors", *Appl. Surf. Sci.*, 43, 340, North-Holland, 1989.
13. L.Hudec, P.Machac, V.Myslik, "Laser annealed ohmic contacts on GaAs structure", Int. Symp. on Advanced Laser Technologies (ALT-93), Prague, November 8-13, 1993.

Optically induced changes of magnetization of YBaCuO-samples  
- crucial examination of the states with fractional  
statistics in high-Tc cuprates.

Valerii Aksenov and Kirill Prokhorov  
General Physics Institute, Vavilova, 38, 117942 Moscow, Russia.

ABSTRACT

A new method for the studies of the spontaneous magnetic field (SMF) in quasi-two-dimensional systems these as high-temperature oxide superconductors is presented. For measuring of magnetic field was used deconfinement anyons at interplanar hopping induced by laser irradiation. Magnetometer with optical access was used for measurement the light induced changes of magnetization at different temperature and intensity of light and external magnetic field. Observed behavior is probably the evidence of the existing of a phase with fractional statistics and spontaneous magnetic field.

2. INTRODUCTION

The discovery of high-temperature oxide superconductors has stimulated interest in study of superconductivity in quasi-two-dimensional systems, since the conduction electrons in these oxides are essentially constrained to move in two-dimensional sheets. The different theoretical models of a high temperature superconductivity are active discussed. Together with conventional models of Bardeen-Cooper-Schriffer superconductors some very exotic theories have been proposed<sup>1-11</sup>. A unique feature of 2D systems is that they can support quasiparticles obeying fractional statistics (referred to as anyons) while only Fermi and Bose statistics are allowed in 3D system<sup>1,2,9-11</sup>. Fractional statistics can be parameterized by a continuous variable  $\alpha$  such that the anyon wave function acquires a phase factor  $\exp(i\pi\alpha)$  from interchange of two anyons. Thus, fractional statistics interpolate between Bose ( $\alpha=0$ ) and Fermi ( $\alpha=1$ ) statistics.

In profound and original article<sup>2</sup>, Laughlin outlined a general picture for the superconductivity of the fractional statistics fluid. Microscopically semions, being halfway between fermions and bosons, should be more inclined than fermions to pair. Two semions make a boson and condensation of such bosons may lead to superconductivity.

One essential feature of the anyon models is a violation of the discrete symmetries of time reversal  $T$  and the two-dimension reflection symmetry  $P$ <sup>1,2,9,10</sup>. One of the most interesting consequences of the broken  $P$  and  $T$  symmetry is the prediction of the intrinsic orbital magnetic moment perpendicular to the each anyon layer, whose sign depends on the sign of the broken symmetry in the layer if the coupling between layers is ferromagnetic there should be number of observable bulk effects, including optical rotation and anomalous transport properties analogous to a Hall conductance which would occur even in absence of an external magnetic field. Depending on the sample geometry there may be a magnetic domain structure and or fringing magnetic fields. According to the anyon model, the strength of the magnetic moment is of order  $15 G^9$ .

The existence in actual condensed matter systems of quasiparticles with fraction statistics was first noted in the case of the fractional quantized Hall effect<sup>2</sup> (FQHE). Lyons et al.<sup>14</sup> report observation of circular dichroism in reflection from cuprate superconducting materials, including YBaCuO films, an etched YBaCuO crystal, and a BiSrCaCuO crystal. This signal develops as  $T$  is lowered below 200K and exhibits little change near  $T_c$ . Laughlin et al.<sup>15</sup> have carefully reproduced the apparatus of Lyons et al. They have not observed temperature-dependent signal from a variety of YBaCuO samples studied. In recent letter, Lyons et. al.<sup>16</sup> reported the observation of the nonreciprocal



polar Kerr effect (NPKE) in high- $T_c$  cuprates. The results show that the time-reversal symmetry is broken in this material.

In the present work we report on experimental observations of "Luttinger-liquid", a state in which charge and spin acquire distinct spectra in superconducting cuprate materials.

### 3. EXPERIMENTAL PART

The samples for studies are the two-dimensional films of high- $T_c$  cuprates and the planar semiconductor 2D structures. Superconducting films of YBaCuO and YBiCaCuO about 500-2000 Å thick were made by laser ablation on SrTiO or MgO substrates. The temperature of the superconductive transition in the film material was higher than 77 K and the c-axis should be perpendicular to the surface in all samples.

The 92 K superconducting phase YBaCuO is the remarkably complicated material: the oxygen stoichiometry is less than 7 and the chain oxygen atoms can assume a number of possible orderings. The superconducting transition temperature, as well as other physical properties, depends sensitively on the oxygen content and ordering.

The sample and two kinds of magnetometer are shown in Fig.1. In practice, the magnetometer with optical access was used to detect light induced changes of magnetization of the samples. The samples were illuminated by laser radiation straight in the dewar with the help of optical fiber. To separate the optically induced signal from any slow drift of the background noise, we used the pulse laser excitation.

In present experiments spontaneously magnetic fields in superconducting films were measured by means of the anomalous destruction by optical radiation and detection of change magnetic flux. The magnetic detector was placed perpendicular to the plane of incidence, approximately 0.1 mm from sample. The pumping radiation for the measurement was supplied by a Q-switched Nd:YAG laser operating at 1.06  $\mu\text{m}$  and producing 100 ns pulses at repetition rate from 10 Hz to 5 kHz. The incident laser beam was focused to the diameter of about 1-3 mm on the sample surface. The signal from magnetic-probe coil detected by gated electronics.

### 4. RESULTS AND DISCUSSION

Several recent theoretical studies have suggested that the quantum dynamics of a strongly-correlated many particle system on a two-dimensional lattice can lead to a state of matter in which the orbital motion of the particles breaks the reflection and time-reversal symmetry of the underlying microscopic Hamiltonian. These P-T breaking states are of fundamental interest, since the quasiparticles of these states can exhibit particle number fractionization and the anomalous quantum statistics implied by this phenomenon.

In comparison with metallic films, high- $T_c$  oxides have the lower light reflection coefficient. This feature makes the high- $T_c$  cuprates attractive for investigations of the influence of light irradiation on their superconducting and normal state properties. The incident light of maximum intensity  $10^2 \text{ W/mm}^2$  is absorbed over a distance of the order of  $1/\alpha = 1 \mu\text{m}$ , where  $\alpha$  is the crystal absorption coefficient at  $\lambda = 1.06 \mu\text{m}$ . On the rear side of the sample a structure of registered coil acts as a local detector of the spinons.

When superconducting films are illuminated by laser light, heating of the sample becomes the interfering factor in experiments aimed to detect the light-induced nonequilibrium phenomena. To exclude the possibility of heating effect on changes of the magnetization we have estimated the increase of sample's temperature under the laser illumination. The heating was found to be less than 10 K at pumping power densities about  $1 \mu\text{J/mm}^2$ .

We propose new type of measurements to detect the possible existence of the spontaneous magnetic field in the high-Tc cuprates. Our experiments are based on the properties of interplanar hopping that converts a spinon into holon and creates an electron in the next plane, which propagates as spinon and holon<sup>3-8</sup>.

The interlayer electron hopping corresponds to the instanton, described by a monopole in the gauge potential. Have shown that monopoles convert anyon superfluid into normal liquid<sup>12</sup>. Interlayer hopping corresponds to changing of the magnetic flux of the Cu-O plane because the spinon transformation into holon induces the annihilation of the magnetic flux quantum. Spinons under interlayer hopping dissociate at

$$S_1 + hu \rightarrow H_1 + e_2 \rightarrow H_1 + S_2 + H_2 \quad (1)$$

where  $S_1$  and  $H_1$  are a spinon and a holon in the layer 1,  $e_2$  is a electron in the layer 2,  $S_2$  and  $H_2$  are a spinon and a holon in the layer 2.

One point of view is that the spinons are topological excitations of the soliton type which appear on the background of the short-range antiferromagnetic order. In this scenario the spin has a topological origin and does not interact with a physical magnetic field. In the mean-field approximation the statistical flux carried by the particles be averaged over space. The particles are then treated as moving in a uniform magnetic field<sup>13</sup>:

$$B = \epsilon_{\alpha\beta} \partial_\alpha a_\beta = 2n\theta \quad (2)$$

where  $\epsilon_{\alpha\beta}$  is the structural constant,  $a_\beta$  is gauge field component,  $n$  is a particle density,  $\theta$  is a statistics constant. The idea is then to reduce the problem to single-body problem. At first sight, this appears questionable since the gauge potential  $a_1$  felt by each particle is in fact a pure (but topologically nontrivial) gauge and thus associated with zero B:

$$\epsilon_{\alpha\beta} \partial_\alpha a_\beta = 0 \quad (3)$$

Consider, however, the scattering of one particle off another. Due to P (and T) violation, the particle tends to scatter preferentially to one side. The net effect is that the particle moves more or less in a circular orbit and acts as if it experiencing a uniform magnetic field. More precisely, as a given particle is transported around a large loop of area  $A$  and, enclosing  $nA$  particles, its W.F. picks up a phase  $\exp(inA\theta)$  thus, the effect "magnetic field"

$$B = 2n\theta \quad (4)$$

The intrinsic orbital magnetic moment direction depends on the sign of scattering angle that determined by the sign of the symmetry breaking parameters. So that the electron interlayer hopping would be to induce the change magnetic flux that deal with the sign change anisotropy of scattering. It is possible that the effect of the no dependence from external magnetic field is determined by topological nature of anyons.

The value of magnetic flux photoinduced change for the antiferromagnetic coupling of Cu-O planes given by:

$$M = \alpha \beta I_0 \sum_{n=0}^{\infty} (-1)^n \exp(-\beta d n) = \alpha \beta I_0 \frac{1}{1 + \exp(-\beta d)} = \alpha \beta I_0 / 2 \quad (5)$$

where  $\alpha$  is constant,  $\beta$  is absorption coefficient of light in film (give consider that photons induce the transitions from the ground states would be to transform spinons into holons and to change the magnetization of the planes),  $I_0$  is intensity of the incident light. In the case of antiferromagnetic alignment of the magnetic moments we anticipate that the signal from the thick film would be equivalent to the signal from one plane. The enlarging of the sample volume would only provide the increase of the signal if the interplanar alignments of moments are ferromagnetic. In this case the signal should be equivalent to the signal from the bulk crystal with thickness equal to the length of light absorption in the film.

$$S = \alpha \beta I_0 \sum_{n=0}^{\infty} \exp(-\beta d n) = \alpha \beta I_0 \frac{1}{1 - \exp(-\beta d)} = \alpha I_0 / d = \alpha \beta I_0 L / d \quad (6)$$

where  $L=1/\beta$  is the absorption of light length.

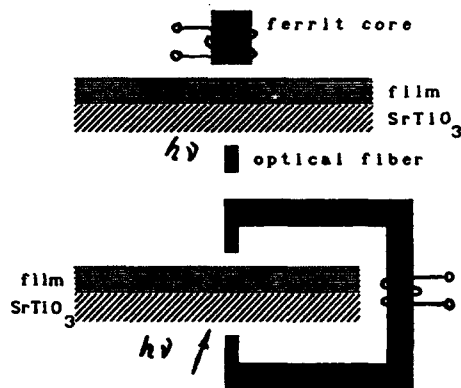


FIG.1. Schematic view of the test coil and the high- $T_c$  film structure analyzed in this study.

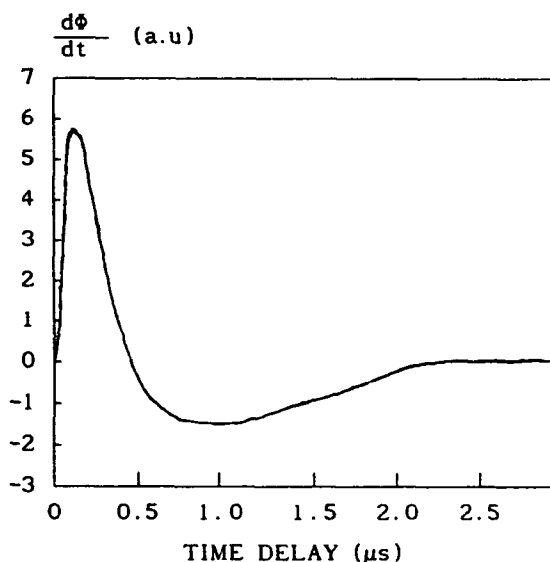


FIG.2. Time responses of the magnetic flux time derivative of the high  $T_c$  superconducting film at room temperature and at the pulse laser excitation.

We have observed optically-induced changes of spontaneous magnetization in the YBaCuO sample and investigated the dependence of these changes on temperature and intensity of light. Typical oscilloscope traces of observed magnetic-probe signal is shown in Fig.2 for incident laser of about  $E=1 \mu\text{J}/\text{mm}^2$ . The long tail of a signal is connected with electron relaxation to the ground states at the cuprous planes. It has been confirmed that the direction of generated magnetic field was normal to the surface of film. For the evaluation of the magnetic moment change we used a simplified model of the magnetometer<sup>17</sup>. For the detecting coil with radius  $R$  and a small sample (diameter  $D$  and length  $L$ ) with

homogeneous magnetization  $M=m/V$  is put at the center of the detecting coil, we have for the magnetic flux  $\Phi=\oint B dS$  through the detecting coil:

$$\Phi = \frac{2\pi M V}{R} \left\{ 1 + \frac{3}{8} \left[ \frac{D}{2R} \right]^2 - \frac{1}{2} \left[ \frac{L}{2R} \right]^2 \right\} \quad (7)$$

for  $2R > D, L$

$$U = -N\mu \frac{d\Phi}{dt} = N\mu \frac{\Delta\Phi}{\Delta t} = \frac{2\pi\Delta M V}{R\Delta t} N\mu \quad (8)$$

Applying this equation to the magnetometer used in our measurements with  $R=2$  mm, and  $D=2$ mm,  $L=1\mu m$ ,  $\mu=200$ ,  $\Delta t=100$  ns,  $N=40$  number of coils,  $U$  is 0.0002 V.

$$\Delta M = \frac{R\Delta t U}{2\pi V N\mu} \quad (9)$$

For case of AFM ordering we obtain the evaluation of the photoinduced magnetization change  $\Delta M=3 \cdot 10^{-4} Vc/m^2=3$  G (for  $L=d=10$  A)

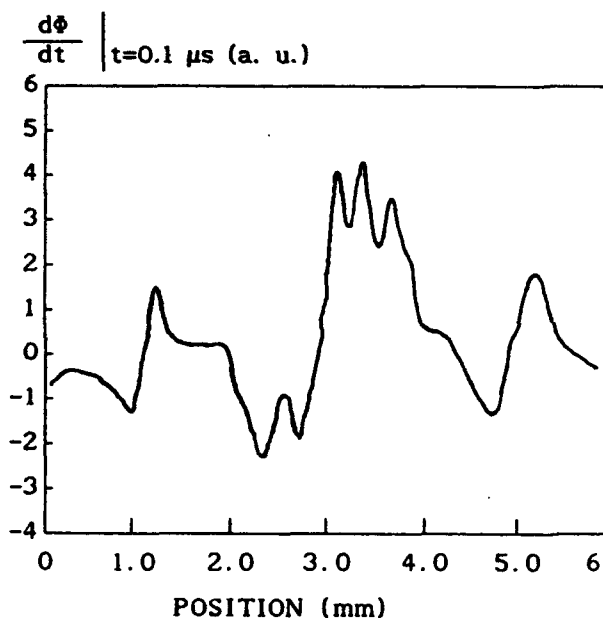


FIG. 3. A longitudinal profile of the magnetometer signal of the high  $T_c$  film (YBaCuO) magnetic field at the time delay is equal to 100 ns after switching laser pulse, that corresponds to maximum value of detected signal.

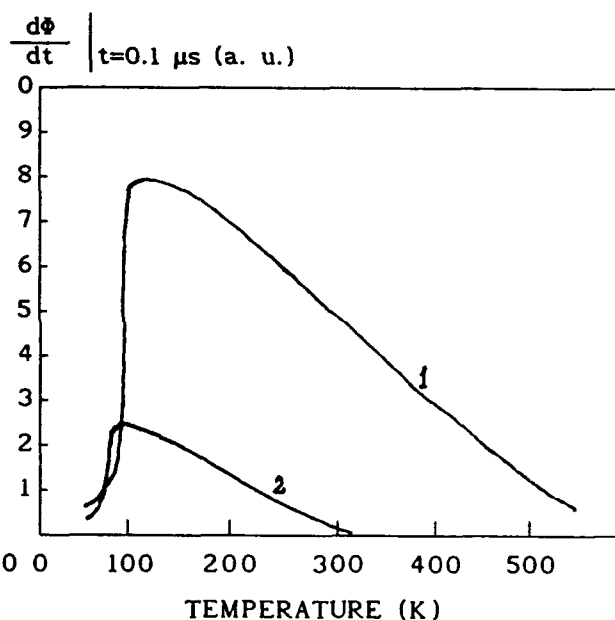


FIG. 4. The magnitude of the magnetic-probe signal as function of temperature at time delay is 100 ns. (1) YBaCuO film with  $T_c=87K$ , (2) YBaCuO film with  $T_c=85K$ .

Location of magnetic probe coil at different places on a film surface (that is some kind of mapping) gives considerably different signals. It can be seen on the the Fig.3. This means that our samples were not perfect and homogeneous. It is not very surprising result. The films had a defects which caused an arising of the macroregions with opposite orientation of magnetic field (some kind of macrodomain structure). We have observed the defects that as a cylindrical domain with the interior of the domain wall is the insertion

of the ferromagnetic state and with opposite directional magnetic fields of outward region is similar to the topological defect that as a skyrmion.

Some of the measurements were made at external magnetic field about 200-400 Oe. Light-induced changes of the magnetization were found to be not sensitive to the applied magnetic field. This means that the mechanism based on uniform laser generation of the current cannot explain our results.

We have measured the optically-induced signal upon the samples temperature. Fig.4. The signal continuously increases while moving to the low temperatures up to transition to the superconducting phase. Exactly at the  $T_c$  temperature the signal disappear. The effect was inversable and we could again discover the signal with increasing the temperature. The sample 2 differed from sample 1 by brief annealing in nitrogen atmosphere at 450 C. This means that the sample 2 having lower oxygen content transforms into the phase with spontaneous magnetic field at lower temperature and the jump of magnetic flux under light illumination not so big. We could not observed any response in a heavy annealed, insulating samples. Such a behavior provides the evidence that existing of the spontaneous magnetic field is related to free carriers. A similar behavior of the value SMF as the function of temperature has been observed by Lyons et al.<sup>16</sup> in the circular dichroism studies of the high- $T_c$  cuprates. This may indicate that the we have situation with antiferromagnetic coupling of the anyon (ferromagnetic) Cu-O planes.

These experimental results are explained by the following model: (1) Existence of the fractional statistics and SMF in the high- $T_c$  cuprates and (2) independence of spin and charge excitations.

## 5. CONCLUSION

The spontaneous magnetic field in high- $T_c$  cuprates would appear to be an ideal tool to probe anyon physics, especially that of P and T symmetries breaking. The spontaneous magnetic fields in superconducting films was observed and measured in the high- $T_c$  cuprates by new experimental method. The existence of system with independent spin and charge excitations was experimentally proved in YBaCuO. The main conclusion of present article is thus that the observed signal is probably the signature of a phase transition to the phase with the fractional statistics in cuprates systems.

## REFERENCES

1. F. Wilczek, "State of Anyon Matter", Int.Jorn. of Modern Physics B, vol. 5, pp.1273-1312, 1991
2. R.B. Laughlin, "The Relationship Between High-Temperature Superconductivity and the Fractional Quantum Hall Effect", Science, vol.242, pp. 525-533, 1988.
3. P.W.Anderson, "The Resonating Valence Bond State in  $\text{La}_2\text{CuO}_4$  and Superconductivity", Science, vol. 235, pp. 1196-1198, 1987.
4. P.W.Anderson, G.Baskaran, Z. Zou, J. Wheatly, T.Hsu, B.S.Shastry, B.Doucot and S.Liang, "The Theory of High- $T_c$  Superconductors-Comparisons with Experiment", Physica C 153-155, pp. 527-530, 1988.
5. P.W.Anderson, "Luttinger-Liquid Behavior of the Normal Metallic State of the 2D Hubbard Model", Phys.Rev.Lett. v.64, 1839-1841 (1990).
6. J.M.Wheatley, T.C.Hsu, and P.W.Anderson, "Interlayer effects in High- $T_c$  Superconductors", Nature 333, pp. 121-124, 1988.
7. P.W.Anderson, "Two Crucial Experimental Test of the Resonating Valence Bond - Luttinger Liquid in Interlayer Tunneling Theory of High- $T_c$  Superconductivity", Phys. Rev. B 42, pp.2624-2626, 1990.
8. P.W.Anderson and R.Schrieffer, "The give-and-take between two solid state

theorists....", Physics today v. 6, pp.55-61, 1991.

9. B.I.Halperin, J.March-Russel and F.Wilczek, "Effective theory of the T and P breaking superconducting state. Consequences of time -reversal -symmetry violation in models of high Tc superconductors", Phys.Rev. B vol.40, pp. 8726-8744 ,1989.

10. C.B.Hanna, R.B.Laughlin, A.L.Fetter, "Quantum Mechanics of the Fractional Statistics Gas: Hartree-Fock Approximation",Phys.Rev.B vol. 40, pp. 87-8758, 1989.

11. V.Kalmer, R.B.Laughlin, "Equivalence of the Resonating-Valence Bond and Fractional Quantum Hall States", Phys.Rev.Lett. 59, pp. 2095-2098, 1987.

12. X.G.Wen and A.Zee, "Compressibility and superfluidity in the fractional-statistics liquid", Phys.Rev. B vol. 41, pp. 240-253, 1990.

13. X.G.Wen and A.Zee, "Neutral Superfluid Modes and "Magnetic" Monopoles in Multilayer Quantum Hall Systems", Phys.Rev.Lett. 69, N12, pp. 1811-1814, 1992.

14. K.B.Lyons, J.Kwo, J.F.Dillon, Jr.G.P.Espinosa, M.McGlashan- Powell, A.P.Ramirez, L.F.Schneemeyer. "Search for Circular Dichroism in High-Tc Superconductors", Phys.Rev.Lett. 64, pp.2949-2952, 1990.

15. Lawrence, Taylor W., A. Szoke, and R.B.Laughlin. "Absence of Circular Dichroism in High-Temperature Superconductors", Phys. Rev.Lett. v.69, pp. 1439-1442, 1992.

16. K.B.Lyons, J.F.Dillon, "Broken Time-Reversal Symmetry in Cuprate Superconductors: The Nonreciprocal polar Kerr Effect", Phys. Rev. B, v.47, pp. 8195-8204, 1993.

17. C.Rettori, D.Rao, S.B.Oseroff, G.Amoretti, S-W.Cheong, D.Vier, S.Schultz, M.Tovar, R.D.Zysler, J.E.Schirber, "Internal magnetic field in  $\text{La}_2\text{SrCuO}_4$  observed by electron paramagnetic resonance", Phys. Rev. B47, pp. 8156-8171 ,1993.

18. V.P.Aksenov, K.A.Prokhorov, "Laser Radiation Interaction with Two-Dimensional Quantum Systems", International Conference on Advanced and Laser Technologies (ALT'92) Proceedings, part 2, pp. 134, Moscow, 1992.

## **Laser processing of $Y_1Ba_2Cu_3O_7$ superconducting thin films**

**P.A. Atanasov, R.I. Tomov, V.I. Serbesov**

**Institute of Electronics, Bulgarian Academy of Sciences  
72, Tsarigradsko shose, 1784 Sofia, Bulgaria**

### **ABSTRACT**

Superconducting  $Y_1Ba_2Cu_3O_7$  thin films were prepared by in-situ oxygen plasma-assisted laser deposition. It was revealed that cw  $CO_2$  laser heating of substrate surface may be a method for reduction of particulate density. The buffer layers such as  $Ba(Sr)TiO_3$  and YSZ(111) were successfully experimented for preparation of good superconducting thin films. A multistep superfast  $CO_2$  laser annealing was investigated as a method of modification of the  $Y_1Ba_2Cu_3O_7$  thin films on Si. It is shown that  $N_2$  laser ablation may be a proper technique for patterning  $Y_1Ba_2Cu_3O_7$  thin films. The films were characterized by EDAX, SEM, XRD and Raman spectroscopy.

### **1. INTRODUCTION**

The discovery of high critical-temperature superconducting oxides<sup>1-3</sup> has excited extraordinary research activity. One reason for these efforts lies in the possibility of growing epitaxial layers that are more appropriate for evaluating the basic physical properties and the fundamental interaction mechanisms responsible for the superconductivity in these oxides. Another major reason is the great technological interest in applying high-temperature superconducting (HTSC) films in devices and electronic circuits. The most important characteristics of the new materials is the fact that their optical and electrical properties span the range from an insulating dielectric to a superconductor giving considerable opportunity for fabricating novel devices.

The bulk HTSC materials are hard, brittle, and sensitive to heating cycles and chemicals. So the preparation of HTSC thin films having the desired properties, including both chemical and structural purity, stability, high critical temperature ( $T_c$ ) and current density ( $J_c$ ) has been more complicated than expected. However, applications involving these films, such as hybrid superconducting/semiconducting circuits and microwave/millimeter wave devices, seem to be closer in practice.

Many applications of HTSC thin films require proper surface patterning. The techniques currently investigated include scribing, wet chemical etching, reactive ion beam etching (RIE), ion beam amorfization, selective ion- and electron-beam induced decomposition, and laser processing. It has been demonstrated that laser induced processing permits good localization and material ablation with little or no damage of surrounding material for HTSC.

### **2. LASER DEPOSITION OF Y-Ba-Cu-O THIN FILMS**

Presently, the techniques employed to fabricate HTSC films are evaporation, electron beam evaporation, rf- and dc-sputtering, molecular beam deposition, chemical vapor deposition, spray- or spin-on coating and laser ablation. Laser ablation is distinguished by a number of unique properties and advantages: it is fast, easy, and inexpensive; it permits great experimental versatility and offer excellent control of the correct stoichiometry within the deposited film.

Laser processing is based on the interaction of intense laser radiation with the material surface and the ambient medium surrounding this material. With the HTSC  $O_2$  and  $N_2O$  have been used as a reactive ambient. Physical phenomena occurring when a laser beam is incident upon a material surface depend foremost on the power density, the thermal properties of the material and the material absorptivity at the laser wavelength. At power density above  $10^8 \text{ W.cm}^{-2}$  a plasma plume is formed. The interaction of this plasma with the laser beam and the evaporation source strongly affects the nature of the evaporation and energy coupling to the surface. High laser-power densities and short pulses cause short interaction cycles resulting in congruent ablation of small material volumes.

The type of laser and target-substrate distance affects the film stoichiometry, but no difference between the  $Y_1Ba_2Cu_3O_7$  target and film composition was observed when a small distance (3 - 5 cm) and excimer lasers were used<sup>4,5</sup>. Spatial distribution of laser ablation is strongly forward directed and can be described by a  $\cos^n\theta$  law, where  $n>1$  and  $\theta$  is the angle between the surface normal and the direction of propagation of ablated species.

The first successful preparation of HTSC thin films was made at substrate temperature ( $T_s$ ) of about 300 - 500 °C and as-deposited films were amorphous. The formation of superconducting crystalline phases required subsequent annealing at 800 - 900 °C in oxygen atmosphere<sup>6</sup>. The films deposited had granular structure and were very rough. Such high-temperature treatment enhances the substrate-film chemical interaction as well as migration induced by the stress due to thermal coefficient difference between the substrate and the film. Consequently, a dead layer appears with thickness in order of 100 nm<sup>7</sup>. This limits the choice of substrates and precludes the possibility of obtaining very thin films.

Epitaxial thin films with good superconducting properties were obtained "in situ" at  $T_s = 650 - 750$  °C and by establishing the oxygen partial pressure at 100 - 200 mTorr, which allows elimination of the high-temperature annealing step. Slow cooling and annealing at 400 - 500 °C ensured oxygen incorporation<sup>8,9</sup>. Even at these temperatures certain interdiffusion and worsening of the superconducting properties are observed, especially for more reactive substrates as Si and  $Al_2O_3$ . The "in situ" deposition is implemented at  $T_s = 400 - 550$  °C in the presence of activated oxygen. Smooth superconducting films (100 Å roughness) with very sharp interfaces ( $\sim 10$  Å) have been obtained<sup>10,11</sup>. Up to now, several ways for activation of oxygen have been reported<sup>10,12,13,14</sup>. Defects content strongly decreases at  $T_s$  below 550 °C, but there are quite a few uncrystallized particles on the film surface worsening the superconducting parameters.

### 3. IN-SITU LASER DEPOSITION OF $Y_1Ba_2Cu_3O_7$ THIN FILMS.

The schematic diagrams of our set-up for pulsed laser deposition of HTSC thin films is shown in FIG.1. The XeCl excimer laser radiation (308 nm, 20 ns) focused by a quartz spherical lens is introduced into the vacuum chamber through a

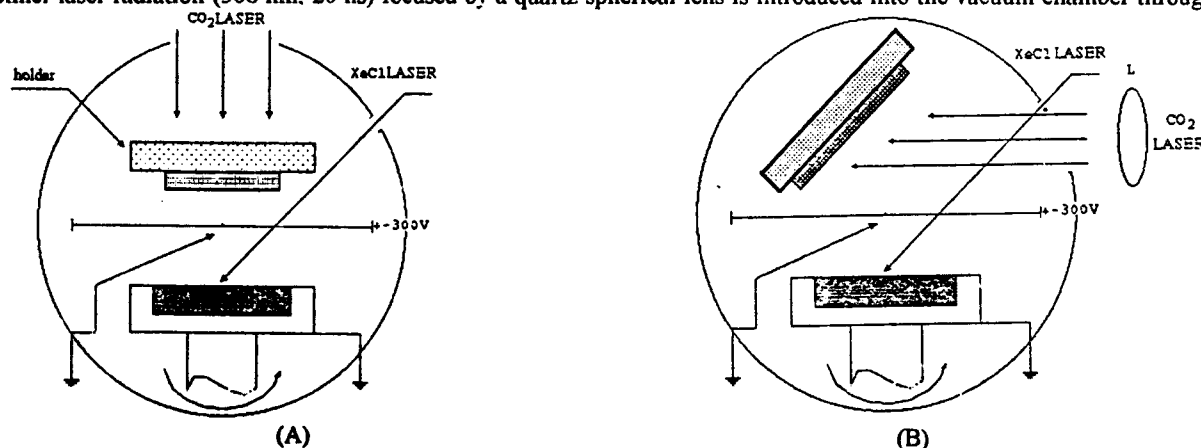


FIG.1 Schematic diagrams of the experimental set-up:  
A - laser irradiation of quartz holder; B - laser irradiation of substrate surface.



density (FIG. 2.a). Although the films were relatively homogeneous and without defects, obviously nonsuperconductive phases existed. XRD investigation showed c-axis perpendicular to the surface with slightly disorientation. The measurements of the critical-current density gave a value of  $7 \cdot 10^5 \text{ A.cm}^{-2}$  at a temperature of 4.2K. Higher substrate temperatures 550 °C and higher partial oxygen pressure (up to 200 mTorr) improved the superconducting properties of the films deposited on  $\text{SrTiO}_3(100)$  substrate considerably (see B1 -  $\Delta T_c = 2\text{K}$ , and  $\Gamma$  up to 2.8). The SEM analysis (FIG.2b) showed substantially lower particulate density. The deposition on substrates with larger lattice percentage mismatch -  $\text{ZrO}_2$  (5.75%, see A2) and  $\text{MgO}$  (8.36%, see B2) at the same temperature resulted in badly crystallized granular films having wide  $\Delta T_c$  and very low resistive ratio. The effect of oxygen deficiency was evidently responsible for the long resistive tail observed in these films. Moreover, when the dc oxygen discharge was not fired and activated oxygen  $\text{O}_2^+$  was absent<sup>19</sup>, superconducting properties were completely destroyed (see A3). Obviously, these substrates require higher substrate temperatures.

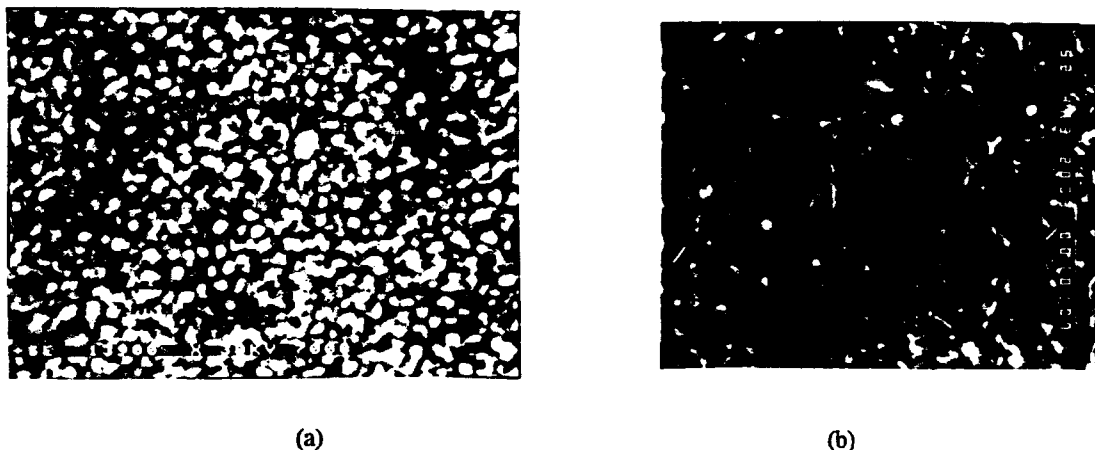


FIG.2 SEM - pictures of  $\text{Y}_1\text{Ba}_2\text{Cu}_3\text{O}_7$  films (a) on  $\text{SrTiO}_3(100)$  - Sample A1; (b) on  $\text{SrTiO}_3(100)$  - Sample B1.

Generation of particulates is a problematic feature of laser ablation. Particulates are 0.1 - 10  $\mu\text{m}$  in size and consist of solidified melt drops or irregularly shaped granular matter. Their incorporation into the film degrade its superconducting properties. Various techniques have been used to eliminate or reduce the density of particulates: deflector vane, electrostatic bias, colliding gas streams, variable laser fluence, spinning disk source, second laser. Generally, the shorter wavelength laser radiation produces films with lower particulate density. Koren et al.<sup>20</sup> gave an explanation in the stronger absorption of shorter wavelength photons by the clusters ejected from the target and their subsequent fragmentation (linear absorption coefficients are 1.2, 1.5, and  $1.7 \times 10^5 \text{ cm}^{-1}$  for 1064, 532, and 355 nm, respectively). An explanation of the particulate densities reduction in the case of samples deposited by substrate surface cw  $\text{CO}_2$  laser heating (scheme B) with respect to those deposited with quartz holder heating (scheme A) can be probably the absorption of IR photons by the photofragments in the excimer laser - produced plasma and on the film surface and their subsequent decomposition, nevertheless of low absorption at 10.6  $\mu\text{m}$  ( $\sim 10^3 \text{ cm}^{-1}$ )<sup>21</sup>.

For microwave application  $\text{MgO}$  has a suitable dielectric constant and a low loss which makes it acceptable for high-frequency application, whereas  $\text{SrTiO}_3$  is unsuitable for this application. However, the larger lattice mismatch percentage of  $\text{MgO}$  (8.36%) in comparison to  $\text{SrTiO}_3$  (1.15%) leads to lower superconducting parameters (see B2). We tried to overcome this problem using  $\text{MgO}$  substrate with magnetron sputtered buffer layer of  $\text{Ba}(\text{Sr})\text{TiO}_3$ . At 650 °C and higher oxygen pressure best results have been obtained - see B3. The Raman spectra of B1 and B3 are shown on FIG.3(a) and FIG.4(a) respectively. The films had almost no oxygen deficiency ( $x < 0.1$  in  $\text{Y}_1\text{Ba}_2\text{Cu}_3\text{O}_{7-x}$ ) and were oriented with a-axis perpendicular to the substrate surface, probably as a result of higher deposition rate -  $V_{\text{dep}} = 1.5 - 2.0 \text{ A.s}^{-1}$ . Mode structure of cw  $\text{CO}_2$  laser spot on the substrate surface (scheme B) caused preheated region on both substrates, where the films were thinner, gray colored and showed lower  $T_c = 88\text{K}$ , wide transition, and  $\Gamma = 1.08$ . Raman spectra of this films areas (FIG.3(b) and FIG.4(b)) showed the c-orientation of the films. As a result regions with different orientation were simultaneously

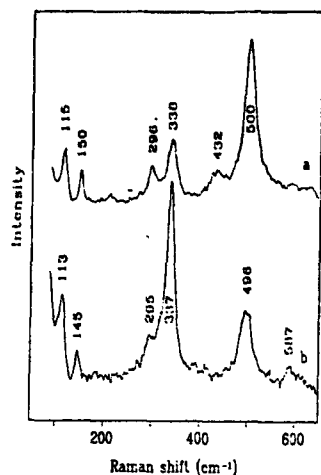


FIG.3 Raman spectra of B1 (a) normal and (b) - preheated region.

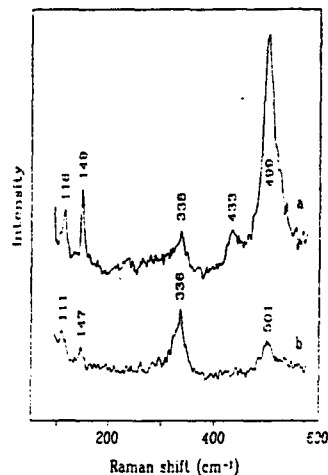


FIG.4 Raman spectra of B3 (a) normal and (b) - preheated region.

deposited on the same substrate. Unfortunately, such deposition results are not controllable and worsening of superconducting properties is undesirable.

#### 4. LASER DEPOSITION OF $Y_1Ba_2Cu_3O_7$ THIN FILMS ON SI WITH YSZ BUFFER LAYER.

The deposition of high-quality HTSC thin films on Si substrates is being intensely investigated by many groups aiming at the integration of HTSC with conventional semiconductor technology. It would have important applications creating high performance hybrid circuits incorporating the best of what superconductors and semiconductors have to offer.

We have tried to prevent the strong substrate-film interaction and migration in the case of Si substrates by use of polycrystalline buffer layer of YSZ(111) deposited on Si(100) by sol-gel method. The thicknesses of YSZ layers were in the range of 100 - 150 nm. The experiments have been carried out in the temperature region of 500 - 600 °C. The best results were obtained at  $T_s = 550$  °C (TABLE I, B4)  $T_c = 88K$ ,  $\Delta T_c = 11K$ . The increasing of  $T_s$  to 600 °C (see B5) causes broader transition below liquid nitrogen temperature probably because of the stronger film-substrate interaction. By reduction of  $T_s$

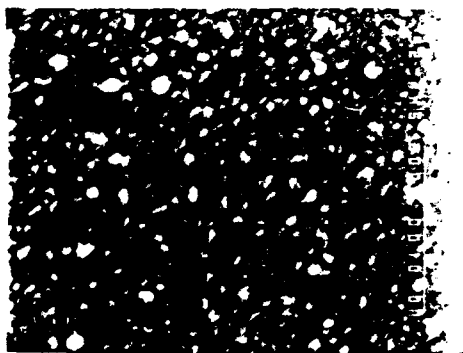


FIG.5 SEM - pictures of  $Y_1Ba_2Cu_3O_7$  film on YSZ/Si - Sample B4.

down to 500 °C (see B6) the worsening of the superconducting properties was observed too. The EDAX analyses of sample B4 showed the strong film-substrate interdiffusion. The SEM picture (FIG.5) of Sample B4 shows clearly the cracks on film surface. Obviously, the YSZ buffer layer had too low packing density to prevent the interdiffusion and stress even at substrate temperature as low as 550 °C.

## 5. MODIFICATION OF THE PROPERTIES OF HTSC YBCO THIN FILMS ON SILICON BY SUPERFAST LASER ANNEALING

In order to avoid deterioration of the film-substrate interface to obtain reversible resistivity control in the chosen dimensions on the coated substrate, a number of groups have prepared  $Y_1Ba_2Cu_3O_7$  films on Si by rapid laser annealing<sup>15,21,22</sup>. This technique allows the films to crystallize by heating only the thin surface layer for a short period of time.

The deposition of the thin films was carried out in vacuum ( $10^{-4}$  Torr) by  $N_2$  laser ablation from stoichiometric  $Y_1Ba_2Cu_3O_7$  target on Si(111) substrate<sup>15</sup>. As-deposited thin films were annealed in oxygen atmosphere ( $p(O_2) = 10^{-2}$  Torr) by cw  $CO_2$  - laser radiation directed onto the film surface. The maximum laser power density was  $40 \text{ W.cm}^{-2}$ . We have measured the film resistivity "in-situ" during the annealing process. Our earlier investigation<sup>15</sup> found that direct cw  $CO_2$  - laser annealing for 8 - 10 sec at  $40 \text{ W.cm}^{-2}$  (annealing temperature  $T_a = 800 - 1000 \text{ °C}$ ) forms structures with presence of metal Si - like transition. Longer laser annealing destroyed the film. Such superfast annealed films were oxygen deficient and not superconductive. We tried to solve the problem of oxygen saturation by using multistep laser annealing instead of the superfast one. Three multistep cycles of laser treatment were tested.

|                      | 1step | 2step | 3step | 4step | 5step | 6step | 7step |
|----------------------|-------|-------|-------|-------|-------|-------|-------|
| cycle 1 - $T_s$ , °C | 420   | 350   | 420   | 350   | 420   |       |       |
| t, s                 | 1     | 60    | 2     | 120   | 2     | -     | -     |
| cycle 2 - $T_s$ , °C | 600   | 400   | 600   | 400   | 600   | 400   |       |
| t, s                 | 2     | 120   | 1     | 60    | 1     | 60    | -     |
| cycle 3 - $T_s$ , °C | 650   | 450   | 650   | 450   | 650   | 450   | 650   |
| t, s                 | 1     | 120   | 1     | 120   | 2     | 120   | 2     |

After the last step the films were held in oxygen atmosphere (1 atm) until room temperature was reached. Formation of an intermediate superconductive phase and interphase interaction at 400 - 450 °C were probably responsible for the saltatory resistivity drop following each superfast annealing step. The film resistivity after cycles 1 and 2 dropped to about 2 Ohm but does not show superconductive transition. The transformation of the film into superconducting state at 79K was achieved by the use of the third annealing cycle (FIG.6). The last step gave the biggest resistivity change and the minimum resistivity value. We believe the fusion of polycrystalline structures to bigger islands took place, creating a chain and containing channels.

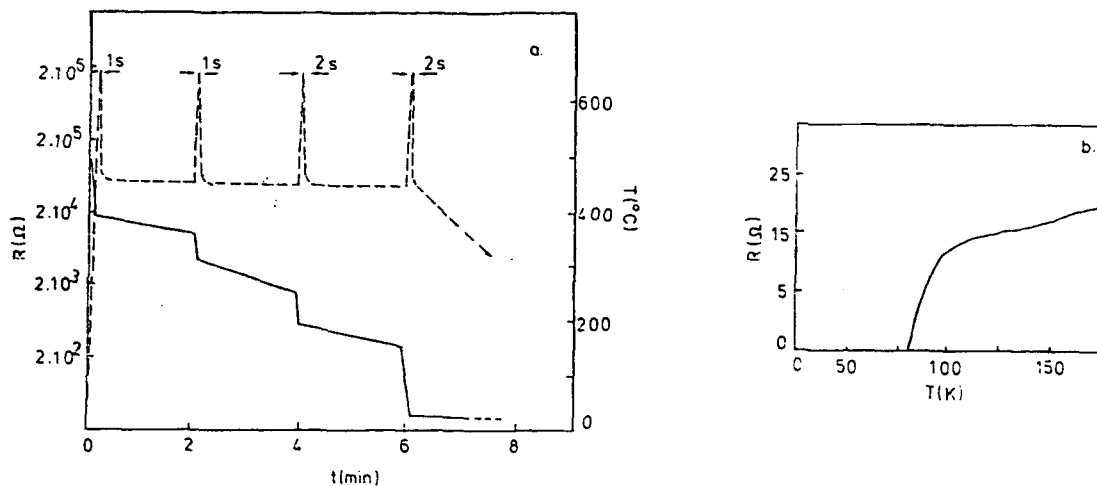


FIG.6 Third laser annealing regime (a), and R-vs-T characteristic of the annealed  $Y_1Ba_2Cu_3O_7$  thin film (b).

## 6. LASER ETCHING OF Y-Ba-Cu-O THIN FILMS WITH NITROGEN LASER

The nitrogen laser used in the etching experiments<sup>23</sup> works at repetition rate of 5 - 20 Hz and produces pulses with the energy 5 mJ at a pulse duration of 6 ns. A spherical quartz lens was implemented to focus the laser beam upon the films. The samples were mounted on X-Y table having increments of 100  $\mu m$  upon X-axis and 1  $\mu m$  upon Y-axis. The displacement rate was varied from 0.5  $mm.s^{-1}$  up to 10  $mm.s^{-1}$ . The incident beam energy density was in the range of 3 - 8  $Jcm^{-2}$ . The experiments were performed in air. No visible alterations of the patterned samples surfaces were observed for rates greater than 10  $mm.s^{-1}$  in the stated incident beam energy range. We have used  $Y_1Ba_2Cu_3O_{7-x}$  films of 0.5 - 1.0  $\mu m$  deposited by co-evaporation on the sapphire and  $SrTiO_3$  substrates and by pulsed laser deposition<sup>15</sup> upon Si substrates. The transition temperatures were in the range of 76 - 92 K.

The SEM micrograph of the  $Y_1Ba_2Cu_3O_7$  thin film deposited on  $SrTiO_3(100)$  and patterned by  $N_2$  laser etching is shown on FIG.7(a). It can be seen that the etched zone in the films has about 30  $\mu m$  width, and there are two regions on the

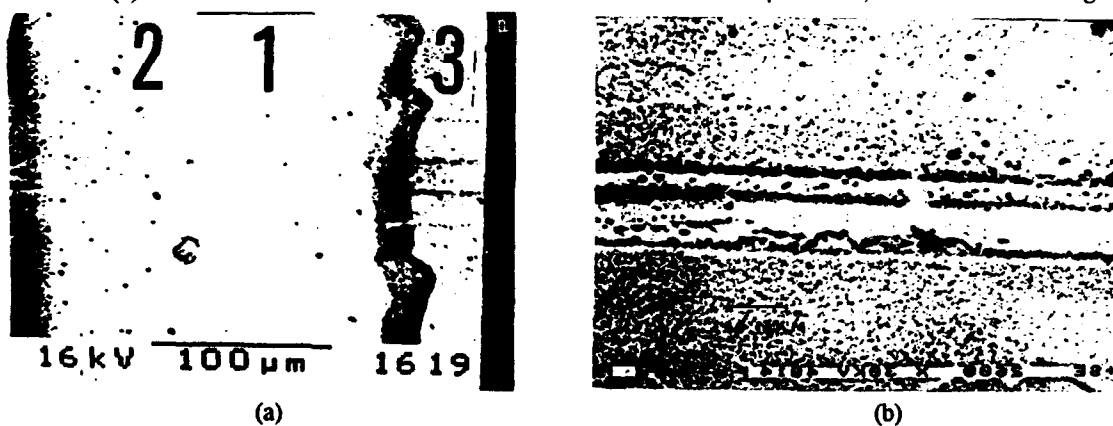


FIG.7 - (a) Top view of 30  $\mu m$  wide track patterned into 0.7  $\mu m$  thick  $Y_1Ba_2Cu_3O_7$  film on  $SrTiO_3$  substrate: (1) - etched zone, (2) - laser beam treated region and (3) - unaffected zone; (b) top view of a 10  $\mu m$  wide track patterned into a 0.8  $\mu m$  thick  $Y_1Ba_2Cu_3O_{7-x}$  film on Si(111).

both sides of it with 200  $\mu\text{m}$  width. The SEM micrograph of the thin film deposited on Si(100) and patterned by  $\text{N}_2$  laser etching is shown on FIG. 7(b). The film composition in the etched and unetched regions was examined by EDAX. The etched region has a conic shape. Region 2 and 3 (FIG. 7a) are not seen here to have any differences between components of the film.

## 7. CONCLUSION

1. Low temperature oxygen plasma assisted in-situ laser deposition technique is a quite proper for obtaining oriented polycrystalline  $\text{Y}_1\text{Ba}_2\text{Cu}_3\text{O}_7$  thin film with good superconducting properties ( $T_c$  up to 90K and  $J_c = 7.10^5 \text{ A.cm}^{-2}$ ). The increase of substrate temperature above 650  $^\circ\text{C}$  allow to obtain quasiepitaxial  $\text{Y}_1\text{Ba}_2\text{Cu}_3\text{O}_7$  thin films. The experiment show that proper buffer layers such as  $\text{Ba}(\text{Sr})\text{TiO}_3$  make possible obtaining of excellent superconducting films on substrates as  $\text{MgO}$ . The use of the polycrystalline YSZ buffer layer on Si(100) still needs parameter optimization. Some attention is paid to problems of characteristic particulate contamination and the ways of their reduction. It is shown that IR laser irradiation onto growing film tends to reduce particulate density.

2. We can conclude that direct laser annealing makes possible restoring of deteriorated superconductive properties of thin films and reproducible modification of film properties.

3. The  $\text{N}_2$  laser ablation is a proper technique for patterning of the HTSC thin films and has advantages over the other techniques: the process is dry, extremely flexible and offers good spatial resolution with no degradation of the film properties.

## 8. REFERENCES

1. J.G.Bednorz, K.A.Muller, "Possible high  $T_c$  superconductivity in Ba-La-Cu-O system," *Z.Phys.* vol.B64, pp.189-193, 1986.

2. K.Wu, J.R.Ashburn, C.J.Torng, P.H.Hor, R.L.Meng, L.Gao, Z.J. Huang, Q.Wang and C.W.Chu, "Superconductivity at 93K in a new mixed-phase Y-Ba-Cu-O compound system at ambient pressure," *Phys.Rev.Let.* vol.58, pp.908-910, 1987.

3. Z.Z.Sheng and A.M.Hermann, "Bulk superconductivity at 120K in the Tl-Ca/Ba-Cu-O system," *Nature* vol.332, pp.138-139, 1988.

4. D.Dijkkamp, T.Venkatesan, X.D.Wu, S.Shaheen, N.Jisrawi, Y.H.Min-Lee, W.L.McLean., and M.Croft. "Preparation of Y-Ba-Cu-oxye superconductor thin films using pulsed laser evaporation from high  $T_c$  bulk material," *Appl. Phys.Lett.* vol.51, pp.619-621, 1987.

5. T.Venkatesan, X.D.Wu, A.Inam and J.B.Wachtman, "Observation of two disting components during pulsed laser deposition of high  $T_c$  superconducting films," *Appl.Phys.Lett.* vol.52, pp.1193-1195, 1988.

6. A.M. DeSantolo, M.L. Mandich, S. Sunshine, and J.A. Davidson, "Preparation of high  $T_c$  and  $J_c$  films of  $\text{Ba}_2\text{YCu}_3\text{O}_7$  using laser evaporation of composite target containing  $\text{BaF}_2$ ," *Appl.Phys.Lett.* vol.52, pp.1995-1997, 1988.

7. X.D. Wu, A. Inam, T. Venkatesan, C.C. Chang, E.W. Chase, P. Barboux, J.M. Tarascon, and B. Wilkens, "Low temperature preparation of high  $T_c$  superconducting thin films," *Appl.Phys.Lett* vol.52, pp.754-756, 1988.

8. B. Roas, L. Schultz, and G.Endres, "Epitaxial growth of  $\text{YBa}_2\text{Cu}_3\text{O}_{7-x}$  thin films by a laser evaporation process," *Appl.Phys.Lett.* vol.53, pp.1557-1559, 1988.

9. G. Koren, A. Gupta, E.A. Giess, A. Segmuller, and R.B. Labowitz, "Epitaxial films of  $\text{YBa}_2\text{Cu}_3\text{O}_{7-\delta}$  on  $\text{NdGaO}_3$ ,  $\text{LaGaO}_3$  and  $\text{SrTiO}_3$  substrates deposited by laser ablation," *Appl.Phys.Lett.* vol.54, pp.1054-1056, 1989.
10. S. Witanachchi, H.S. Kwock, X.W. Wang, and D.T.Shaw, "Deposition of superconducting Y-Ba-Cu-O films at 400 °C without post-annealing," *Appl.Phys.Lett.* vol.53, pp.234-236, 1988.
11. R.K. Singh, J. Narayan, A.K. Singh and J. Krishnaswamy, "In situ processing of epitaxial Y-Ba-Cu-O high  $T_c$  superconducting films on (100) $\text{SrTiO}_3$  and (100) $\text{YS-ZrO}_2$  substrates at 500 - 650 °C," *Appl.Phys.Lett.* vol. 54, pp.2271-2273, 1989.
12. G.Koren, E.Polturak, B.Fisher, and D.Cohen, "Highly oriented as-deposited superconducting laser ablated thin films of  $\text{YBa}_2\text{Cu}_3\text{O}_{7-\delta}$  on  $\text{SrTiO}_3$ , zirconia, and Si substrates," *Appl.Phys.Lett.* vol.53, pp.2330-2332, 1988.
13. G.Koren, A.Gupta, and R.J.Baseman, "Role of atomic oxygen in the low-temperature growth of  $\text{YBa}_2\text{Cu}_3\text{O}_{7-\delta}$  thin films by laser ablation deposition," *Appl.Phys.Lett.* vol.54, pp.1920-1922, 1989.
14. An Cheng-wu, Fan Yong-chang, Lu Dong-sheng and Li Zai-guang, "In situ laser processing of high  $T_c$  superconducting thin films at 450 - 550 °C," *Chinese Science Bull.* vol.37, pp.1483-1486, 1992.
15. V.Serbezov, St.Benacka, D.Hadgiev, P.Atanasov, N.Elektronov, V.Smatko, and V.Stribik, "Structure and superconducting properties of  $\text{YBa}_2\text{Cu}_3\text{O}_{7-x}$  films prepared by nitrogen laser evaporation and  $\text{CO}_2$  laser annealing in oxygen," *J.Appl.Phys.* vol.67, pp.6953-6957, 1990.
16. E.Dyer, I.Assa, P.H.Key, and P.Monk, "A cw  $\text{CO}_2$  laser substrate heater for superconducting thin film deposition," *Supercond.Sci.Technol.* vol.3, pp.472-475, 1990.
17. K.H.Wu, C.L.Lee, J.Y.Juang, T.M.Uen and Y.S.Gou, "In situ growth of  $\text{YBa}_2\text{Cu}_3\text{O}_{7-x}$  superconducting thin films using a pulsed neodymium:yttrium aluminium garnet laser with  $\text{CO}_2$  laser heated substrates," *Appl.Phys.Lett.* vol.58, pp.1089-1091, 1991.
18. P.A.Atanasov, R.I.Tomov, and V.S.Serbesov, "Plasma assisted in-situ laser deposition of  $\text{YBa}_2\text{Cu}_3\text{O}_{7-x}$  superconducting thin films with laser heating and annealing," *Vacuum*, in press.
19. R.K. Singh, L. Ganapathi, P. Tiwari, and J. Narayan, "Effect of processing geometry in oxygen incorporation and in situ formation of  $\text{YBa}_2\text{Cu}_3\text{O}_7$  superconducting thin films by pulsed laser evaporation technique," *Appl. Phys.Lett.* vol.55, pp.2351-2353, 1989.
20. G.Koren, A.Gupta, R.J.Baseman, M.I.Lutwyche, and R.B.Laibowitz, "Laser wavelength dependent properties of  $\text{YBa}_2\text{Cu}_3\text{O}_{7-\delta}$  thin films deposited by laser ablation," *Appl.Phys.Lett.*vol.55, pp.2450-2452, 1989.
21. S.Otsubo, T.Minimakawa, Y.Yonezawa, T.Maeda, A.Morimoto, and T.Shimitzu, "Crystallization induced by laser irradiation in Ba-Y-Cu-O superconducting films prepared by laser ablation," *Japan.J.Appl.Phys.* vol.28, pp.2211, 1989.
22. T.Minimakawa, Y.Yonezawa, S.Otsubo, T.Maeda, A.Moto, A.Morimoto, and T.Shimizu, "Preparation of  $\text{Ba}_2\text{YCu}_3\text{O}_x$  superconducting films by laser evaporation and rapid laser annealing," *Japan.J.Appl.Phys.* vol.27, L619-621, 1988.
23. V.Serbesov and P.A.Atanasov, "Nitrogen laser with high pulse and average power," *Meas.Sci.Technol* vol.1, pp.601-604, 1990.

## Structural transformation in laser processing of steel

A. Barborica, V.S. Teodorescu\*, I.N. Mihailescu\*, G. Daurelio\*\*, L. Cento\*\*

University of Bucharest, Physics Department, P.O.Box MG-11, RO-76900 Bucharest-Romania

\*Institute of Atomic Physics, Laser Department P.O.Box MG-6, RO-76900 Bucharest-Romania

\*\*Centro Laser Bari, Via de Blasio 1, 70123 Bari-Italia

### ABSTRACT

Electron microscopy studies are performed on steel samples submitted to high-intensity CO<sub>2</sub> laser irradiation. The results are analysed in connection with the macroscopic characteristics of the laser irradiation bead as against the required performances for a quality laser welding. An appropriate description of the experimental evidence is obtained through the intermediary of a 2-D numerical analysis of the cooling dynamics subsequent laser irradiation.

### 1. INTRODUCTION

There is a large literature devoted to the laser processing of metals (see e.g. <sup>1-4</sup>). The most of these works approach this topic from the point of view of the quality and overall performances of the respective laser operations only - i.e. cutting, drilling and welding. The main purpose of this paper is to establish a connection among the macroscopic characteristics of the irradiated zone and the

modifications induced by laser irradiation at a microscopic scale. We have also tried to obtain an appropriate description of the thermal regime of the zones submitted to laser irradiation in agreement with the experimental evidence at both macroscopic as well as microscopic scale.

### 2. EXPERIMENTAL

In experiments, we have used 3mm thick laminated sheets of: AISI 304, AISI 316 and AISI 430 steel. The samples were irradiated with a BOC TEA-CO<sub>2</sub> laser with axial flow yielding 2 kW in CW. As depicted in fig. 1a, the laser beam (1) is directed through a 45° tilting mirror (2) to the focusing head or to a powermeter (3). The orientation of the mirror is controlled through an electro-pneumatical mechanism. The focusing head has another mirror at 45° (3) which drives the laser beam down to a KCl focusing lens (5) of plane-convex type,

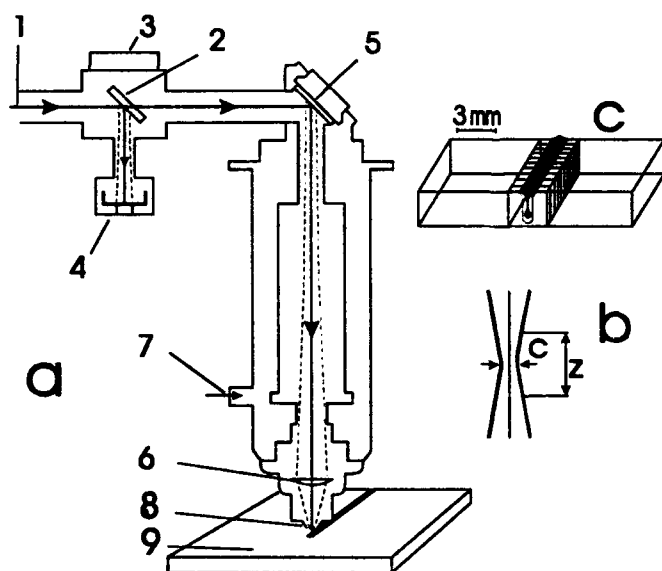


Fig. 1. a) - Schematic depiction of the experimental set-up; (1) - CO<sub>2</sub> laser beam; (2) - tilting mirror; (3) - electro-pneumatic valve; (4) - power meter; (5) - mirror at 45°; (6) - focusing KCl lens; (7) - gas inlet; (8) - gas outlet; (9) - steel plate. b) - Shape and size of the focus; at P=2kW laser power, the effective diameter c is 600μm and the depth z of the focus is 5.2mm. c) - Metallographic, TEM and SEM specimen cutting.

having a focal length of  $f=75\text{mm}$ , and a diameter of  $D=38\text{mm}$ . The beam is focused onto the steel plate (9), the focus having at 2 kW laser power an effective diameter of  $c=600\mu\text{m}$  and a depth of  $z=5.2\text{ mm}$  (see fig 1b). The steel plate is linearly moved at a constant speed of  $v=0.6\text{-}2\text{cm}\cdot\text{s}^{-1}$ . In order to prevent the development of oxides and burning ignition as a consequence of the laser heating and melting, an axial jet of inert gas ( $\text{CO}_2$ , He or  $\text{N}_2$ ) is insured at a flow rate of  $0.5\text{-}1.3\text{ l}\cdot\text{s}^{-1}$ . According to the dimension of the gas outlet (7) of  $\varnothing 4.5\text{-}13.5\text{ mm}$ , the maximum flow rate is chosen in order to avoid melt removal.

In a first stage we have tested the relative mechanical performances (traction, bending and fatigue) of the laser treated zones as against the characteristics of the virgin material. The results of these studies are given in detail elsewhere<sup>5</sup>. We have identified in every case the laser irradiation regimes which result in the best mechanical performances of the treated zones. For the purpose of this analysis we have selected the case of AISI 430 (DIN 14016) stainless steel (having 16+18% Cr and max. 0.12% C, 1.00% Mn, 1.00% Si, 0.030% S, 0.040% P). It was found out that for this type of steel the best mechanical performances are obtained by scanning across surface with a speed of  $v=2\text{ cm}\cdot\text{s}^{-1}$  a 2kW CW  $\text{CO}_2$  laser beam under a gas jet of He at a flow rate of  $0.8\text{ l}\cdot\text{s}^{-1}$ . We stress upon the fact that the general observations of our microscopic investigations are actually identical for all the investigated steel marks. To the view of performing metallographic observations, specimens were cut from the irradiated samples as shown in fig. 1c and submitted to an oxalic acid treatment. On similar specimens were performed microhardness investigations at different locations. Samples were studied by Scanning Electron Microscopy (SEM), Transmission Electron Microscopy (TEM) and Selected Area Electron Diffraction (SAED) investigations on laser irradiated and heat affected zones using a JEOL TEMSCAN 200 CX electron microscope operating at 200 kV. The TEM specimens were thinned in a bath of 5% percloric acid in glacial acetic acid.

### 3. RESULTS

It is to be pointed out that a plasma plume was visible during irradiation in the vicinity of the laser impact region.

Due to the significance for laser welding, we shall refer to the case of almost complete penetration of the metal plates. There is no metal loose in this case by pouring and we can study the structural transformations caused by laser irradiation, unperturbed by material removal. On the top side of the irradiated steel plates, one observes at visual inspection a uniform bead 1.5 mm wide indicating the melting of steel. There is no evidence of melting on the bottom side of the plates. Also, there is no evidence of a significant removal of material. Metallographic observations, presented in fig. 2, showed that the melted zone, as identified by the continuity of the microscopic aspect of the surface layer (melted according to visual observations) to the inner zones, extends into the 3mm thick steel plate down to 2.2 mm. It has to be noted that the metal is profoundly melted while the melt width remains narrow (from

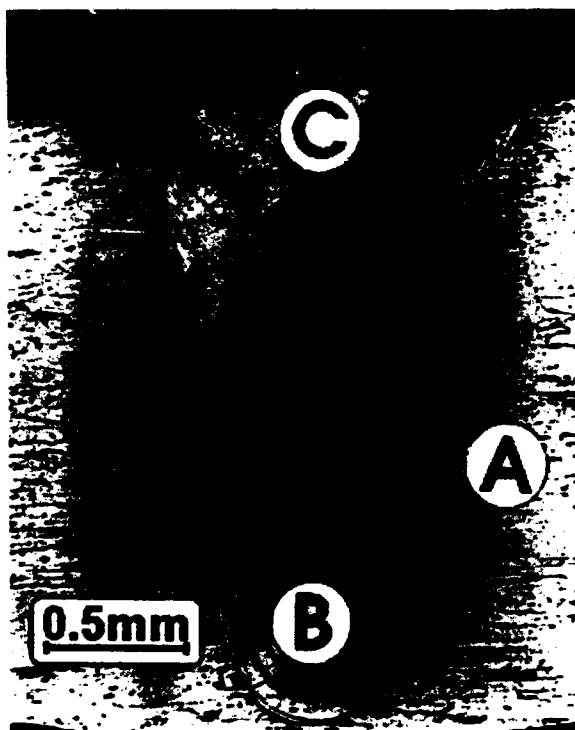


Fig. 2. Optical microscopy image of a cross-section through the laser irradiated zone.



fig. 2 one notes a ratio of about 3:1). One can distinguish in fig. 2 three regions with a different microscopic aspect, denoted by A, B, and C, respectively. The zone A keeps unmelted and mostly preserves the initial structure of the steel, while the zones B and C undergo melting. We performed SEM (fig. 3), TEM (figs. 4, 5) and SAED (figs. 6a-b) investigations of regions in the zones A and B. We observe that:

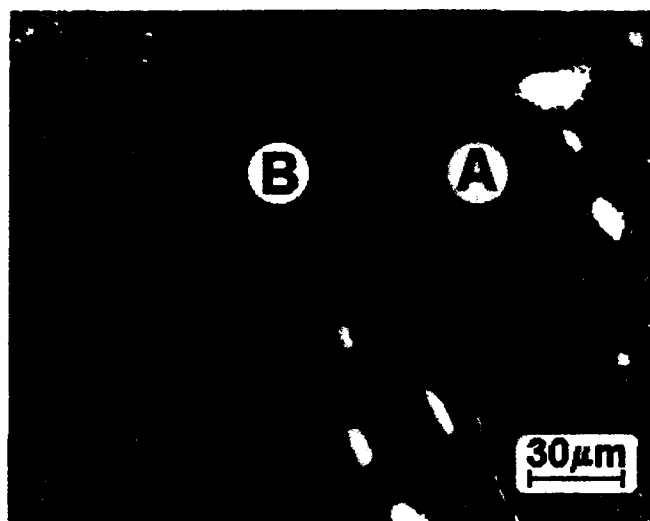


Fig. 3 SEM image of the boundary between zones A and B in fig. 2.

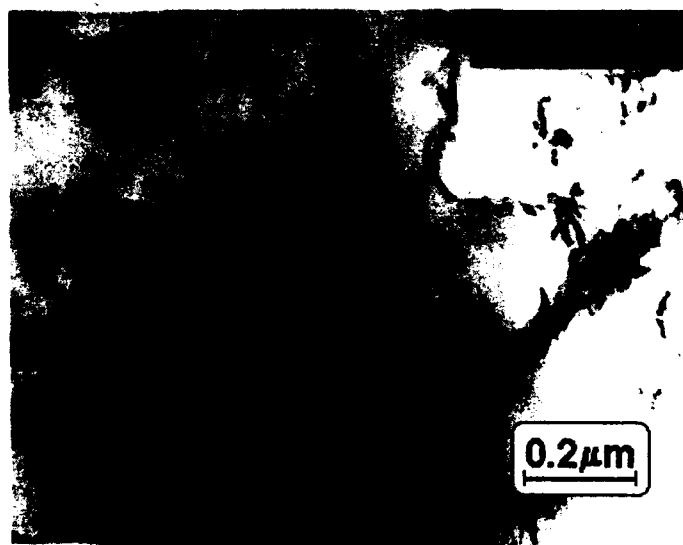


Fig. 4. TEM image of a light-colour region in the zone denoted by B in fig. 2.

i) The steel preserves its initial ferritic structure in zone A (fig. 3), with large precipitates (tens of microns size) and a density of about  $10^8 \text{ cm}^{-3}$ . The precipitates are disposed in rows with a preferential orientation parallel to the rolling direction. Further SAED investigations showed that the precipitates are carbides of the type  $M_6C$ ,  $M_{23}C_6$  and  $M_7C_3$ .

ii) A dense and uniform distribution of small precipitates with a density of about  $10^{12} \text{ cm}^{-3}$  is observed in zone B (fig. 3). The dimension of the precipitates is of 50-100 nm (figs. 4 and 5). SAED investigations of the light-coloured regions (fig. 4) cannot reveal consistent structural information in order to index their structure in a definite way. However, the extra reflections suggest a  $M_2C$ -type structure (fig. 6a);

iii) The zone B, pear shaped (fig. 2), exhibits several dark lines. One observes from fig. 5 precipitates having a larger size, of about 100nm, i.e. almost twice the size of the precipitates in the lighter zones (fig. 4). The precipitates were identified as  $\epsilon$ -carbide ( $M_2C$ ), most probably  $Cr_2C$  (fig. 6b);

iv) The boundary between zones A and B is sharp (figs. 2,3). On the zone B side, the vicinity of the boundary presents no structure variations (fig. 2,3), while on the other side, within zone A, there is a structure change extending to 100μm from the boundary (fig. 2);

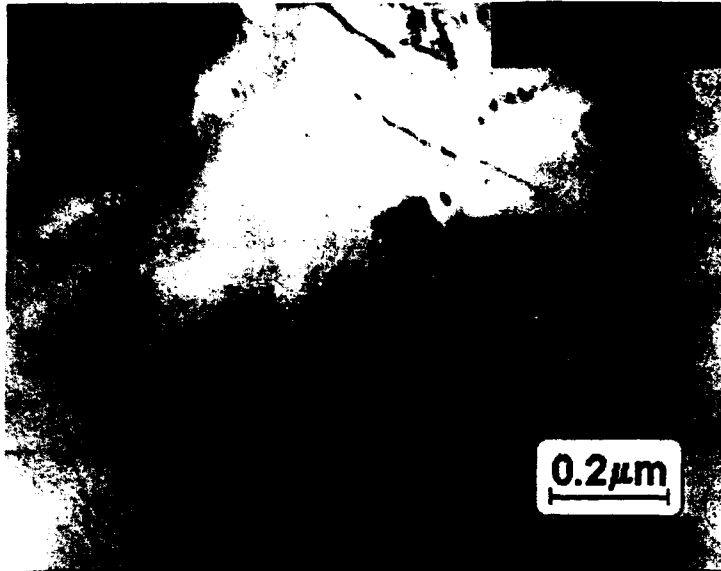


Fig. 5 TEM image of a dark-colour line in the zone denoted by B in fig. 2.

v) Microhardness tests<sup>5</sup> indicated that the zone C has the highest hardness as compared to the zones A and B. This can be related to the fact that the structure is martensitic.

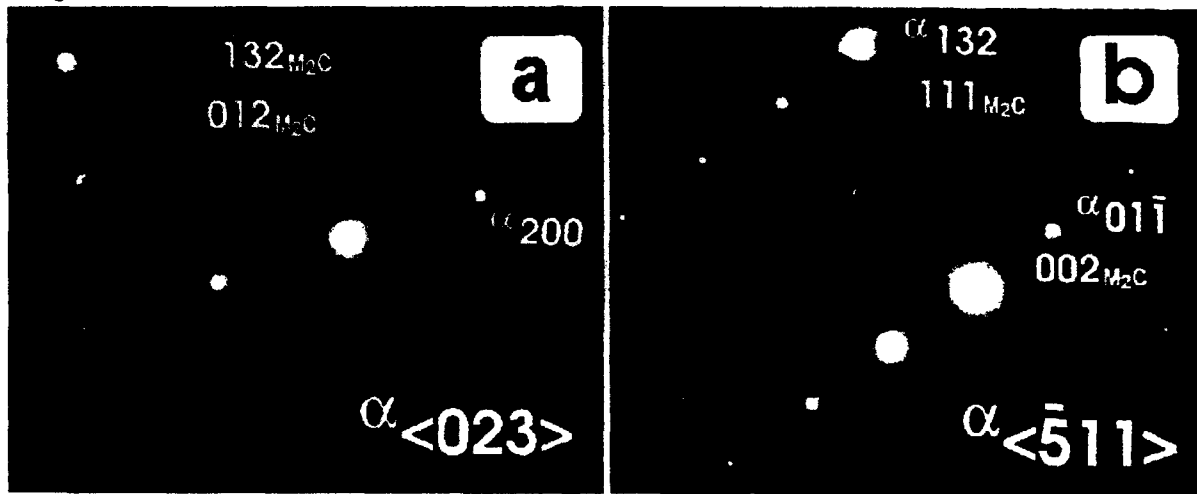


Fig. 6 a,b SAED images corresponding to the zones shown in fig. 4 and fig. 5, respectively.

#### 4. 2-D NUMERICAL ANALYSIS

We put in a finite difference form the heat-flow equation choosing a rectangular spatial grid with a  $100 \mu\text{m}$  step<sup>3,6,7</sup>. The time step was recalculated at each iteration, in order to insure the maximum convergence speed still maintaining the numerical stability. We took into account the temperature dependence of the material's parameters, including particular transitions, as the one at the Curie point of steel ( $T_c=670^\circ\text{C}$ )<sup>8</sup>. We did not consider approximate analytical formulas for the temperature dependence of the material's parameters, but experimental curves digitized in form of tables. The first order phase transformations, accompanied by latent heat, that lead to singularities in the specific heat are treated as peaks with finite height and non zero widths. This means that the

phase transition is considered to take place over a non zero temperature interval, not at a fixed temperature.

We considered two types of losses: the radiative losses and the convective losses. The radiative losses follow the well-known Stefan-Boltzmann law. On the upper side of the sample there is a forced gas flow, leading to a higher convective exchange as compared to the bottom side. Moreover, due to the horizontal orientation of the bottom side, a steady air current can't develop due to the thermal gradients.

The absorptivity at  $\lambda=10.6\mu\text{m}$  is less than 15%<sup>2,5</sup>. At the given incident laser intensities, the metal rapidly melts in depth, and a thin layer vaporizes, the laser radiation falling on a surface at the vaporization temperature,  $T_v=3070^\circ\text{C}$ , at which one would expect an increased absorption.

For the first set of our simulations, we have assumed that the absorption of the radiation takes place at the sample surface, the value of absorptivity being of about 15% and we neglected the melt flow. The simulations performed under this hypothesis indicated that: i) the metal reaches the vaporization temperature and a certain amount of it vaporizes; ii) the calculated temperature distribution is not in accordance with the microscopic experimental evidence, i.e. a deep and narrow melted zone.

We therefore assumed that the vaporized material 'pushes' laterally the melt and a keyhole develops into the material, the absorption taking place deeper and deeper into the bulk. Since a combined analysis, thermal and hydrodynamical, of the processes taking place during laser irradiation, is very difficult to accomplish, we started our thermal analysis immediately after the end of the irradiation of a certain location, during the subsequent cooling process. A much lower flow is expected in the melted phase during the cooling process as compared to the flow during the action of the laser radiation. Moreover, due to the forced cooling of the upper side of the sample, the solidification takes place in a very short time, and that is why we neglected the heat transport by melt flow for the second set of simulations we performed.

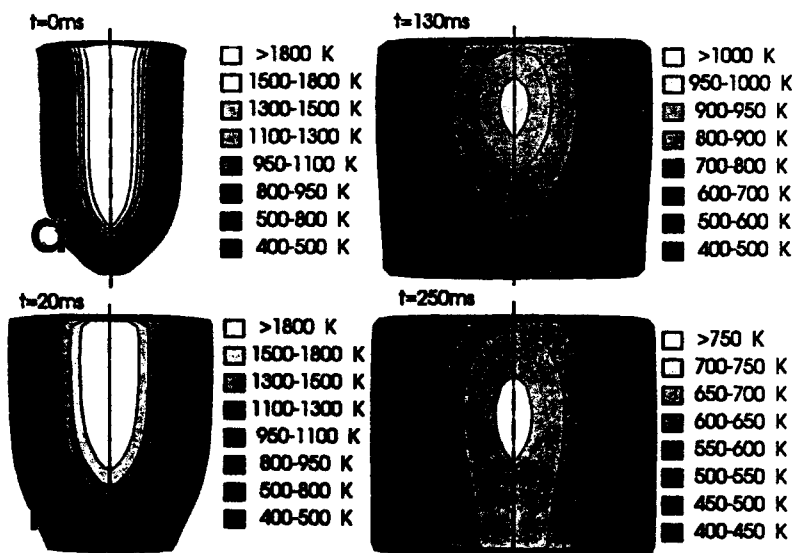


Fig. 7. Temperature distribution within the sample for several values of the time elapsed from the end of the irradiation and start of the cooling process.

The overall absorption of the laser radiation is increased, since it takes place deep into the sample and the radiation reflects several times on the keyhole sides. Also, due to the movement of the steel plate, the absorption of the laser radiation takes place on an inclined plane, which has a larger area than the horizontal spot. This leads to a lower local incident laser intensity, diminishing the quantity of material which is vaporized. Therefore less of the incident heat is spent to form vapours which are ejected through the keyhole, increasing the overall efficiency of the laser radiation coupling. For the second set of

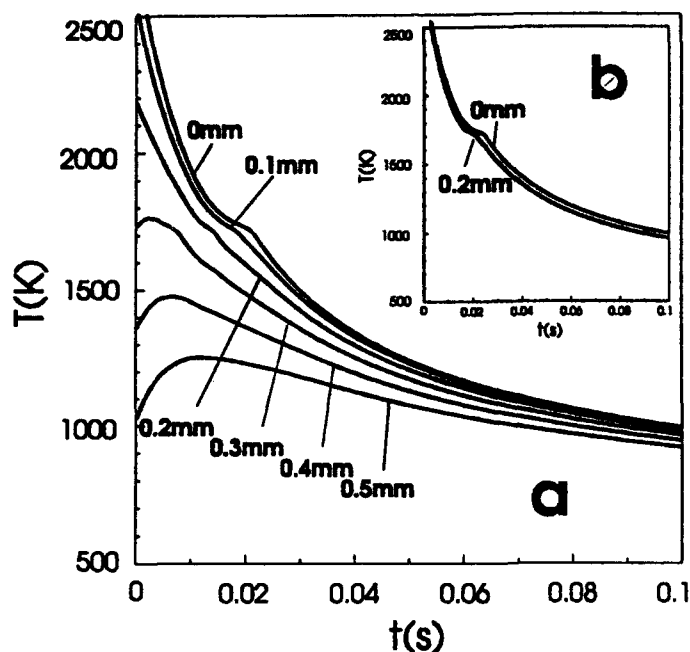


Fig 8 a) - Time evolution of the temperature at a point within the irradiation spot, located on the beam axis, at a distance from the sample surface of  $z_0=0$  and  $z_0=0.2$  mm corresponding to the zone C in fig. 2. b) - Time evolution of the temperature at different distances from the beam axis. The distance from the sample surface is  $z_0=1.5$  mm corresponding to the centre of the zone B.

closely congruent to the dynamics of the cooling process as inferred by the numerical analysis. Thus, the unmelted zone A kept its initial morphology, excepting a region of about  $100\mu\text{m}$  close to the boundary to zone B. This region reaches a temperature higher than  $600^\circ\text{C}$  (fig. 8), for which according to ref. <sup>8</sup>, morphological transformations are promoted.

According again to the evidence in fig. 2, the material in the zone B is melted during irradiation. This observation is confirmed by the results of the numerical simulation. We thus note that the material in zone B remains liquid for a duration of up to 25ms. As a consequence, the carbides within this zone completely dissolve. One special note follows from the almost perfect similitude between the isothermal lines obtained from numerical simulation, represented in our figure 7, and the dark lines observed in fig. 2. The carbide precipitates regrow during the cooling process, their size and morphology being strongly influenced by the cooling rate. The numerical simulations also show that the melted material entirely solidifies in about 25ms and the temperature decreases below  $600^\circ\text{C}$  in less than 100 ms after the end of the irradiation. This cooling proceeds much faster than the cooling during usual manufacturing of steel. That is why the precipitate size in the zone B is so small, of about  $50+100$  nm only. For comparison, we observe that in the region A, where the material does not undergo melting, the precipitates are hundreds of times larger, i.e. having typical dimensions of tens of microns (see fig. 3 and compare it to figs. 4 and 5). The precipitates in zone B are found in two forms: i) small precipitates, of about 50 nm, in the light-coloured regions; ii) better grown precipitates, of about 100 nm which form the dark lines (fig. 2). As the SAED images (figs. 6a, 6b) of the two types of precipitates indicates, the smaller ones have a structure that is not very well

the simulations, we have therefore assumed that about 50% of the incident intensity is absorbed into the sample.

As initial data for the analysis during the cooling process, we assumed that there is a U-shaped pocket of liquid which has a temperature close to the vaporization point (fig. 7a) along its vertical axis.

The shape of the melted (fig. 7a) zone is close to the experimentally observed one (fig. 2). We observe that in the regions corresponding to zone C, close to the upper surface, the cooling rate is high, exceeding the threshold value<sup>8</sup> of about  $500 \text{ Ks}^{-1}$  (fig. 8b), for which a martensitic structure is obtained. The cooling in the central zones (fig. 8a), proceeds at a lower rate, and one has to note the constant temperature levels at the transition points.

## 5. DISCUSSION

To start with, we note that the morphological aspect of the different zones affected by the laser treatment is

defined, of  $M_2C$  type. The larger ones exhibit more reflections on different crystalline planes, proving a more regular structure of the precipitates which are most probably  $Cr_2C$ .

One special note follows from the perfect similitude between the isothermal lines obtained from our numerical analysis, represented in fig. 7, and the dark lines observed in fig. 2. We foresee therefore to systematically apply this analysis for preliminary of the best irradiation regimes to obtain high quality welding.

## 6. CONCLUSIONS

We have characterized on a microscopic scale the structural modifications the fast cooling subsequent to laser irradiation is causing. We emphasize upon the fact that the observed structures support the experimental results showing a good mechanical behaviour of the formed structures. One important remark is that our numerical analysis predicts thermal evolutions in both qualitative as well as quantitative agreement with the microscopic experimental evidence.

## 7. REFERENCES

1. J. F. Ready, *Effects of High Power Laser Irradiation*, Academic Press, N.Y., 1971.
2. W. W. Duley, *CO<sub>2</sub> Lasers, Effects and Applications*, Academic Press, New York, 1976; W. Duley, *Laser Processing and Analysis of Materials*, Plenum Press, New York, London, 1983.
3. W.M. Steen, *Laser Materials Processing*, Springer-Verlag, London, Berlin, 1991.
4. A.M. Prokhorov, V.I. Konov, I. Ursu, and I.N. Mihailescu, *Laser Heating of Metals*, Adam Hilger - IOP Press, Bristol, Philadelphia, N.Y., 1990.
5. G. Daurelio, L. Cento, and C. Esposito, *2 kW CO<sub>2</sub> Laser Welding of Carbon and Stainless Steel*, Technical Report, Centro Laser - Bari, Sept. 1982.
6. V.P. Isachenko, V.A. Osipova, and A.S. Sukomel, *Heat Transfer*, Mir publishers, Moscow, 1977.
7. G. I. Marchiuk, *Methods of Numerical Analysis*, Nauk, Moscow, 1980.
8. C. S. Barrett and T.B. Massalski, *Structure of Metals*, Pergamon Press, Oxford, N.Y., Sydney, Paris 1980.

Integration of photochemical processes of  
silicon surface cleaning with deposition  
of thin solid films

Alekhan A.P.<sup>\*</sup>, Bokov Yu.S.<sup>\*</sup>, V'iukov L.A.<sup>\*</sup>, Markeev A.M.<sup>\*</sup>,  
Nevolin V.N.<sup>\*\*</sup>, Samsonov N.S.<sup>\*</sup>, Fominski V.Yu.<sup>\*\*</sup>

<sup>\*</sup> Zelenograd Institute of Physical Problems, Moscow, 103460

<sup>\*\*</sup> Moscow Engineering Physics Institute, 115409, Moscow,  
Kashirskoe shosse, 31

ABSTRACT

The possibility of a low temperature technique development including combined photochemical processes of the silicon substrate cleaning, chemical vapor deposition (CVD) and post treatment of  $\text{SiO}_2$  has been demonstrated.

1. INTRODUCTION

Photochemical processes due to the absence of the high energy and charged particles, high migration length of active species are one of the most promising low temperature techniques for chemical vapor deposition (CVD) of various functional layers in microelectronics technology,<sup>1,2</sup> e.g. for CVD of  $\text{SiO}_2$  and  $\text{Si}_3\text{N}_4$  as gate dielectrics, insulating and passivating coatings. Thus some experimental works have been done on photo-CVD of  $\text{SiO}_2$  using such reagents as  $\text{SiH}_4$  and  $\text{N}_2\text{O}$  under low pressure mercury lamp<sup>2,3</sup> and ArF excimer laser radiation<sup>4</sup>,  $\text{Si}_2\text{H}_6$  and  $\text{N}_2\text{O}$  under ArF laser radiation<sup>5</sup>,  $\text{SiH}_4/\text{Si}_2\text{H}_6$  and  $\text{O}_2$  under deuterium lamp radiation<sup>6,7</sup>. However, in the experiments on photo-CVD of  $\text{SiO}_2$  it has been paid less attention to investigation of the possibilities of the photochemical processes for the substrate cleaning and film post-treatment.<sup>8,9</sup>

The photons from the ultraviolet (UV) and vacuum ultraviolet (VUV) region can induce or dissociation of the wide range of substances ( $\text{O}_2$ ,  $\text{N}_2\text{O}$ ,  $\text{F}_2$ ,  $\text{NF}_3$ ,  $\text{Si}_x\text{H}_y$ ,  $\text{C}_x\text{H}_y$ ) with the formation of

chemically active particles at low temperatures. Thus, in principle, the development of a technique combining the photochemical processes for the substrate cleaning, deposition and post-treatment of  $\text{SiO}_2$  is possible and this work is devoted to this problem. In the process development it is important to exclude the contact of the sample with the external environment and to provide the substrate surface or deposited layer analysis on the various stages of the processing.

## 2. EXPERIMENTAL

In this work a special two-module set-up containing a photochemical technological module and an analytical module of X-ray photoelectron spectroscopy (XPS) was developed for the investigation of combined photochemical processes of the silicon substrate cleaning, silicon dioxide photo-CVD and post-treatment (Fig.1.).

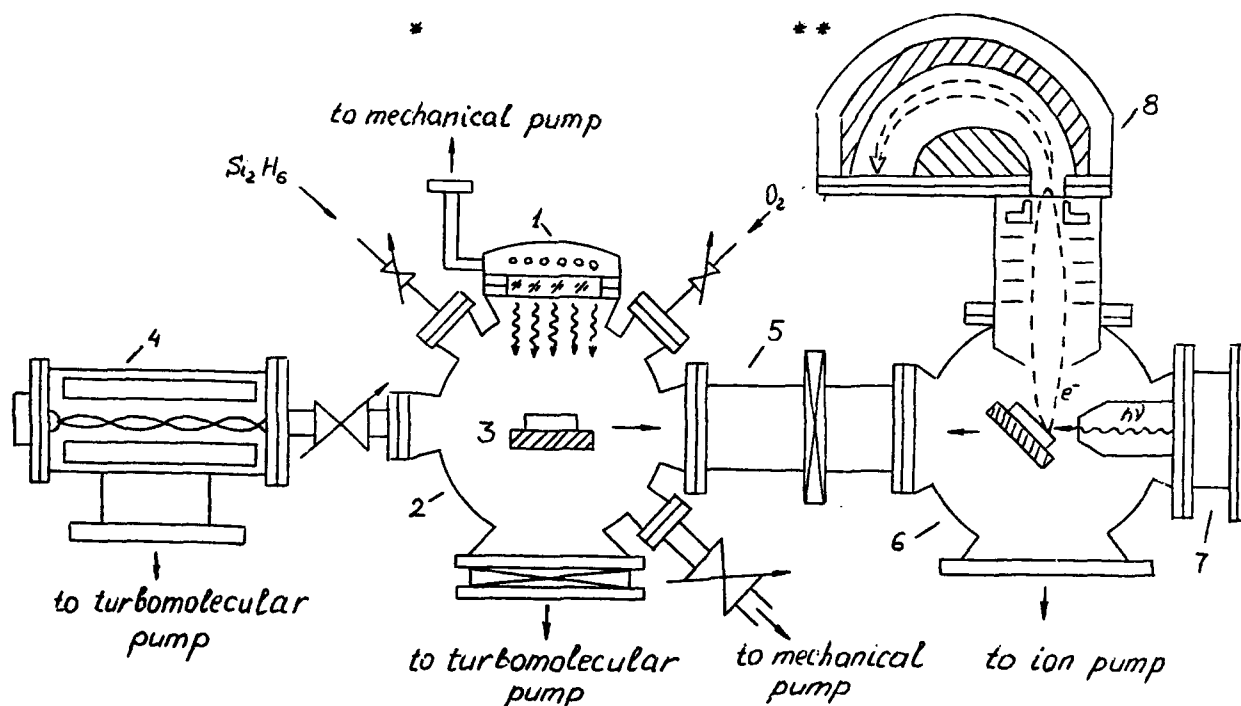


Fig.1. Principle scheme of experimental system: \* - photochemical technological module, \*\* - XPS-analytical module  
1-source of VUV-radiation; 2-reaction chamber; 3-sample-holder; 4-quadrupole mass-spectrometer; 5-sample transfer system; 6-analytical chamber; 7- X-ray source; 8-semispherical electron energy analyzer.

The (100) n-type silicon wafers with the resistivity of  $4.5 \Omega \cdot \text{cm}$  were used as the substrates. Firstly, the substrates were pretreated in 1% HF water solution. Then the substrates were VUV-irradiated in oxygen to study the carbon contaminants removal processes. The deuterium lamp was used as VUV-radiation source since its maximum intensity was in the region of  $\lambda=160 \text{ nm}$  coinciding with oxygen maximum absorption and allowed to generate the most chemically active  $\text{O}(^1\text{D})$  atoms. The  $\text{D}_2$ -lamp radiation power density in the region of 115-200 nm was  $1 \text{ mW/cm}^2$ . The oxygen pressure was 1 Torr, the substrate temperature range  $20\text{-}200^\circ\text{C}$ . The photon flux incidence both normal and parallel to surface was used. Before and after VUV-irradiation in oxygen substrate was transferred in the XPS-analytical module for the chemical state surface analysis.

After the photochemical cleaning the photo-CVD of  $\text{SiO}_2$  from  $\text{Si}_2\text{H}_6$  and  $\text{O}_2$  under Hg lamp radiation under normal photon flux incidence was carried out in the same photochemical technological module. The Hg lamp radiation power density on  $\lambda_1=185\text{nm}$  and  $\lambda_2=254 \text{ nm}$  was  $2 \text{ mW/cm}^2$  and  $20 \text{ mW/cm}^2$  respectively. The flow rate of mixture of  $\text{Si}_2\text{H}_6$  (1%) with He was  $38 \text{ cm}^3/\text{min}$  and oxygen flow rate was  $15 \text{ cm}^3/\text{min}$ , the total pressure was 2 Torr. The substrate temperature range  $20\text{-}200^\circ\text{C}$ .

Part of the deposited  $\text{SiO}_2$  films were VUV-post-irradiated by Hg lamp in oxygen during 40 min, the oxygen pressure was 5 Torr, the substrate temperature  $200^\circ\text{C}$ .

The obtained  $\text{SiO}_2$  films were studied by ellipsometry ( $\lambda=633 \text{ nm}$ ), Fourier-transformation infrared (FT-IR) spectroscopy, Rutherford backscattering spectrometry (RBS). The electrical properties were investigated by C-V measurements, I-V measurements and deep level transient spectroscopy (DLTS).

### 3. RESULTS AND DISCUSSIONS

#### 3.1. Photochemical cleaning of silicon substrate

An XPS analysis of silicon substrate treated in 1% HF aqueous solution showed the absence of native oxide and the presence of the



carbon contaminants with C-H bonds on the silicon surface. The ratio of the C1s peak area to Si2p peaks area  $A_{C1s}/A_{Si2p}$  characterizing the amount of carbon on the analyzed surface was equal 0,6. The VUV-irradiation of the silicon surface at room temperature under normal incidence of photon flux in oxygen resulted in the decrease of C1s peak. The rate of carbon removal in this conditions can be evaluated from the dependence of  $A_{C1s}/A_{Si2p}$  on the irradiation duration (Fig.2)

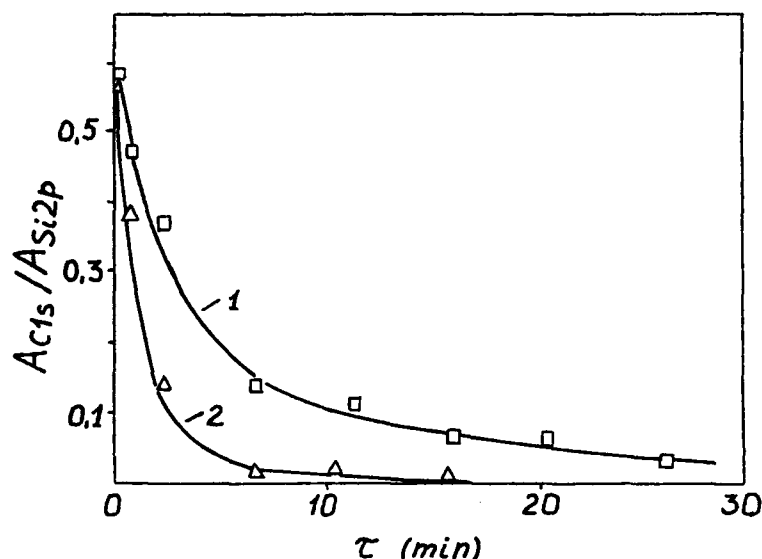


Fig.2.  $A_{C1s}/A_{Si2p}$  plots versus irradiation duration  $\tau$  measured by XPS from silicon surface VUV-irradiated in  $O_2$  (normal photon flux incidence) at  $T_s = 20^\circ\text{C}$  (curve 1) and at  $T_s = 200^\circ\text{C}$  (curve 2).

It was found that the effectiveness of photochemical carbon contaminants removal depended on the substrate temperature. Really, the decrease of  $A_{C1s}/A_{Si2p}$  in dependence on the irradiation duration is more sharp in the case of heated ( $200^\circ\text{C}$ ) substrate (Fig. 2). It is worth mention here that according to XPS analysis the heating in  $O_2$  up to  $200^\circ\text{C}$  without VUV-irradiation did not induce the carbon contaminants removal.

The dependence of the photochemical silicon substrate cleaning effectiveness on the direction of the photon flux incidence was investigated too. In Fig.3. the C1s XPS spectra measured from silicon

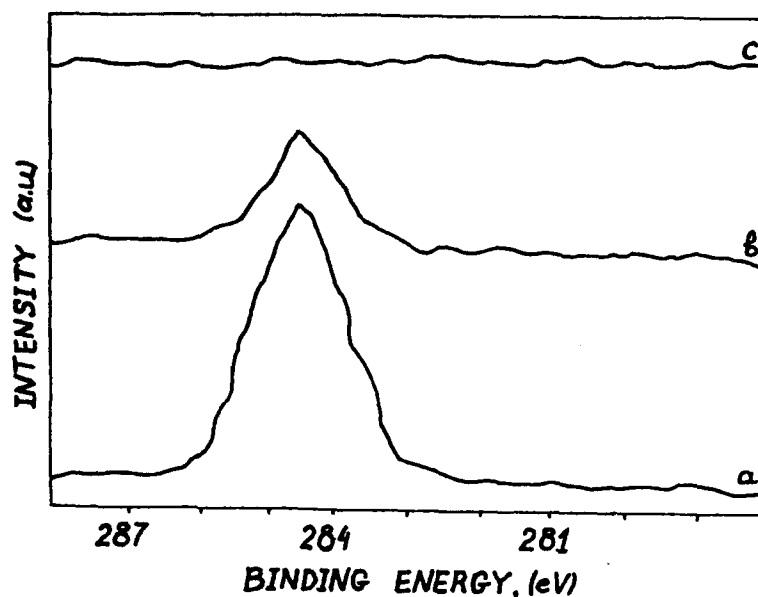


Fig.3. C1s XPS spectra measured from silicon surface: initial surface (a), after VUV-irradiation in  $O_2$  ( $\tau=15$  min,  $T=200^\circ C$ ) under parallel (b) and normal photon flux (c) incidence

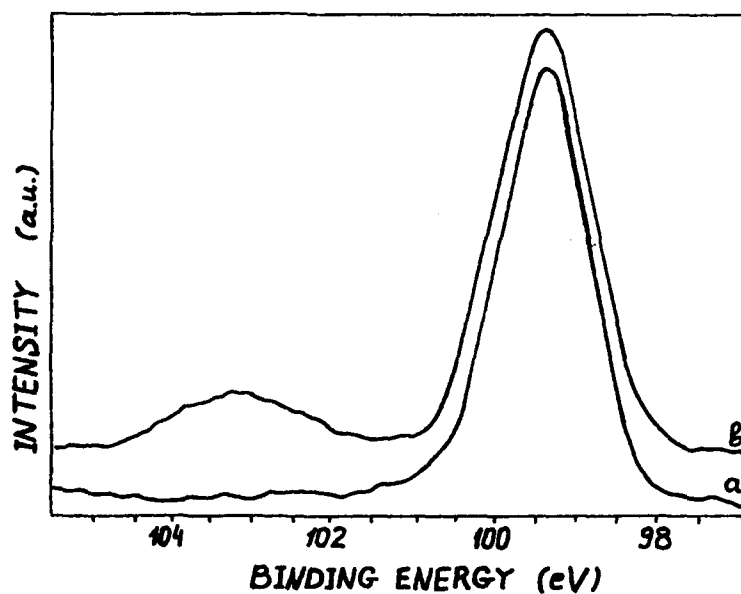


Fig.4. Si2p XPS spectra: a - silicon surface treated in 1% HF water solution; b - after VUV-irradiation in  $O_2$  ( $\tau=15$  min,  $T_s=200^\circ C$ , normal incidence of photon flux)

surface before (a) and after VUV-irradiation in  $O_2$  at  $T_s = 200^\circ C$  during 15 min under parallel (b) and normal (c) photon flux incidence. The absence of C1s XPS-signal in the case of normal photon flux incidence indicate the importance of photon-induced surface reactions for the effective removal of carbon contaminants.

Thus, the experiments on photochemical cleaning showed that VUV-irradiation of silicon surface in  $O_2$  at substrate temperature  $T_s = 200^\circ C$  under the normal incidence of photon flux allowed to remove the carbon contaminants to the value less than XPS analysis sensitivity ( $\sim 0.1$  at.%).

A slight photon induced oxidation of silicon was observed during the photochemical carbon contaminants removal. According to analysis of Si2p XPS spectrum (Fig. 4) the photochemical treatment resulted in the  $SiO_2$  formation up to depth of  $\sim 2$  monolayers.

### 3.2. Photo-CVD of $SiO_2$

It was found the VUV-radiation extensively influenced on the  $SiO_2$  CVD process from  $Si_2H_6$  and  $O_2$ . Thus, the film deposition rate is 2 nm/min at  $T_s = 20^\circ C$  under the VUV-irradiation, while without VUV-irradiation deposition was not observed at this temperature. At  $T_s = 200^\circ C$  the deposition rate was of 7 nm/min under VUV-irradiation, and one was of 3 nm/min without VUV-irradiation.

The FT-IR spectrometry analysis of the photo-CVD films with the thickness of 150 nm showed that their chemical composition depends on the substrate temperature during deposition. Thus, the FT-IR spectrum of the film formed by photo-CVD at  $T_s = 20^\circ C$  in addition to the absorption peaks at  $1060\text{ cm}^{-1}$  and  $810\text{ cm}^{-1}$  corresponding to Si-O bonding contains the absorption peaks at  $880\text{ cm}^{-1}$ ,  $2250\text{ cm}^{-1}$  corresponding to Si-H bonding, the absorption peak at  $950\text{ cm}^{-1}$  corresponding to Si-OH bonding and the absorption peak in the region of  $3500\text{ cm}^{-1}$  (Si-OH, H-OH bonding)<sup>6,7</sup> (Fig. 5a). The ratio of the Si-H absorption peak ( $880\text{ cm}^{-1}$ ) area to one of the Si-O absorption peak ( $1060\text{ cm}^{-1}$ )  $A_{Si-H}/A_{Si-O} = 0,22$ .

The increase of the substrate temperature during the photo-CVD

up to  $T_s = 200^\circ\text{C}$  results in the considerable decrease of the Si-H, Si-OH, H-OH bonds (Fig. 5b) and improvement the properties of  $\text{SiO}_2$  films. Really, in this case the ratio  $A_{\text{Si-H}}/A_{\text{Si-O}} = 0,1$ . It was found too that the VUV-irradiation allows to decrease noticeably the amount of Si-H bonds in the films in comparing with films deposited without VUV-irradiation at the same temperature.

The RBS analysis of the films formed by the photo-CVD at  $T_s = 200^\circ\text{C}$  showed that the ratio of the oxygen atoms number to the silicon ones  $N_{\text{O}}/N_{\text{Si}} = 2 \pm 0,02$  which indicates the high stoichiometry of the formed  $\text{SiO}_2$  films. In addition to this the RBS analysis combined with the profilometer thickness measurements allowed to measure the  $\text{SiO}_2$  film density which was of  $2,1 \text{ g/cm}^3$ , which is close to one of  $\text{SiO}_2$  formed by the high temperature silicon oxidation. According to the ellipsometry analysis the refraction index  $n$  of the photo-CVD  $\text{SiO}_2$  films was 1,455.

It is worth mention that the pre-deposition VUV-radiation induced removal of carbon contaminants from the substrate surface results in the enhance of the photo-CVD  $\text{SiO}_2$  film adhesion to the substrate. Really, in contrast with the  $\text{SiO}_2$  films deposited on the photon-induced precleaned surface, the films formed without photon-stimulated cleaning of substrate reveal the tendency of spontaneous peeling off.

### 3.3. Low temperature VUV-radiation-stimulated post treatment of deposited $\text{SiO}_2$

Just after the photo-CVD at  $T_s = 200^\circ\text{C}$  in the same reaction chamber the experiments on the post treatment of the deposited  $\text{SiO}_2$  films both under the VUV-irradiation and without of one were carried out. Taking into account that VUV-irradiation of oxygen results in the formation of active oxygen species and ozone which can induce a termination of Si-H bonds in the deposited films leading to formation of silicon dioxide with more perfect chemical composition in both cases the treatment was carried out in oxygen. The FT-IR spectroscopy analysis showed that the post treatment without VUV-irradiation did

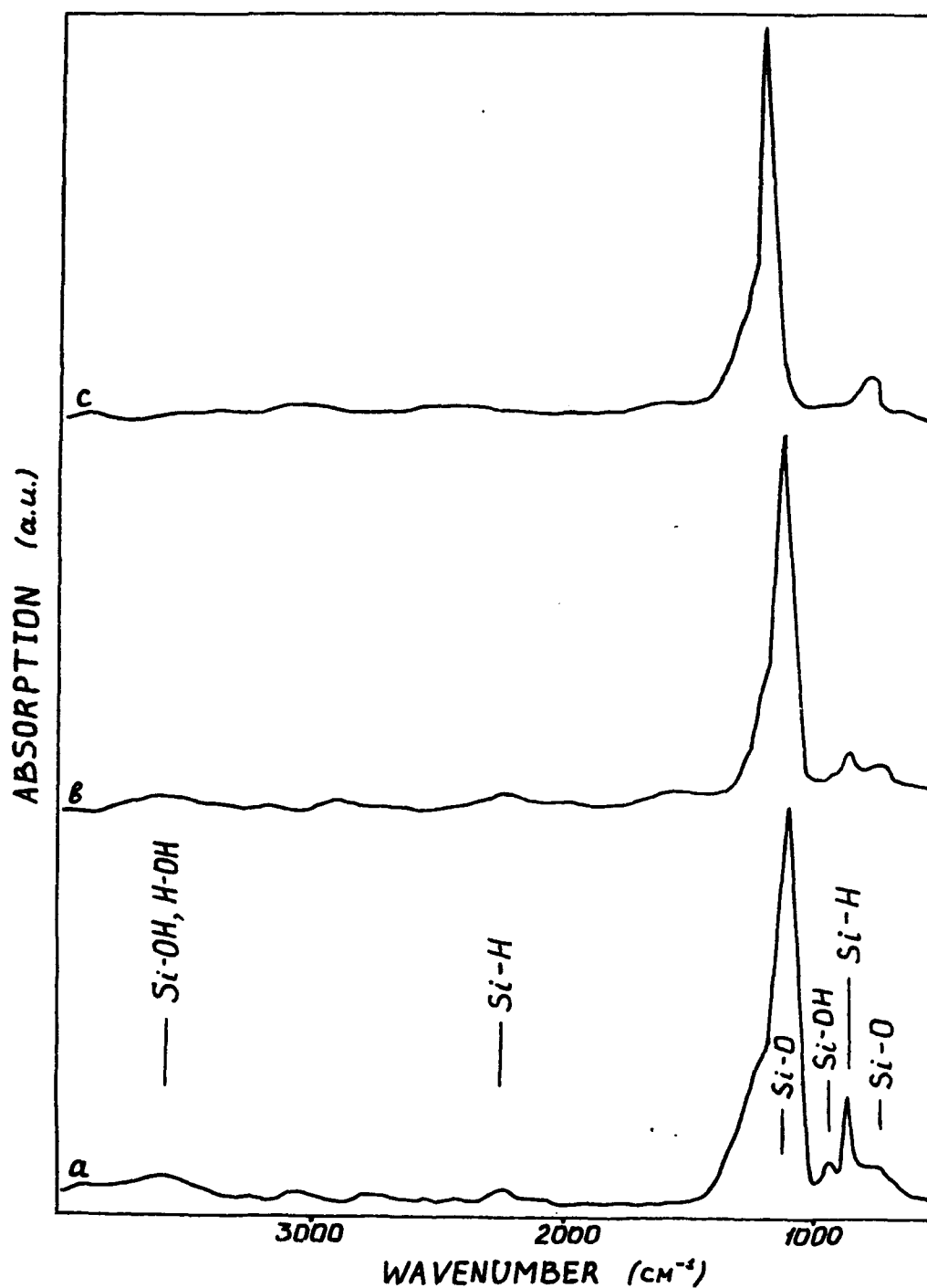


Fig.5. FT-IR absorption spectra for SiO<sub>2</sub> films formed by photo-CVD at T<sub>s</sub>=20°C (a), at T<sub>s</sub>=200°C before (b) and after VUV-radiation stimulated post treatment in O<sub>2</sub> at T<sub>s</sub>=200°C during 40 min (c).

not induce noticeable changes in the FT-IR spectra of  $\text{SiO}_2$  films. In contrast with this the post treatment under the VUV-irradiation resulted in the practical disappearing of the absorption peaks corresponding to Si-H, Si-OH, H-OH bonds in the FT-IR spectra of the  $\text{SiO}_2$  films (Fig. 5c).

According to<sup>6,7</sup> the decrease of Si-H, Si-OH bonds in the  $\text{SiO}_2$  films improves their electrical properties. Really, the C-V measurements of the photon-assisted annealed  $\text{SiO}_2$  films (Fig. 6) indicated on the considerable decrease of the oxide charge density up to the value of  $\leq 1 \cdot 10^{11} \text{ cm}^{-2}$ .

The deep level transient spectroscopy measurements allowed to obtain information about the interface state density (Fig. 7), thus minimum interface state density after the VUV-irradiation post-treatment was  $\sim 5 \cdot 10^{10} \text{ eV}^{-1} \cdot \text{cm}^{-2}$ . It was found too that the breakdown voltage of the post-treated  $\text{SiO}_2$  films was  $(5 \div 10) \cdot 10^6 \text{ V/cm}$ .

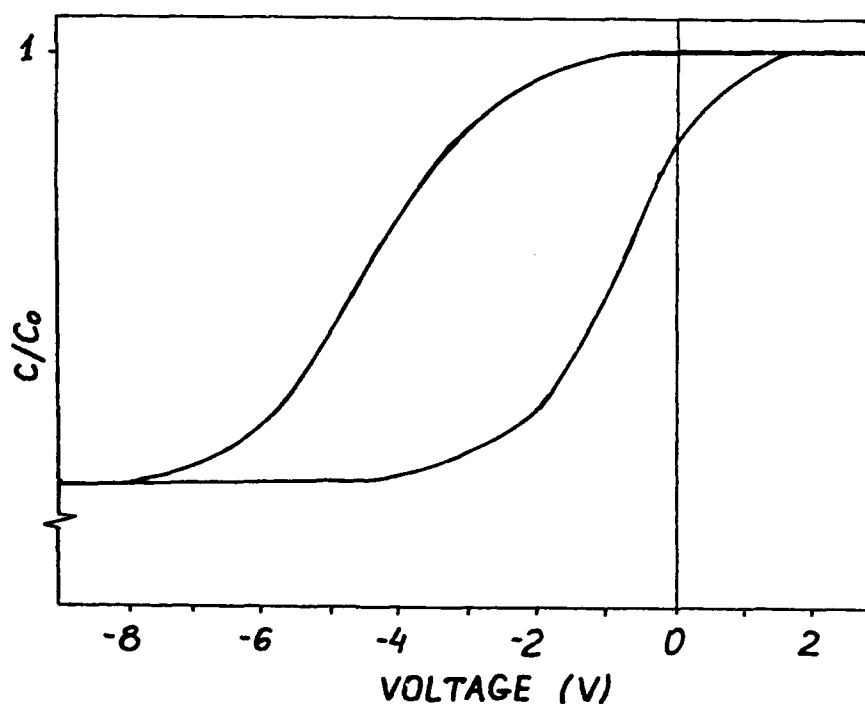


Fig. 6. Capacitance versus voltage curves of Si- $\text{SiO}_2$ -Al capacitor measured for as deposited  $\text{SiO}_2$  films (curve 1) and for the VUV-radiation-stimulated post treated  $\text{SiO}_2$  film (curve 2).

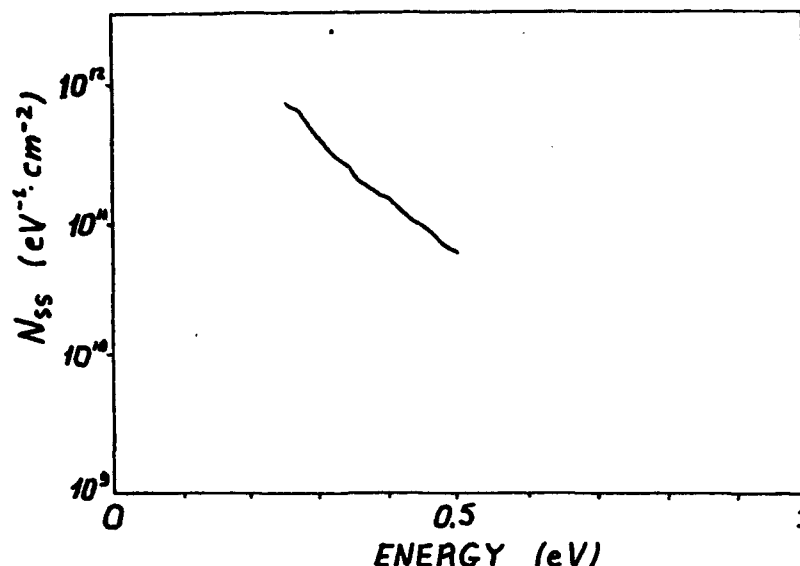


Fig.7. Interface-state densities  $N_{ss}$  of the MOS diodes using  $\text{SiO}_2$  film deposited at  $T_s = 200^\circ\text{C}$  and VUV-radiation post-treated.

#### 4. CONCLUSIONS

- VUV-radiation induced carbon contaminants removal in oxygen atmosphere from silicon surface proceeds more effectively at  $T_s = 200^\circ\text{C}$  and normal photon flux incidence. In this conditions of cleaning carbon contaminants are not detected by *in situ* XPS analysis
- VUV-radiation induced post-treatment of  $\text{SiO}_2$  allows to decrease the amount of Si-H, Si-OH bonds and decrease fixed charge density in the films
- integration of VUV-radiation induced processes for silicon substrate cleaning, silicon dioxide deposition and post-treatment resulted in the dielectric formation with the next properties: stoichiometry -  $\text{SiO}_{2 \pm 0.02}$ , density -  $2.1 \text{ g/cm}^3$ , refraction coefficient - 1.455, electrical breakdown field -  $5 \pm 10 \text{ MV} \cdot \text{cm}^{-1}$ , fixed charge density -  $1 \cdot 10^{11} \text{ cm}^{-2}$ , minimum interface states density -  $5 \cdot 10^{10} \text{ eV}^{-1} \text{cm}^{-2}$ .

## REFERENCES

1. D. Rieger and F. Bachmann, "ArF laser induced CVD of  $\text{SiO}_2$  films: a search for the best suitable precursors," Appl. Surf. Sci. Vol. 54, pp. 99-107, 1992.
2. T. Inushima, N. Hirose, K. Urata, K. Ito and S. Yamazaki, "Film growth mechanism of photo-chemical vapor deposition," Appl. Phys., Vol. A 47, pp. 229-236, 1988.
3. M. Petijen, N. Proust, J.-F. Chapeaublanc, " $\text{SiO}_2$  deposition by direct photolysis at 185 nm of  $\text{N}_2\text{O}$  and  $\text{SiH}_4$ ," Appl. Surf. Sci., Vol. 46, pp. 189-194, 1990.
4. P. K. Boyer, G. A. Roche, W. H. Ritchie and C. J. Collins, "Laser induced chemical vapor deposition of  $\text{SiO}_2$ ," Appl. Phys. Lett., Vol. 40, pp. 716-718, 1982.
5. J. Shirafuji, S. Miyoshi and H. Aoki, "laser-induced chemical vapor deposition and characterization of amorphous silicon oxide films," Thin Solid Films, Vol. 157 pp. 105-115, 1988
6. Y. Toyoda, K. Inoue, M. Okuyama and Y. Hamakawa, "Preparation of  $\text{SiO}_2$  film by photo-induced chemical vapor deposition using a deuterium lamp and its annealing effect," Jpn. J. Appl. Phys., Vol. 26, pp. 835-840, June 1987.
7. K. Inoue, M. Michimori, M. Okuyama and Y. Hamakawa, "Low temperature growth of  $\text{SiO}_2$  thin films by double-excitation photo-CVD," Jpn. J. Appl. Phys., Vol. 26 pp. 805-811, June 1987.
8. K. Inoue, M. Nakamura, M. Okuyama and Y. Hamakawa, "Reduction of interface-state density by F treatment in a metal-oxide-semiconductor diode prepared from a photochemical vapor deposited  $\text{SiO}_2$  film," Appl. Phys. Lett., Vol. 55 pp. 2402-2404, 1989
9. C. Debauche, C. Licoppe, C. Meriadec, F. Sartoris and J. Freyenstein, "UV annealing of low temperature photodeposited  $\text{SiO}_2$  films with a new powerful lamp source," Appl. Surf. Sci., Vol. 54, pp. 435-439, 1992.



## Laser welding in optoelectronics

Doc. Ing. DUNOVSKÝ Jiří, CSc. \*  
RNDr. KUCHAR Elemer, RNDr. AUBRECHT Ivo, CSc. \*\*  
Doc. Ing. HÜTTEL Ivan, DrSc. \*\*\*

\* Faculty of Mechanical Engineering of the Czech Technical University of Prague,  
Technická 4, Praha 6, 160 00, Czech Republic

\*\* Institute of Radio Engineering and Electronics Academy of Sciences of the Czech Republic,  
Chaberská 57, Praha 8, 180 00, Czech Republic

\*\*\* Prague Institute of Chemical Technology  
Technická 1, Praha 6, 160 00, Czech Republic

### ABSTRACT

The high-power laser beam welding is a progressive technology which can be employed in optoelectronics and integrated optics. Its advantageous feature is the possibility to achieve a long-term stable and high mechanically reliable coupling between a semiconductor injection laser and an optical waveguide.

Two proposed and investigated schemes of stable and reliable couplings of semiconductor laser to fibre-optic waveguides are described. Both schemes employ high-power impulse Nd-YAG laser beam for the fixation of the fibre-optic waveguide to the laser diode heat sink. Specially designed mechanical components are used for this purpose.

### 2. INTRODUCTION

There are some areas of modern optics, such as optoelectronics and integrated optics, where mastering the technology of coupling between a semiconductor injection laser and an optical waveguide plays the fundamental role. What is required in particular is a high efficiency of the optical energy transfer from the laser into the waveguide and long-lasting mechanical stability of the coupling.

Till now, many coupling schemes, differing in efficiency, stability and cost, have been designed [1-6]. The coupling efficiency can be considerably increased by means of a convenient optical system placed between the laser and the waveguide, including a microlens formed on the waveguide front surface, or by covering this surface with an antireflection layer. The stability can be ensured by suitable fixing the waveguide input to the semiconductor laser, using fixation technologies based on gluing, soldering and high-power laser beam welding. It is well known that the former two methods can only rarely result in a long-lasting waveguide fixation in the set-up position for the maximum coupling efficiency due to glue volume changes or irregularities of the solder solidification process. Moreover, soldering may damage or destroy the semiconductor laser. The latter method, the laser welding, does not require any additional fixing material as the gluing or soldering does, and the heat build-up during the welding is very local and very short in time. As a consequence, the obtained weld is of long-lasting mechanical stability and the danger of semiconductor laser damage is almost avoided.

Two proposed and investigated schemes of stable and reliable couplings of a semiconductor laser to a fibre-optic waveguide are described in this paper. High-power impulse Nd-YAG laser beam is employed for the fixation of the fibre-optic waveguide to the semiconductor laser diode heat sink in these schemes. To set up and fix the location of the fibre-optic waveguide which is optimal from the point of view of the coupling efficiency, specially designed mechanical components are used.

### 3. SCHEMES OF COUPLING

The semiconductor laser with the fibre-optic waveguide fixed to its heat sink is placed in a special module containing a Peltier cell, a diode monitoring the laser power, and necessary control and regulation electronics. The following two schemes differ in construction and in that whether the fixation is made outside the module (the first scheme) or inside the module (the second scheme).

#### 3.1. CTLCHS fixation scheme

The author of this scheme is J. Hüttel with whose kind permission some construction and technological details are presented here. The name of the scheme is derived from the initial characters of its components.

The components of the scheme are: a steel capillary tube of a length of 10 mm and of an inside diameter of 0.2 mm, a circular steel lamella of a diameter of 3.5 mm and of a thickness of 0.1 mm, a steel cylinder of a diameter of 4 mm and of a height of 1.5 mm, and a copper heat sink with an opening (through its thickness) for that cylinder. The fixation principle and the technology are as follows: First of all, the lamella is welded on to the capillary tube from the side of the lamella, and a part of the fibre-optic waveguide to be fixed is inserted into the tube where it is fastened with a glue (the fibre diameter fits the inside capillary tube diameter). The lamella with the tube is laid upon the cylinder which is placed in that heat sink opening (the cylinder lies on a small spring but only for the purpose of location adjusting). After the optimal coupling efficiency is achieved the fixation welds the lamella - the cylinder, the cylinder - the heat sink are carried out.

For laser welding, a special welding machine based on Nd-YAG laser with an optomechanical aiming system was used. This welding aggregate was developed at the Institute of Radio Engineering and Electronics Acad. Sci. CR, and it is drawn schematically in Fig.1. The Nd-YAG laser generates light pulses at the wavelength of 1064 nm with the beam divergence (full angle) of approx. 4 mrad. The pulse duration is 3.5, 4.5 or 5 ms (optional) and the maximum energy is 8J. The generated beam is focused and aimed at the target by means of the aiming system. The location of the welds can be chosen within the volume of approx. 15x15x15 mm<sup>3</sup>. Accurate aiming of the beam is ensured either by a visual control system (not shown in Fig.1) or by the semiconductor laser TOSHIBA 9201(s),  $\lambda = 660$  nm.

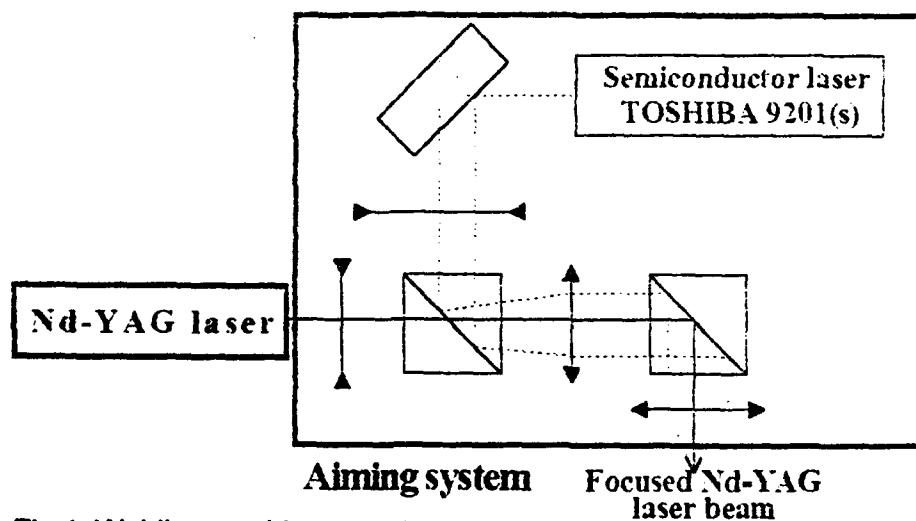


Fig.1: Welding machine based on Nd-YAG laser with an optomechanical aiming system.

### 3.2. DKX fixation scheme

This scheme was developed at the Faculty of Mechanical Engineering of the Czech Technical University.

Fibre-optic waveguide is indium coated and soldered into the steel capillary (1) ( see fig. 2a ,2b ). The capillary (1) together with the optic waveguide is moved in x, y, z directions until the best position is attained ( i.e. the position with maximum coupled power ). The carrier (2) is shifted in the x direction on the stirrup (3) surface . As soon as there is a contact between the capillary and carrier, the spot welds W1 and W2 are made by laser LAX-5 (  $\lambda = 1064 \text{ nm}$  , pulse energy = 1-8 J , pulse duration 1-6 ms ). Then the carrier (2) is welded by this laser to the stirrup (3) ( spot welds W3,W4,W5. and W6 ). Technological conditions of the welding are listed in table 1.

All welds are made in vertical direction and so it is possible to fix the fiber-optic waveguide inside the optoelectronic device module. The carrier is cut out from a steel lamella of a thickness of 0.1 mm by means of the laser OPTRONIC 757 DMX (  $\lambda = 1064 \text{ nm}$  , average power = 40 W , peak power = 40 kW, repetition frequency = 0.01 - 50 kHz ).

Table 1 : Technological conditions of the welding. All spot welds are made by laser LAX-5.

| Spot weld | Power supply<br>battery voltage<br>[kV] | Pulse duration<br>[ms] | Iris diaphragm<br>number | Distance<br>focus-weld<br>position <sup>1</sup> |
|-----------|---|------------------------|--------------------------|---|
| W1,W2     | 1.6                                     | 4                      | 0.9                      | -1.2  |
| W3-W6     | 1.65                                    | 4                      | 1                        | -4  |

<sup>1</sup> It is negative if the weld is above the focus, positive if the focus is above weld.

#### References

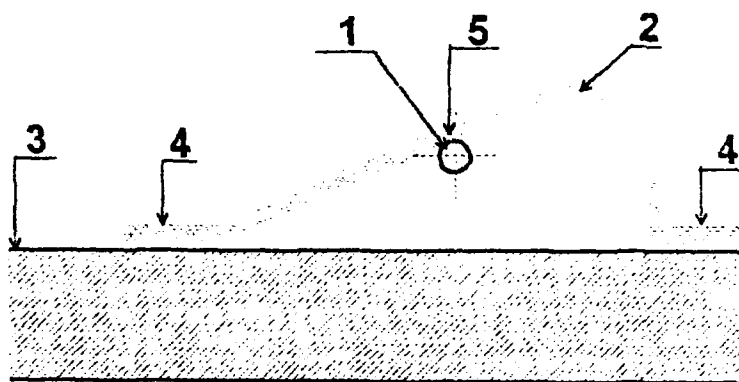


Fig.2a : DKX fixation scheme.

1.Capillar. 2.Carrier. 3.Stirrup. 4.Spot welds W3,W4,W5 and W6. 5.Spot welds W1 and W2.

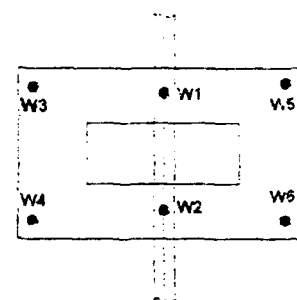


Fig.2b :DKX fixation scheme -plan. W1-W6 spot welds

#### 4. REFERENCES.

- [1] Weidel , E. : Light coupling a junction laser into a monomode fibre with a glass cylindrical lens on the fibre end. Optics Commun. , Vol. 12, No. 1 , September 1974
- [2] Kawano , K. : Combination lens method for coupling a laser diode to a single -mode fibre. Appl. Optics , Vol. 24 , No. 7 , April 1985
- [3] Kawano , K. : Coupling characteristics of lens systems for laser diode modules using single-mode fibre. Appl. Optics , Vol. 25 , No. 15 , August 1986
- [4] Karstensen , H. : Laser diode to single-mode fibre coupling with ball lenses. J. Opt. Commun. , Vol. 9 , No. 2 , 1988
- [5] Karstensen , H. : High efficiency two lens laser diode to single-mode fibre coupler with a silicon plano-convex lens .J. Lightwave Technol. , Vol. 7 , No. 2 , February 1989
- [6] Shiraisi , K. : New scheme of coupling from laser diodes to single-mode fibres : a beam expanding fibre a hemispherical end. Appl. Optics , Vol. 29 , No. 24 , August 1990
- [7] Dunovský, J. - kol, : Vývoj nových metod svařování , dělení a defektoskopie pro elektroniku a optoelektroniku . Výzkumná zpráva č. 2116 , ČVUT - FS, Praha 1991
- [8] Dunovský, J. - kol, : Vývoj technologie výroby přesných detailů laserem. Výzkumná zpráva č. HS 216 487 ČVUT - FS , Praha 1987

# Numerical investigation of laser slip-flow gas mixture separation

A.S. Lagutchev, Yu.N. Petrov.

Heterophase Optical Processes Lab., Institute of General Physics, 117942, Moscow, Russia.

## ABSTRACT

Simple single-particle iterative procedure is proposed to simulate molecular flows in capillaries. Intermolecular collisions are taken into account. Based on the computer simulation the mechanism of laser action on slip flows in capillaries is described. Some perspectives of laser gas-mixture separation in capillaries are discussed.

## 1. INTRODUCTION

Slip flow in capillaries takes place when the molecular mean free path and the capillary diameter are of the same order. There are no simple analytical formulae describing the flow of that kind, especially in the case of a gas-mixture flow. On the other hand, slip flows in capillaries were found recently to be of interest for the laser-assisted gas-mixture separation<sup>1</sup>. Absorbing molecules in the gas mixture could be selectively excited by laser radiation. If the gas is sufficiently rarefied (i.e. intermolecular collisions frequency and molecular-wall collisions frequency are close to each other), selective excitation of the absorbing component can lead to its selective heating. The temperatures and capillary gas conductivities of mixture components become different. This results in steady enrichment of the flowing mixture by one component. Such situation can occur only in the slip flow. Separation is impossible in the viscous flow due to the effective momentum exchange in intermolecular collisions. Steady free-molecular flow is insensitive to the temperature changes. In order to optimize separation in the slip flow one should develop suitable analytical or computational model.

## 2. METHOD

We failed to find simple analytical description method for the slip flow of gas mixtures through long tubes. Phenomenological formulae for tube gas conductivity in the slip-flow region contain coefficients which are unique for the given gas. In the case of a gas mixture this approach becomes perfectly inconvenient. Many problems disappear if the direct computer simulation of molecular motion in the tube is used. By direct simulation we assume separate molecules trajectories calculation (one by one or as a group) with subsequent averaging procedure which gives macroscopic parameters of the flow. To perform such a simulation one needs to know only the molecules velocity distribution near the tube ends, velocity distribution of the molecules, desorbing from the tube walls and (optionally) molecule-molecule scattering characteristics. Nothing prevents modeling of binary or more complex mixtures flows. Many specific features of molecule desorption process, e.g. angular distribution, momentum and energy accommodation, etc. can be easily taken into account.

Velocity distribution in the volumes near the tube ends is assumed to be maxwellian. This is true in the case of a "small leak", when the majority of the entering molecules return back, thus the distortion of the velocity distribution in the volume is negligible. Such situation is typical for a slip flow. Angular distribution of the desorbing molecules could be described by the Knudsen cosine law as the first approach. Scattering angles and velocities after the intermolecular collision are given by formulae of classical mechanics for the given type of the interaction potential.

The simplest case to apply the approach just described would be the simulation of a steady free-molecular flow through the tube into vacuum. Since no intermolecular collisions occur one can introduce separate molecules with random velocity vectors consequently from the tube entrance. Random trajectory is calculated until the particular molecule either exits from the tube end into vacuum or returns back to the initial volume. Being repeated for many times this algorithm gives the molecular transmission probability of the tube,  $\nu$ , which is proportional to the tube gas conductivity.

$$\nu = \frac{N}{N_0} \quad (1)$$

Here  $N_0$  is the total number of introduced molecules,  $N$  is the number of molecules, that successfully passed the tube. Such a simulation was performed in early 60-ties (e.g.<sup>2</sup>). It should be pointed out that in the case of a steady free-molecular flow the tube gas conductivity is simply a geometric factor being independent upon gas and walls temperatures provided the cosine law of desorption is still applicable.

The situation appears to be more difficult if one comes to the region of a slip flow. Intermolecular collisions should be taken into account. This problem could be solved in two ways. The first one assumes simultaneous simulation of many molecules moving, adsorbing, desorbing, colliding, etc. inside the tube. Calculation difficulties of this method grow very fast if the number of molecules increases. One should possess a supercomputer to obtain any valuable results using this method. Fortunately enough there is the other way, which seems to be proposed first in<sup>3</sup>. The simulation of a steady slip flow could be performed by comparatively simple iterative procedure. Each step of such iteration resembles the process of transmission probability calculation for collisionless conditions. One monitors only a single molecule random flight through the tube. In addition random intermolecular collisions are simulated. Collision probability is proportional to the molecular concentration inside the tube. This concentration is calculated during each iteration step using molecular velocities data. Concentration profile, obtained during the  $n$ -th step is used to calculate collision probability at the  $(n+1)$ -th step. Numerical experiments show that the described iteration usually converges, though strict mathematical evidence of this fact is unknown for us. One can say only that if the numerical iterative model properly reflects the real process this model should be converging.

The steady slip flow in tubes could be simulated provided one can calculate the velocities after the random intermolecular collision. The strict calculation of the random angle and velocity according to the scattering theory is difficult. Suitable formulae contain complex trigonometric functions combinations. This factor slows down the calculation dramatically. Fortunately we found out that for the transmission probability calculation one can assume the spatial distribution of the scattering angle to be uniform without substantial loss of the accuracy. Moreover, it turned out that molecular velocities could be set constant and equal to the average molecular speed at the given temperature. Thus, the procedure was strongly simplified.

Molecular movement in the tube with the flow is not completely random. Mean molecular velocity is nonzero. For adequate description of the gas flow in a tube with collisions one should take into account the process of regular momentum transfer in the flow direction. This transfer is responsible for the linear dependence of the tube gas conductivity from input pressure in the viscous flow region. This is a consequence of the Poiseuille formula for the viscous flow<sup>4</sup> (viscosity is the process of momentum transfer by definition). If collisions disappear (free-molecular flow), regular momentum transfer vanishes and tube gas conductivity becomes independent upon the input pressure.

We found out, that the regular momentum transfer could be comparatively easy taken into account using the described iteration process. We propose to divide all the molecules in the tube into two groups: randomly moving (RM) and directly moving (DM) ones. First ones never pass the tube, second ones are doomed to pass it. RM molecules mean velocity equals to zero. DM molecules mean velocity is constant along the tube and can be calculated using average lifetime of the DM molecule in the tube. Collision of the monitored molecule with RM molecule results in velocity which spatial distribution is uniform. Collision with the DM molecule results in uniformly distributed velocity plus the additional regular component. This component is assumed to be equal to the DM molecules velocity. The probability of collision with either RM or DM molecule is proportional to the ratio of their concentrations. DM molecules concentration equals to the total concentration near the tube entrance multiplied by the transmission probability  $\nu$  and is assumed to be constant along the tube.

Described method seems to be rather primitive but let us emphasize that our main goal while developing all this calculation technique was not the accurate calculation of the tube gas conductivity, but rather its relative variation

under laser action. Such information is necessary to optimize the action on the slip flow as well as the separation factor. The algorithm should be simple and efficient to maintain multiple parameters optimization in realistic time intervals.

Let us show that the proposed algorithm works at least at the slip-flow region.

### 3. RESULTS

To test the algorithm we used the "Knudsen minimum effect" which is well known from the classical gas kinetic theory. When the mean pressure in the tube rises from almost zero the gas flow passes through the three consecutive stages: free-molecular, slip-flow and the viscous one. Accordingly, transmission probability  $\nu$  is constant at the free-molecular stage, exhibits minimum at the slip-flow stage and grows linearly with pressure at the viscous stage. Fig. 1 demonstrates transmission probability vs. pressure in the tube for three model situations. Dependence No I corresponds to the case when intermolecular collisions are completely suppressed (by assuming molecular cross section  $\sigma=0$ ) and demonstrates the level of  $\nu$  for collisionless flow. No II reflects the situation when all molecules are assumed to collide in a completely random manner, i.e. regular momentum transfer is not taken into account. In this case the transmission probability  $\nu$  decreases sharply with pressure. The total flow being the product of the incident flow and  $\nu$  begins to decrease also, which is obviously unrealistic result. Finally, No III demonstrates the effect of the regular momentum transfer. This curve looks very much like those, experimentally obtained by Knudsen in 1905<sup>5</sup>.

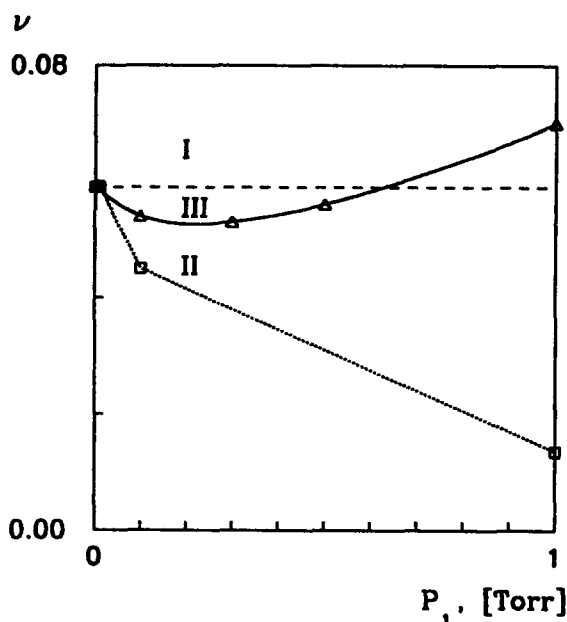


Fig.1. Molecular transmission probability  $\nu$  vs. pressure at the capillary entrance  $P_1$ . I - collisions are suppressed (collision cross section  $\sigma=0$ ), II - collisions occur without momentum transfer, III - regular momentum transfer is taken into account. The latter case demonstrates "Knudsen minimum".

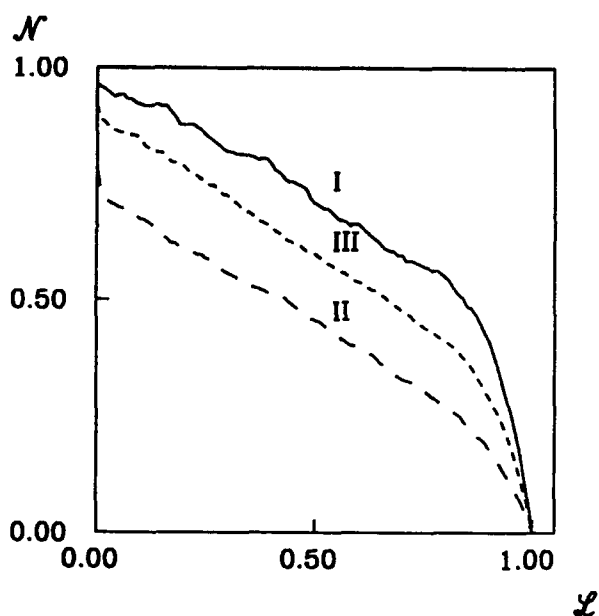


Fig.2. Normalized gas density  $N$  in the capillary vs. dimensionless longitudinal coordinate  $\ell$ . Pressure at the entrance - 1 Torr. I - initial profile (room temperature), II - density profile under laser heating, III - density profile after heating capillary walls up to 500°K.

The mechanism of laser heating is assumed to be as follows: absorbing molecule is excited during its flight from one wall to the other; deexcitation takes place mostly at the wall resulting in the desorption of the molecule with excessive translational energy; excessive energy dissipates during intermolecular collisions. Calculation results, presented here were obtained for the  $SF_6$  gas under cw  $CO_2$  laser irradiation for the tube of 0.5 mm in diameter, 10 mm

length. As it is shown on Fig. 2, gas density inside the capillary decreases and its dependence upon relative length becomes more linear either under walls or laser heating. The flow seems to become "more collisionless" and transmission probability is decreased by about 30% and 20% consequently for walls heating and laser heating. This result is in the good agreement with our former experiments<sup>1</sup>.

#### 4. CONCLUSION

Next step in the usage of the described method will be the optimization of laser action on the absorbing gas flow by such parameters as the tube dimensions, walls temperature, input and output pressure, etc. We plan to report the results of this optimization in the nearest future. More complex problem will be the simulation of binary mixture flow through a tube under selective laser action and separation coefficient optimization but we don't expect any principle difficulties on this way. The proposed algorithm can be used in a variety of the problems connected with the slip flow. It becomes the method of choice especially in the presence of temperature or concentration gradients, flows with positive or negative sources, e.g. slip flows in hollow fibers.

#### 5. REFERENCES

1. A.S. Lagutchev, A.N. Orlov, Yu.N. Petrov, R. Alexandrescu, I. Morjan, "Selective Laser Action on Gas-Mixtures Flows through Capillaries", *Proceedings of the International Symposium on Gas Separation Technology, Process Technology Proceedings*, Elsevier, Amsterdam, Vol.8, pp. 57-58, 1990.
2. D.H. Davis, "Monte Carlo calculation of molecular flow rates through a cylindrical elbow and pipes of other shapes", *J. Appl. Phys.*, Vol.31, p. 1169, 1960.
3. J.O. Ballance, W.K. Roberts, D.W. Tarbell, "A study of cryopump configurations in free-molecular-flow regions", in: *Advances in Cryogenic Engineering*, Vol.8, Plenum Press, New York, p.46, 1963.
4. E.H. Kennard, "Kinetic theory of gases", McGraw-Hill, N.Y., 1938.
5. M. Knudsen, "Die Gesetze der Molecularströmung und inneren Reibungsströmung der Gase durch Röhren", *Annalen der Physik*, Vol. 28, pp. 75-130, 1909.



## Resonant electromagnetic fields effects on dimers

Maksimov V.V.<sup>\*</sup>, Orlov A.N.<sup>\*\*</sup>, and Prokhorov A.M.<sup>\*\*</sup>

<sup>\*</sup> N.S. Kurnakov Institute of General and Inorganic Chemistry, RAS,  
117907, Moscow, Leninskii Prospekt, 31, Russia

<sup>\*\*</sup> General Physics Institute, RAS,  
117942, Moscow, Vavilov St., 38, Russia

### ABSTRACT

The interaction changes between two molecules in dimer due to excitation presence are considered. The two levels approach is used. The changes in the dynamic and in the spectroscopy of such dimers are predicted.

In definite conditions, e.g. on a condensed body surface, alone molecules of substances can unite in dimers. Further we shall imply the surface dimers molecules will not differ one each other. Some substance molecules, e.g. formic acid, can cling in the dimer effectively in common conditions in gaseous phase. For any substance molecules the most effective dimers creating takes place during cooling in a gasdynamic jet.

Molecules unite in dimers due to London's forces and because of interaction between constant multipoles moments.

The questions about electromagnetic fields effects on associates consisting of several particles<sup>1,2</sup> to decompose them or to initiate their growth were put in works<sup>1,2</sup>.

In this work the question about the additional interaction between the dimer molecules due to excitation one of them is considered. If the dipole active transition is possible, then the quantum exchange is defined by the dipole-dipole interaction at least, in the opposite case the first interaction member is quadrupole-quadrupole one. In our approach the dimer molecules are regarded as two level systems. The consideration implies the times less than the time of the complete energy of excitation transfer in the rotational, translation movements energy or in photons one. Molecular constant multipoles are supposed not to be changed by the excitation. Further we shall consider prolong photon exchange only.

For a pair of identical molecules<sup>2</sup>, which are excited at a time  $t = 0$  with probabilities  $\alpha^2$  and  $\beta^2$  ( $\alpha^2 + \beta^2 = 1$ ), one can write

$$i\dot{\psi}_1 = V\psi_2 + i\alpha\delta(t), \quad i\dot{\psi}_2 = V\psi_1 + i\beta\delta(t), \quad (1)$$

where  $\psi_1$  and  $\psi_2$  are the wave functions characterizing the excitation

of the first and the second particles respectively,  $V$  is the matrix element of the interaction between two molecules,  $V$  is assumed not to be time-dependent,  $\delta(t)$  is Dirac's delta function.

The main difference of our approach here from the consideration<sup>3</sup> is in that the dimer has just existed, and at an initial time the quantum excitation presence probability on any molecule is arbitrary (but  $\alpha^2 + \beta^2 = 1$ ). During dimer interaction with the other particles in gas phase or on a surface (with phonons) the change of ratio between  $\alpha^2$  and  $\beta^2$  occurs in cases, when the interaction energy is comparable with  $V$ , as if the getting out of the phase of the quantum circulating took place for the excitation quantum. The getting out of the excitation quantum circulating phase due to interaction with phonons was considered previously.

The system of the equations (1) can be deduced derived of Schrodinger's equation for two 2-level interacting systems under two additional predictions: 1. excitation quantum energy should be larger than the matrix element of the interaction between two molecules  $V$ , in this case the use of Dirac's delta function is possible; 2. the matrix element of the interaction between two molecules  $V$  should be larger than the molecules interaction with the laser field  $V \gg \mu_0^1 E$ , where  $\mu_0^1$  is the matrix element of dipole moments of the molecule transition for the resonant mode,  $E$  is the electric intensity amplitude of the laser field. After perform a Fourier transformation with the system of equation (1) we obtain

$$\left. \begin{aligned} -\varepsilon \varphi_1 &= V \varphi_2 + \alpha i \\ -\varepsilon \varphi_2 &= V \varphi_1 + \beta i \end{aligned} \right\} \quad (2)$$

where

$$\varphi_j = \int_{-\infty}^{+\infty} \psi_j e^{-i\varepsilon t} dt, \quad j = 1, 2.$$

To derive the functions  $\psi_j$  it is necessary to perform the inverse Fourier transformation:

$$\psi_j = \frac{1}{2\pi} \int_{-\infty - i\delta}^{+\infty - i\delta} \varphi_j e^{i\varepsilon t} d\varepsilon, \quad (3)$$

where  $i\delta$  is a small imaginary component, (3) shifts the contour of integration slightly.

From (2) we obtain  $\varphi_1 = i \frac{(\beta V - \alpha \epsilon)}{\epsilon^2 - V^2}$ ,  $\varphi_2 = i \frac{(\alpha V - \beta \epsilon)}{\epsilon^2 - V^2}$ , (4)

Performing the inverse Fourier transformation we obtain

$$\left. \begin{aligned} \psi_1 &= \frac{(\alpha + \beta)e^{-iVt} + (\alpha - \beta)e^{iVt}}{2} \\ \psi_2 &= \frac{(\alpha + \beta)e^{-iVt} - (\alpha - \beta)e^{iVt}}{2} \end{aligned} \right\} \quad (5)$$

Performing the inverse Fourier transformation on the formulas indicated above, for  $\langle V \rangle$  we get

$$\langle V \rangle = \frac{1}{4\pi^2} \iint_{\epsilon \xi} (\varphi_1^*(\xi) \hat{V} \varphi_2(\epsilon)) e^{i(\epsilon - \xi)t} d\epsilon d\xi + \text{c.c.} \quad (6)$$

where the contour of integration over  $\xi$  is a mirror image relative to the real axis of the contour integration over  $\epsilon$ . Performing the corresponding integration, we obtain

$$\langle V \rangle = 2V\alpha\beta \quad (7)$$

If  $\alpha = \beta = \frac{1}{\sqrt{2}}$ , we get  $\psi_1 = \psi_2 = \frac{e^{-iVt}}{\sqrt{2}}$ ,  $\langle V \rangle = V$  (7a)

If  $\beta = -\alpha = -\frac{1}{\sqrt{2}}$ , we get  $\frac{e^{iVt}}{\sqrt{2}}$ ;  $\psi_2 = -\frac{e^{iVt}}{\sqrt{2}}$ ,  $\langle V \rangle = -V$  (7b)

I.e. dimer excitation can lead both to the deepening and vice-versa to the becoming more shallow of the pear potential between the resonant molecules. As a rule, only these extreme cases ( $\alpha = \beta = 1/\sqrt{2}$ , and  $\beta = -\alpha = -\frac{1}{\sqrt{2}}$ ) were taken into consideration by the other authors<sup>4</sup>.

Our hypothesis is in that only the conservation laws define the limits imposed on  $\alpha$  and  $\beta$ . I.e.  $\alpha$  and  $\beta$  can be permanent.

In our case the figures  $\alpha$  and  $\beta$  ( $\alpha^2 + \beta^2 = 1$ ) characterize the casual excitation probability distribution between two molecules of dimer at an initial time. These figures define the additional potentials that vary dimer structure. It is possible to estimate the additions to a pear potential.  $V$  is the matrix element of the operator of the dipole-dipole interaction between molecules

(quadrupole-quadrupole interaction is not taken into account)

$$V_{01} = \langle \psi_1^1 \psi_0^0 | \frac{(\vec{\mu}_0, \vec{\mu}_1) - 3(\vec{n}, \vec{\mu}_0)(\vec{n}, \vec{\mu}_1)}{r^3} | \psi_1^0 \psi_0^1 \rangle, \quad (8)$$

where  $\psi_1^0$ ,  $\psi_0^0$ ,  $\psi_1^1$  and  $\psi_0^1$  are wave functions of excited and nonexcited molecules. The consideration uses the wave functions the unperturbed Hamiltonian;  $\mu_0$ ,  $\mu_1$  are the operators of the dipole moments for the molecules,  $\vec{n}$  is a unit vector along the direction between the molecules centers,  $r$  is the distance between the molecules centers.

$V_{01}$  was analyzed in details in the work<sup>3</sup>.

If  $\vec{n}$  is along the direction  $\vec{\mu}_0$  and  $\vec{\mu}_1$  the two last being parallel, we have  $V_{01} = -2 \frac{|\vec{\mu}_0|_0^1 |\vec{\mu}_1|_0^1}{r^3} \approx -2 \frac{\mu_0^1}{r^3}$  where  $\mu_0^1$  is the matrix element of dipole moments of transition for resonant mode of the molecule. Supposing  $\alpha = \beta = 1/\sqrt{2}$ ,  $\mu_0^1 = 0,5D$ ,  $r = 3\text{\AA}$ , we obtain  $V = 66,3^\circ\text{K}$ . Supposing  $\alpha = \beta = 1/\sqrt{2}$ ,  $\mu_0^1 = 1D$  (typical matrix element of dipole moments of transition for molecules in visible range).  $r = 3\text{\AA}$  we obtain  $V = 265^\circ\text{K}$  ( $180\text{ cm}^{-1}$ ).

If the two molecules are modeled by two undivided particles, than the dimers energetic states can be drawn in such way as the energetic states of two atoms molecules. Analogous energetic terms must take place. They are drawn on the figure. At this figure the intermediate states ( $0,5 > \alpha\beta > -0,5$ ) are not showed.

I.e. in case of dimer excitation, e.g. due to previous excitation on one of the molecule before the clinging in dimer, the pear potential be deepened by the amount  $V$ . For dimers in gaseous phases it means the time life increase, if the collisions are weak. For dimers on a surface it means the adsorption potential increase of every molecules.

For the first time the adsorption potential change hypothesis for resonant molecules in laser fields was proposed in the work<sup>5</sup>, but these adsorption potential changes estimations due to prolong photon exchange only was made for the first time in the work<sup>6</sup>.

Let us consider resonant to laser radiation molecules, which built dimers, e.g. during cooling in a gasdynamic jet. The cooling gas is irradiated in the spot just after critical part of the jet. The interesting results in the frame of the above mentioned scheme

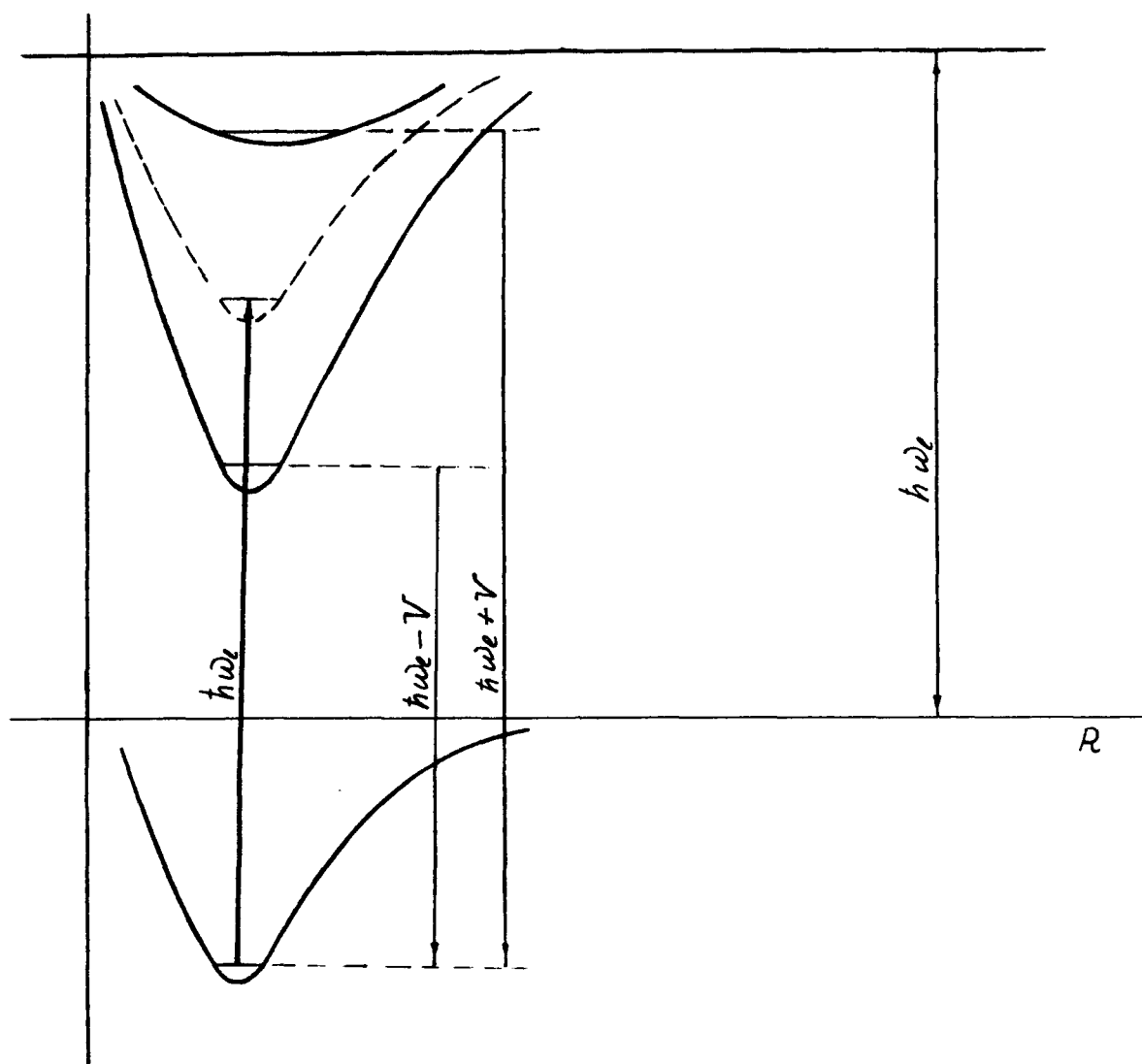


Figure. The energetic dimer states scheme when excited. The resonant quantum frequency for alone molecule is  $\omega_1$ . For simplicity the excitation is supposed not to vary  $R$  the distance between the molecules. In the upper figure part only the two terms for  $\alpha \cdot \beta = -1/2$  (low term) and for  $\alpha \cdot \beta = 1/2$  (highest term) are presented by the solid line. The lowest vibrational states are shown for these terms only. The thick arrow up shows the laser radiation action result. The thin arrows down show the possible system transitions, e.g. in case of spontaneous irradiation.

were obtained in works<sup>7,8</sup>, where benzonitrile molecules in the limit of several percents in the mixture with a noble gas were cooled (rotational temperature was about 4°K) and excited by the light ( $\lambda = 2738.8 \text{ \AA}$ ). Part of the excited and non excited molecules unites in dimers. If the molecules clinging in dimer was adiabatic enough

(smooth) that the migration of a quantum of excitation phase has not been changed at the unite time point (i.e.  $\alpha = 1$ ,  $\beta = 0$ .), the excitation quantum presence does not vary the pear potential. Further the dimer collisions with the other particles vary the phase of the quantum excitation migration, the multiplication  $\alpha \cdot \beta$  becomes not equal zero, i.e. the weakening or the deepening of the pear potential will take place.

Let us consider the extreme case  $V \gg kT$ . In this case the states with a violet shift ( $\alpha \cdot \beta > 0$ ) will have small probability. If the quantum excitation energy does not convert (degrade) completely in the other forms of energy after several dimer collision with the other particles, than the system will be on the lowest vibrational level of the lowest term  $\alpha \cdot \beta = -0.5$ . The changes will give rise to the red shift in spectrum: after mixture irradiation with a resonant laser frequency  $\omega_1$  one will find the additional line  $\omega_1 - V$  and some more faint lines between them. We think that the quantum exchange effects should be taken into account in the explanation of the experimental results<sup>7,8</sup>, where the red shift  $-98 \text{ cm}^{-1}$  was found.

The ratio of the probabilities of the system beings on the highest term ( $\alpha \cdot \beta = 0.5$ , the zero vibrational level) and on the lowest term ( $\alpha \cdot \beta = -0.5$ , the zeroth vibrational level) is equal  $\exp(-2V/kT)$ . If one takes the the upper figures ( $V = 180 \text{ cm}^{-1}$  or  $V = 98 \text{ cm}^{-1}$ ,  $T = 4^\circ \text{K}$ ) the extreme small number of dimers in the highest term will be found. When cooling in differ from the alone molecules the nonexcited dimers have the weak light absorption band  $\omega_1 \pm 2\alpha \cdot \beta \cdot V$  ( $0.5 > \alpha \cdot \beta > -0.5$ ) besides the strong absorption on  $\omega_1$ . The dimer excitation with quantum  $\omega_1 - V$  leads to its strengthening, and vice-versa the dimer excitation with quantum  $\omega_1 + V$  leads to more shallow pear potential.

In case of uniform irradiation on all frequencies and the absence of the phase change for migration of a quantum of excitation (in this work we made just the opposite assumption) and other things being equal the pear potential in dimer becomes weaker due to unevenness of Boltzmann's distribution.

In our case the probability change of dimer decomposition after excitation is possible to find analytically for any ratio between  $V$  and  $kT$ , if the quantum time life is much more larger than the mean time between collisions and  $\alpha$  and  $\beta$  can change because of the collision. The excited dimer decomposition is supposed to take place after the gaining the additional energy due to collision with another particle. The energy distribution of the new terms defined by the  $\alpha$  and  $\beta$  is implied to be Boltzmann's one. I.e. the possibility of system being on a term defined by  $\alpha$  and  $\beta$  ( $\alpha^2 + \beta^2 = 1$ ) is equal

$$P_{\alpha\beta} = \left[ \exp(-2\alpha\beta V/kT) \right] / \left( \frac{1}{2\pi} \int_1^{\infty} d\lambda \exp(-2\alpha\beta V/kT) \right) \quad (9)$$

The integration is made over the circle with a unit radius. The expression for the probabilities ratio in the excitation presence  $P_1$  and in the excitation absence  $P_0$  is

$$\frac{P_1}{P_0} = \frac{1}{2\pi} \int_1^{\infty} dP_{\alpha\beta} \exp[-(E_a - 2\alpha\beta V)/kT] / \exp(-E_a/kT) = I_0^{-1}(V/kT) \quad (10)$$

where  $I_0(V/kT)$  is the modified Bessel function of zeroth order,  $E_a$  is the dissociation energy of unexcited dimer. So the dimer excitation may lead to the dimer strengthening in common case after several collisions.

The adsorption potential deepening for the molecules united in dimer on a surface and the pear potential deepening for the molecules united in dimer in gas because of excitation one of the particles is undoubtedly interesting for practical applications.

#### REFERENCES

1. Alexandrov M.L., Kusner Yu.S., Gasdynamical Molecular, ions and clusters beams, (in Russian), 1989, Leningrad, 271p..
2. Kim K.C., Filip H., Person W.B., "Inhibition of Homogeneous Condensation of  $SF_6$  by Vibrational Excitation," Chem. Phys. Lett. 1978, v.54, No2, pp.253-257.
3. Kravchenko V.A., Orlov A.N., Petrov Yu.N., Prokhorov A.M., Resonant Heterogeneous Processes in a Laser Field (monograph), Proceedings of General Physics Institute, Acad. of Scien. USSR, 1989, v.11, 253. Nova Science Publishers, Inc.
4. Shahparronov M.I., Philippov L.P. Study of *Structure*, Heat Moving and Properties of Liquids. (in Russian), 1986, Moscow State Univ. 358p.
5. Karlov N.V., Orlov A.N., Petrov Yu.N., Prokhorov A.M., "Interaction between molecules in the resonant electromagnetic field", Pisma v zhurnal tehnikeskoi fiziki, 1982, v.8, No 7, pp 426-428.
6. Orlov A.N., "Resonant molecules behavior change on surface in the laser field", Pisma v zhurnal tehnikeskoi fiziki, 1988, v.14, No 6, pp 532-537.
7. Kobayashi Tohry, Honma Kenji, Kajimoto Okitsugu and Tsuchiya Soji, "Benzonitrile and its van der Waals complexes studied in a free jet. I. The LIF spectra and the structure", J. Chem. Phys. (1987), v.86, pp.1111-1118.
8. Kobayashi Tohry and Kajimoto Okitsugu, "Benzonitrile and its van der Waals complexes studied in a free jet. II. Dynamics in the excited state: The effect of changing the degrees of freedom of partner molecules, " J. Chem. Phys. (1987), v.86, pp.1118-1124.
9. Maksimov V.V., Orlov A.N., Petrov Yu.N., Prokhorov A.M., "About Electromagnetic Field Effects on Molecules Associates in Gaseous Phase," Theor. Foundations of Chem. Engineering, 1994, V.28, No.4, (to be published)

## **Session 2.**

**New aspects of laser diagnostics  
of media and interfaces.**



# Application of IR-laser-light scattering for non-destructive control of near-surface regions in semiconductor substrates

V.P.Kalinushkin, D.I.Murin, V.A.Yuryev, O.V.Astafiev,  
A.I.Buvaltsev

General Physics Institute of RAS, 38 Vavilov street,  
B-333, Moscow, Russia.

## ABSTRACT

The method for investigation and control of large-scale recombination-active defects in near-surface regions of semiconductor wafers is proposed. The potentialities of the technique proposed are illustrated by the example of germanium single crystals.

## 1. INTRODUCTION

At present the methods, which allow performing non-destructive control of presence of various inhomogeneities - especially those which affect the electrophysical properties - in near-surface regions of semiconductor substrates, arouse a great interest. This work is targeted at consideration of utilization possibilities of the low-angle mid-IR-light scattering technique (LAIS) for revealing and non-destructive control of inhomogeneities affecting carrier life - so called large-scale recombination-active defects (LSRDs). Such imperfections as impurity inclusions and precipitates, defects of structure (dislocations, swirls, grain boundaries, etc.), impurity atmospheres around them and other impurity accumulations - if contain enough recombination and/or glue centers - may fall into this type of defects.

## 2. LAIS FOR LSRD CONTROL

For the beginning we shall briefly remind the basic principles of LAIS technique <sup>1,2</sup>.

Every inhomogeneities in crystals have dielectric constants diffe-

rent from average one outside them, that result in elastic scattering of light. Registering the scattered light one can obtain information about inhomogeneities in the crystal.

In LAIS, as distinct from the laser scattering tomography,<sup>3</sup> scattered light is registered at relatively small angles (usually from about  $2^\circ$  to less than  $15^\circ$  in the crystal) and laser light with large wave-length (usually  $10.6\text{ }\mu\text{m}$  or  $5.4\text{ }\mu\text{m}$ ) is used as a probe radiation, and scattered light being registered from all the defects in the probed with laser beam crystal volume.<sup>1</sup> In experiments, the light scattering diagrams of this region are measured, from which the sizes of scatterers, the value of  $(C\Delta\epsilon^2)^{1,2}$  - where  $C$  is the scatterers concentration,  $\Delta\epsilon$  is the dielectric constant deviation in them - and a number of other parameters are estimated.<sup>5-7</sup> Employing of light with large wave-length as a probe beam make LAIS sensitive to the most important for semiconductors class of inhomogeneities, i.e. to the domains with enhanced (or inverted) free carrier concentration. And the scattered light registering at small angles allow observing the defects with the sizes of an order of the wave-length (i.e. from several to several dozens  $\mu\text{m}$ ). LAIS is very sensitive, it allow to register the defects with  $\Delta\epsilon$  down to  $10^{-4}$ - $10^{-5}$ . Using LAIS, so called large-scale electrically active defects accumulations (LSDAs) have been registered and thoroughly investigated in a number of semiconductors.<sup>5-15</sup>

One of the main disadvantages of standard LAIS is its inability to discriminate between scattering from crystal bulk and surface. The way allowing to reveal ISRDs in near-surface substrate layers using LAIS is proposed in the present paper.

The following technique for ISRD revealing has been developed within the framework of traditional LAIS: using pulse photoexcitation the electron-hole pairs are generated in the sample; if the ISRDs are contained in the crystal then the regions with lowered free carrier

---

<sup>1)</sup> Now the technique is developed within LAIS framework, which allow defect visualization,<sup>4</sup> but in this paper the case in point is the standard LAIS.<sup>1,2</sup>

concentration - if ISRDs are the centers of accelerated recombination - or with enhanced one - if ISRDs are the glue centers - arise round them. The dielectric constant of these regions is different from that outside them that result in light scattering by them.  $\Delta\epsilon$  is evidently proportional to concentration of generated inequilibrium carriers. So in the case of pulse pumping, the light scattering by ISRDs is also of pulse character. Respectively, the scattering by all other types of defects, which do not interact with current carriers, does not change in time. So registering only the pulse component one can separate the scattering by ISRDs from that by other defects.

The last technique has been realized for Si and Ge,<sup>16,17</sup> with photoexcitation sources been chosen which have allowed bulk generation of carriers (two-photon absorption of  $\text{CaF}_2:\text{Dy}^{2+}$  laser radiation has been used for Ge and  $\text{Yag}:\text{Nd}^{3+}$  laser has been used for Si pumping). Unfortunately one cannot segregate the scattering by near-surface and in-bulk defects in these experiments.

In order to make segregation of near-surface fraction, it is being proposed in present work to generate carriers in narrow near-surface zone; they will penetrate in crystal bulk only due to diffusion. ISRDs will evidently be revealed by light scattering only in that part of crystal where inequilibrium carriers diffuse, i.e. in the layer of  $(D\tau)^{1/2}$  in thickness where  $D$  is carrier diffusion coefficient,  $\tau$  is its life. In many industrially used in reality crystals, this layer thickness runs between 1  $\mu\text{m}$  and 20  $\mu\text{m}$ .

### 3. EXAMPLE OF Ge SINGLE CRYSTALS

#### 3.1. Experimental setup, samples and conditions

In this work, the standard setup for LAIS has been used, it is described in detail e.g. in <sup>1,2</sup> (Fig.1). Continuous  $\text{CO}_2$ -laser ( $\lambda=10.6 \mu\text{m}$ , power  $P=3 \text{ Watt}$ ) has been used as a probe beam source.  $\text{Yag}:\text{Nd}^{3+}$  giant-pulse laser (pulse duration  $\tau_p=50 \text{ ns}$ , pulse energy  $E_p=0.3 \text{ mJ}$ , pulse frequency  $f_p=1\text{kHz}$ , wave-length  $\lambda_p=1.06 \mu\text{m}$ , spot diameter on the sample  $d_p=8 \text{ mm}$ ) has been used for inequilibrium carriers generation. Ge single crystals have been chosen as a research object, as the above pulse

laser pumps efficiently the inequilibrium carriers in its near-surface region.

The samples of pure Ge with effective carrier life of less than 50  $\mu$ s has been investigated. The life-time has been estimated from transmittance signal decay which has been registered with photoreceiver (Fig.1). It is determined either by bulk life or by surface recombination rate. Volume life has lain in the range of 100-200  $\mu$ s.

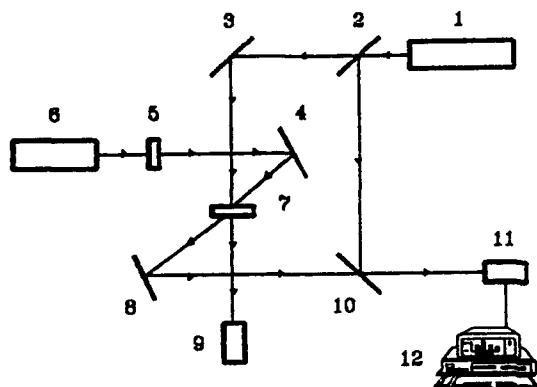


Fig.1. Experimental setup.  
1 - CO<sub>2</sub>-laser, 2,10 - semi-transparent mirrors, 3,4 - mirrors, 5 - filters, 6 - pulse laser (Yag:Nd<sup>3+</sup>), 7 - sample, 8 - movable mirror, 9,11 - photoreceivers, 12 - computer.

All the crystals were grown under the same conditions and practically did not differ by their electrophysical properties. In them,  $N_D - N_A \approx 10^{11} \text{ cm}^{-3}$ , dislocation density  $N_d \approx 10^3 - 10^4 \text{ cm}^{-2}$ . They were studied beforehand by LAIS, and the samples specially chosen with close LSDA parameters. Only the surface preparation varied - a part of the samples was subjected to mechanical polishing, after which damaged layer remained, the others were treated by chemico-dynamical polishing for damaged layer etching off.

The specimens' thickness has been ranged from 3 to 5  $\mu$ m. Three mechanically and three chemically polished wafers have been investigated, every couple of which been the nearest neighbours in the ingot. All the substrates have been washed in a special way to remove dust and surface contaminations.

### 3.2. Results and discussion

In Fig.2, the characteristic light scattering diagrams of LSDAs in Ge crystals, measured without photoexcitation, and the characteristic scattering diagrams of LSRDs in mechanically and chemically polished

Ge samples, measured with photoexcitation, are plotted ( $I_{sc}$  is the light scattering intensity,  $W_0$  is the probe beam power,  $\theta$  is the scattering angle inside the crystal). LSDAs are distributed in whole the crystal volume and the light scattering by them is practically independent of the surface polishing procedure,<sup>10,13,14</sup> this has been detected in present experiments either. Whereas the scattering by these crystals with the surface photoexcitation considerably differs depending on the surface preparation procedure. In the case of mechanical polishing, the scattering by small-sized LSRDs has been detected (so called plateau, Fig.2, curve 2). In the case of chemical polishing the scattering is much less intense and the diagrams are quite alike in their shapes to those measured without photoexcitation (Fig.2, curves 1,3). In both cases the procedure of surface washing has not affected the light scattering.

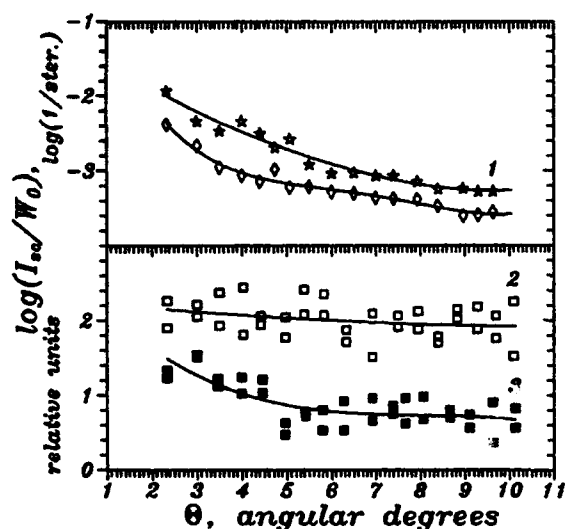


Fig.2. Light scattering diagrams of Ge. 1 - without photoexcitation, 2 - mechanically polished sample, 3 - chemically polished sample; 2,3 - with photoexcitation.

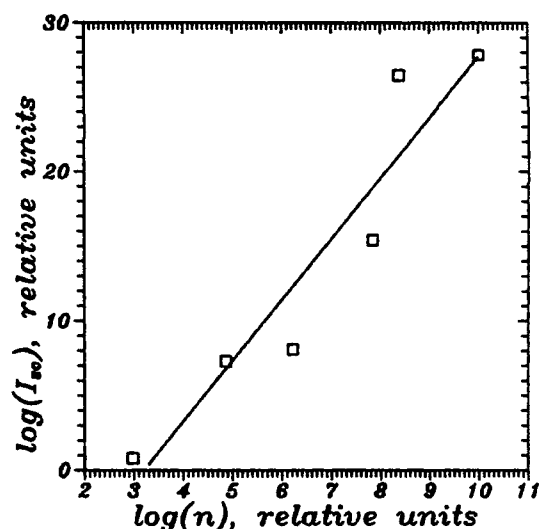


Fig.3. Light scattering intensity vs excited carrier concentration (mechanically polished sample).

The dependence of light scattering intensity upon excited carrier concentration is depicted in Fig.3 for the samples subjected to mechanical polishing ( $n$  is proportional to excited carrier concentration). This dependence is of non-linear character that is an obvious evidence that namely ISRDs are registered in the experiments.<sup>16</sup> Analogous experiments with chemically polished Ge are hard to be done because of very low scattering intensity.

We consider the defects of damaged layer to have been revealed by use of surface photoexcitation, which have appeared to be the centers of accelerated recombination. Their sizes are small and not larger than 2  $\mu\text{m}$ . Note that not the defects themselves are registered in the experiments but the regions with lowered carrier concentration around the defects, so the defects' sizes are even less than indicated.

For the crystals after chemico-mechanical polishing the same defects as without photoexcitation are likely registered with pumping too. (These ISRDs are likely the same LSDAs but located in the near-surface layer.) This is quite natural, as LSDAs are recombination-active in pure Ge (as previously shown in <sup>17</sup>).

#### 4. CONCLUSION

The sum total of the present work is from our standpoint that the possibility of defect revealing in near-surface layers (from 1 to 20  $\mu\text{m}$  in thickness) of semiconductor substrates by use of contactless non-destructive technique has been demonstrated experimentally. The first obvious practical application of this technique is the development of incoming and step control of Si (the denuded zone depth after inner gettering is usually 5-10  $\mu\text{m}$  so Si is convenient for such work and the method is applicable for Si). No problems are seen in analyzing of epilayers with the thickness of several  $\mu\text{m}$  using this technique. But analogous method developing for analysis of epitaxial layers with the thickness of less than or about 1  $\mu\text{m}$  does require additional investigations, however.

## 5. REFERENCES

1. V.P.Kalinushkin, "Investigation of impurity centers in semiconductors by IR-laser emission scattering techniques," *Proc.Inst.Gen. Phys.Acad.Sci.USSR*, Vol.4, *Laser Methods of Defect Investigations in Semiconductors and Dielectrics*, New York, Nova, pp.1-75, 1988 and references therein.
2. V.V.Voronkov, V.P.Kalinushkin, D.I.Murin et.al. "Application of elastic IR light scattering for investigation of large-scale electrically active defects in semiconductors," *J.Cryst.Growth*, Vol.103, pp.126-130, 1990.
3. T.Ogawa, N.Nango, "Infrared light scattering tomography with an electrical streak camera for characterization of semiconductor crystals," *Rev.Sci.Instrum.*, Vol.57, pp.1135-1139, 1986.
4. O.V.Astafiev, V.P.Kalinushkin, V.A.Yuryev, "Non-destructive method for visualization of free carrier accumulations in standard semiconductor wafers," *Proc. ALT'93 (this issue)*.
5. V.P.Kalinushkin, V.A.Yuryev, D.I.Murin, "Large-scale accumulations of electrically active defects in single crystals of indium phosphide," *Soviet Phys. - Semicond.*, Vol.25, No.5, pp.798-805, May 1991.
6. V.P.Kalinushkin, V.A.Yuryev, D.I.Murin, M.G.Ploppa, "On the nature of large-scale electrically active defect accumulations in InP and GaAs," *Semicond.Sci.Technol.*, Vol.7, pp.A255-A262, July 1992.
7. S.E.Zabolotskii, V.P.Kalinushkin, D.I.Murin et.al., "Determination of parameters of point centers constituting 'weak' impurity clusters in semiconductor materials," *Soviet Phys. - Semicond.*, Vol.21, No.8, p.1364-1368, Aug. 1987.
8. V.P.Kalinushkin, V.A.Yuryev, D.I.Murin et.al., "Large-scale impurity accumulations in III-V and II-VI materials," *Proc. 7-th Intern.Conf. on Microelectronics (Microelectronics'90)*, Vol.1, Minsk, A.S.Popov All Union Society, p.57-59, 1990.
9. S.E.Zabolotskii, V.P.Kalinushkin, T.M.Murina et.al., "The influence of growth rate on the impurity cloud parameters in pure silicon," *Phys.Stat.Sol.(a)*, Vol.88, pp.539-542, 1985.
10. V.V.Voronkov, G.I.Voronkova, V.N.Golovina et.al., "Impurity

clouds in silicon and germanium," *J.Cryst.Growth*, Vol.52, pp.939-942, 1981.

11. A.N.Buzynin, S.E.Zabolotskii, V.P.Kalinushkin et.al., "Large-scale electrically active impurity accumulations in silicon crystals grown by Czochralski method," *Soviet Phys. - Semicond.*, Vol.24, No.2, pp.264-270, Febr.1990.

12. A.V.Batunina, V.V.Voronkov, G.I.Voronkova et.al., "Influence of rapidly diffusing impurities on small-angle scattering of light in silicon," *Soviet Phys. - Semicond.*, Vol.22, No.7, pp.1308-1310, July 1988.

13. N.V.Veselovskaya, V.V.Voronkov, G.I.Voronkova et.al., "The temperature of the oxygen cloud formation in germanium," *Soviet Phys. - Solid State*, Vol.27, No.5, pp.1331-1333, May 1985.

14. V.V.Voronkov, G.I.Voronkova, V.P.Kalinushkin et.al., "The character of electrical activity of the centers forming impurity clouds in germanium," *Soviet Phys. - Semicond.*, Vol.18, No.12, pp.2222-2224, Dec. 1984.

15. A.V.Voronkova, V.P.Kalinushkin, N.S.Sysoyeva et.al., "Interaction of gold with impurity clouds in silicon," *Soviet Phys. - Semicond.*, Vol.19, No.10, pp.1902-1904, Oct. 1985.

16. V.P.Kalinushkin, D.I.Murin, T.M.Murina et.al., "Application of the small-angle light scattering method for investigation of the large-scale centers of recombination and gluing in semiconductor crystals," *Soviet Phys. - Microelectronics*, Vol.15, No.6, pp.523-528, June 1986.

17. V.V.Voronkov, T.M.Murina, G.I.Voronkova et.al., "Influence of photoexcitation on light scattering by single crystals of pure germanium," *Soviet Phys. - Solid State*, Vol.20, No.5, pp.1365-1368, May 1978.



# Non-destructive method for visualization of free carrier accumulations in standard semiconductors wafers

O V Astafiev, V P Kalinushkin, V A Yuryev

Laboratory of Laser Defectoscopy of Semiconductors,  
General Physics Institute of the Russian Academy of Sciences,  
38 Vavilov Street, V-333 GSP-1, Moscow 117942, Russia

## ABSTRACT

A new non-destructive method for visualization of free carrier accumulations in standard semiconductors wafers (VCA or scanning low-angle light scattering, SLAIS) is being proposed firstly. The method have been applied to visualize large-scale electrically active defect accumulation (ISDAs) in a number of semiconductor crystals. It allows mapping and investigating technological semiconductor wafers, being sensitive to low concentration of free carriers in the accumulations.

## 1. INTRODUCTION

In a number of papers,<sup>1-3</sup> a method of law-angle light scattering (LAIS) was described which allows investigating the accumulations of electrically-active defects with the sizes of 1-50  $\mu\text{m}$  which are usually present in semiconductor crystals.<sup>4-6</sup> A plane wave of IR-laser radiation is applied in LAIS to probe semiconductor crystals. LAIS is non-destructive and yields the following integral values:

- 1) concentration of accumulations  $C$  multiplied by the square of effective differential concentration of free carriers in the accumulation  $\Delta n_{\text{eff}}$ ;
- 2) effective sizes of defects  $a_{\text{eff}}$ .

A new non-destructive method for visualization of free carrier accumulations in standard semiconductors wafers (VCA) is being introduced in the current paper. Like LAIS, VCA is based on elastic low-angle scattering of plane wave of laser radiation in the region of wavelengths where most of semiconductors are transparent, i.e in mid-infra-red region.

## 2. VCA PHYSICAL BASIS

The concentrations of free carriers in the accumulations of electrically-active defects are different from that in a crystal bulk. This difference produces correspondent change in the accumulations' dielectric constant at the cycle frequency  $\omega$ , the change is

$$\Delta\epsilon = - \frac{4\pi\Delta n e^2}{m_{\text{opt}} \omega^2} \quad (1)$$

where  $\Delta n$  is a difference in free carrier concentration between the crystal volume and the accumulation,  $e$  is the electron charge,  $m_{\text{opt}}$  is the effective mass of free carriers at frequency  $\omega$ .  $|\Delta\epsilon|$  increases with decreasing of radiation frequency  $\omega$ , so large wave-length makes the method more sensitive to  $\Delta n$ . A usual value of  $\Delta n$  is small and  $|\Delta\epsilon| \ll \epsilon$  ( $\epsilon$  is dielectric constant in semiconductor bulk).

The VCA principle scheme is shown in Fig.1. The plane wave of laser source illuminates a thin semiconductor crystal with polished surfaces (usually standard technological wafer before structure production). The wafer is located in the focal plane of a lens  $L_1$ . Let a defect to be in the crystal bulk in the front focal plane of  $L_1$ . It scatters the probe wave producing an additional scattered wave, which diverge in an angle of an order of  $\frac{\lambda}{a}$  where  $\lambda$  is a wave-length,  $a$  is the defect's characteristic size. A resultant wave after the defect is a sum of non-disturbed plane wave and that scattered by the defect. The lens  $L_1$  condenses the plane wave in the back focus to a spot with the size of about  $(\lambda f_1)/D_1$  where  $D_1$  is a diameter of the probe plane-wave beam. A small mirror turned to the angle of 45 degrees to focal plane or absorbing screen is positioned in the back focus for removing the probe wave radiation. The scattered wave, being almost plane wave with characteristic beam diameter of  $\frac{\lambda}{a} f_1$ , after  $L_1$ , comes to the second lens  $L_2$  almost without losses - if the mirror size is smaller than  $\frac{\lambda}{a} f_1$ . So the scattered wave without probe radiation achieves the lens  $L_2$  and the image of the defect is formed in the back focus of  $L_2$  in the scattered rays.

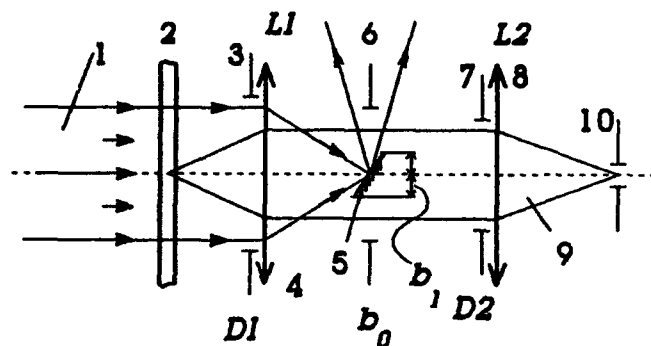


Fig.1. The principle scheme of VCA. 1 - the probe wave; 2 - the tested sample with polished surfaces; 3 - a diaphragm with diameter of  $D1$  in the plane of the lens  $L1$ ; 4 - the lens  $L1$ ; 5 - "dark field" with radius  $b_0$  in the back focus plane of  $L1$ ; 6 - a diaphragm with the radius  $b_1$  in the plane of "dark field"; 7 - a diaphragm with the diameter of  $D1$  in the plane of the lens  $L2$ ; 8 - the lens  $L2$ ; 9 - the scattered wave; 10 - a photoreceiver.

The scheme described above is a well known in microscopy method of so called "dark field", but using of the laser source for producing a good plane wave and applying mid-IR radiation make it possible to visualize accumulations of electrically-active defects.

### 3. EXPERIMENTAL SETUP

To realize the described above method the experimental setup was constructed. The scheme of VCA setup is shown in Fig.2. It had some unimportant differences from the ideal setup plotted in Fig.1, which were connected with some technical and financial problems. A probe wave from the IR-laser source came to a long-focus lens  $L1$  ( $f = 100$  mm), which slightly focused radiation on the sample. The sample was shifted in a plane in front of the focus of the lens  $L2$  near it,  $L2$  formed an image of the sample on the photoreceiver. The probe beam was removed by means of an absorbing screen which was placed in front of the plane of the lens  $L2$ . The diameter of the probe beam was much smaller than the diameter of  $L2$  due to focusing by lens  $L1$ , so the "dark field" was much bigger than the probe beam diameter. It means that almost no matter where to place the "dark field": in the back focus of  $L2$  or imme-

diately in the plane of the lens L2.

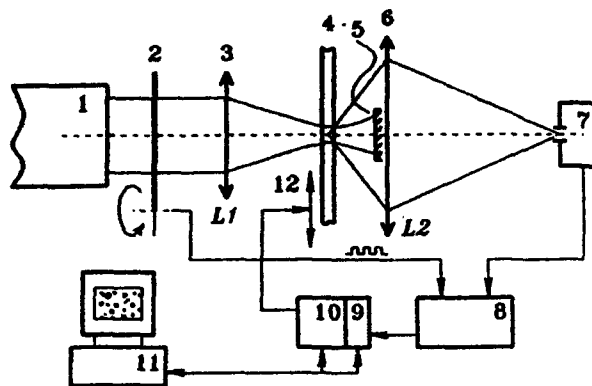


Fig.2. Experimental setup.

1 - CO<sub>2</sub>-laser; 2 - an obturator; 3 - the lens L1 for probe wave focusing; 4 - sample; 5 - "dark field"; 6 - the image forming lens; 7 - IR-photoreceiver (liquid nitrogen cooled Cd-Hg-Te); 8 - an amplifier with a synchronous detector; 9 - ADC; 10 - step motor control system; 11 - a computer for the system control and data acquisition; 12 - a step motors for studied sample moving.

The sample was moved over two coordinates perpendicularly to the optical axis and a signal proportional to intensity of the scattered wave was registered by IR-photoreceiver (Cd-Hg-Te cooled with liquid nitrogen). The receiver detectivity was  $3 \cdot 10^{12} \text{ } \sqrt{\text{Hz}}/\text{Watt}$ , its size was  $150 \text{ } \mu\text{m} \times 150 \text{ } \mu\text{m}$ , integration time for measurement in one point was about  $10^{-2} \text{ s}$ , i.e. the receiver detected  $5 \cdot 10^{-10} \text{ Watt}$  of the incident radiation power. The analog signal was digitized and transferred into computer to produce and save image.

CO<sub>2</sub>-laser was used as a source of probe wave, its wave-length was  $10.6 \text{ } \mu\text{m}$ , with power been of an order of 0.5 Watt.

This type of non-optimized setup is sensitive to free carrier concentration within defect down to  $10^{14} \text{ cm}^{-3}$  (this value has been calculated for the defects with the sizes  $a$  of about  $10 \text{ } \mu\text{m}$ ).

#### 4. THE FIRST EXPERIMENTAL RESULTS

Some images of standard semiconductor substrates are presented in Fig.3; those of as-grown dislocationless Si with diameter 76 mm doped

with boron ( $\rho \approx 10 \text{ ohm} \cdot \text{cm}$ ), annealed at  $700^\circ \text{C}$  for 8 hours dislocationless Si with diameter 76 mm doped with boron ( $\rho \approx 10 \text{ ohm} \cdot \text{cm}$ ), as-grown dislocationless Si with diameter 76 mm doped with phosphorus ( $\rho \approx 4.5 \text{ ohm} \cdot \text{cm}$ ) and SI LEC GaAs annealed under vacuum in sealed quartz ampule at  $900^\circ \text{C}$  ( $\rho > 10^7 \text{ ohm} \cdot \text{cm}$ ;  $\mu > 4000 \text{ cm}^2/\text{V} \cdot \text{s}$  at 300K) are plotted in Figs 3a-3d. Silicon (Figs. 3a-3b) was investigated beforehand by chemical etching: distribution of the defects in as-grown silicon was homogeneous and distribution of them in annealed one was striped. We consider that small white spots are ISDAs, which previously were investigated by LAIS.<sup>1-6</sup> The large white spots are backgrounds from dust particles on the surfaces of the wafers.

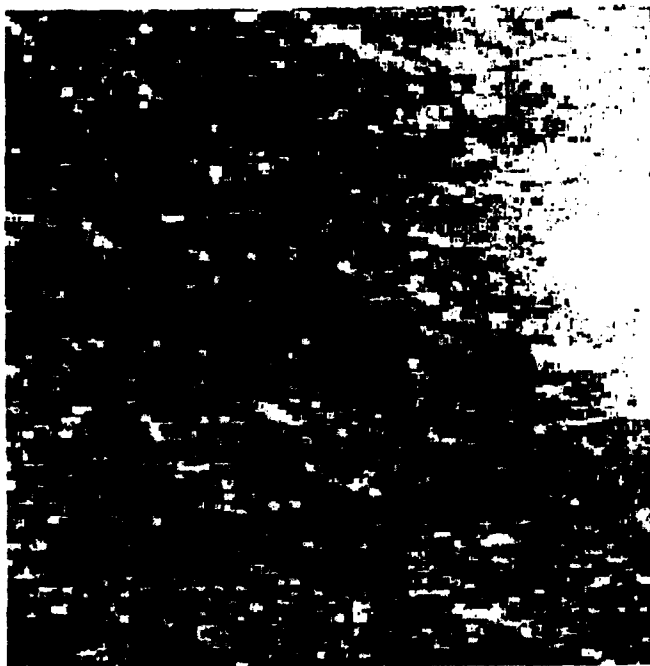


Fig.3. ISDA in semiconductor crystals. a) as-grown dislocationless Si with a diameter of 76 mm doped with boron ( $\rho \approx 10 \text{ ohm} \cdot \text{cm}$ ); b) annealed dislocationless Si with a diameter of 76 mm doped with boron ( $\rho \approx 10 \text{ ohm} \cdot \text{cm}$ ); c) as-grown dislocationless Si with a diameter of 76 mm doped with phosphorus ( $\rho \approx 4.5 \text{ ohm} \cdot \text{cm}$ ); d) SI LEC GaAs ( $\rho > 10^7 \text{ ohm} \cdot \text{cm}$ ;  $\mu > 4000 \text{ cm}^2/\text{V} \cdot \text{s}$ ). The area of 2 by 2  $\text{mm}^2$  is depicted in each pattern.

a)

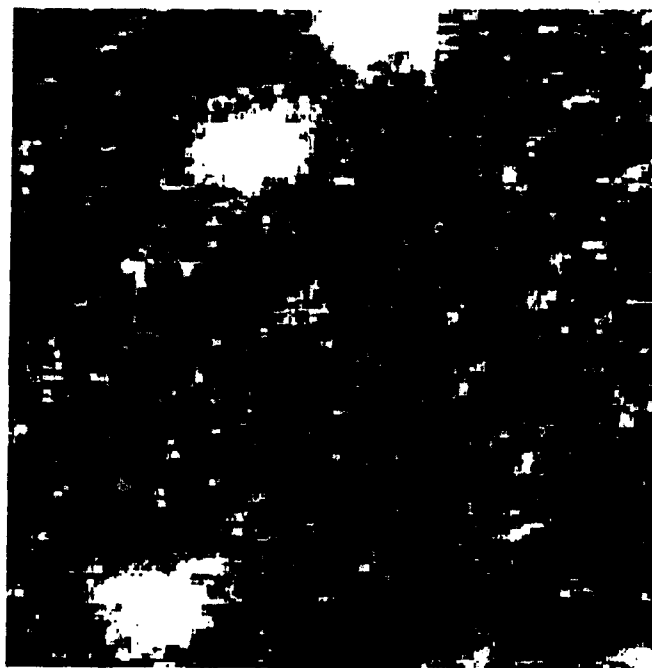


b)



c)

*Handwritten text, possibly a signature or date.*



d)

A signal from the small defects is higher approximately by 10 times for GaAs than for Si wafers. VCA intensity ratios for these wafers are the same as in LAIS, that allows to state that the same defects are registered in both methods. The defects concentrations for the Si wafers  $C$  are of an order of  $10^6 \text{ cm}^{-3}$ , and for the GaAs, it is about  $10^5 \text{ cm}^{-3}$ . These values are in rather good agreement with the data obtained by other methods such as LAIS, EBIC, etching.<sup>4,5</sup> We should add that the mentioned methods give only indirect information on this type of defects, whereas VCA gives numerical data for their main parameters. Let us assume for simplicity that the sizes of the defects are  $\approx 10 \text{ } \mu\text{m}$ . It has been obtained that  $\Delta E \approx 10^{-2}$  for GaAs,  $\Delta E \approx 10^{-3}$  for Si:P and Si:B. Free carrier concentrations in defects - from (1) - are  $\Delta n \approx 10^{16} \text{ cm}^{-3}$  for GaAs,  $\Delta n \approx 10^{15} \text{ cm}^{-3}$  for Si:P and Si:B.

## 5. CONCLUSION

VCA is a unique non-destructive method which allows to visualize large-scale electrically-active defect accumulations in semiconductor crystals. Laboratory device for VCA measurements has been developed.

It is sensitive to free carrier accumulations with sizes  $3\pm 20\mu\text{m}$  and carrier concentrations down to about  $10^{14}\text{cm}^{-3}$ . But we should note that there are many possibilities to improve strongly the characteristics of the device.

In addition to above discussion, we should mention that VCA probably may be used not only for substrate characterization but also for non-destructive control and visualization of elements of doped structures with small carrier concentrations directly in technological cycle.

## 6. REFERENCES

1. V.V.Voronkov, G.I.Voronkova, B.V.Zubov et.al., "The scattering of infra-red laser radiation as a method for investigation of local inhomogeneities in pure semiconductors," *Soviet Phys.- Solid State*, Vol.23, No.1, pp.65-74, January 1981.
2. V.V.Voronkov, V.P.Kalinushkin, D.I.Murin et.al. "Application of elastic IR light scattering for investigation of large-scale electrically active defects in semiconductors," *J.Cryst.Growth*, Vol.103, pp.126-130, 1990.
3. V.P.Kalinushkin, "Investigation of impurity centers in semiconductors by IR-laser emission scattering techniques," *Proc.Inst.Gen. Phys.Acad.Sci.USSR*, Vol.4, *Laser Methods of Defect Investigations in Semiconductors and Dielectrics*, New York, Nova, pp.1-75, 1988.
4. A.N.Buzynin, S.E.Zabolotskii, V.P.Kalinushkin et.al., "Large-scale electrically active impurity accumulations in silicon crystals grown by Czochralski method," *Soviet Phys. - Semicond.*, Vol.24, No.2, pp.264-270, February 1990.
5. V.P.Kalinushkin, V.A.Yuryev, D.I.Murin, M.G.Ploppa, "On the nature of large-scale electrically active defect accumulations in InP and GaAs," *Semicond.Sci.Technol.*, Vol.7, pp.A255-A262, July 1992.
6. V.V.Voronkov, G.I.Voronkova, V.N.Golovina et.al., "Impurity clouds in silicon and germanium," *J.Cryst.Growth*, Vol.52, pp.939-942, 1981.



## **Session 3.**

**New materials and structures  
for optics and optoelectronics.**

# Nonlinear optical properties of CuCl nanocrystallites

Bernd Hönerlage and Roland Lévy

IPCMS, Groupe d'Optique Nonlinéaire et d'Optoélectronique  
5, rue de l'Université  
67084 Strasbourg Cedex  
France

## ABSTRACT

We review the nonlinear optical properties and their dynamics for CuCl nanocrystallites, embedded in a borosilicate glass matrix. Because of the high exciton binding energy of this compound, elementary electronic excitations are always in the weak confinement regime. In this limit, the optical properties of the quantum dots and their dynamics are essentially described by those of the bulk material. One has to consider, however, that the lack of translational invariance modifies the selection rules of optical transitions and hinders a classification in terms of longitudinal and transverse excitons.

## 1. INTRODUCTION

Nanocrystalline structures or quantum dots have been extensively studied these recent years both, experimentally and theoretically. This interest was first stimulated by the prediction of a possible increase of optical nonlinearities due to confinement or local field effects<sup>1-4</sup>. In metallic materials, this latter effect enhances the nonlinearity considerably close to the plasmon resonance. Optical nonlinearities of such quantum dots have been studied using e.g. Ti, Ag or Au suspensions in liquids. Although these effect are important in metallic materials, they are of minor relevance in semiconductors.

Concerning the confinement in semiconductor quantum dots, two limiting cases can be distinguished. In the limit of strong confinement, electrons and holes are confined independently. In this case, the exciton binding energy  $E_{ex}^b$  (which measures the importance of the Coulomb interaction between electrons (e) in the conduction band and holes (h) in the valence band) is small with respect to the energy of confinement  $E_c^i$  of the quasiparticles ( $i = (e, h)$ ) inside the dot. Then, the Coulomb interaction can be treated as a perturbation of the electron and hole states.

The confinement quantizes the kinetic energy of the quasiparticles<sup>5</sup> and splits the continuous bands  $E(Q)$  of the bulk material into discrete levels. It is the lack of translational invariance which implies that the quasiparticle wavevector  $Q$  is not well defined and is no longer a good quantum number to characterize the quasiparticle energy  $E(Q)$ , as it is the case in bulk material. In addition, this lack of translational invariance also affects the selection rules in optical transitions<sup>6</sup> since wavevector conservation is no longer necessary.

In the strong confinement limit, the exciton Bohr radius  $a_B$  is large compared to the radius  $r$  of the quantum dot. If, however,  $a_B \ll r$  or  $E_{ex}^b \gg E_c^i$ , the limit of weak confinement is reached. In this case, it is a straight forward approximation<sup>5</sup> to consider excitons as good quasiparticles, to confine their center

of mass motion, and then to quantize their kinetic energy<sup>7,8</sup>. This is a valid approximation for CuCl.

Bulk CuCl presents a simple band structure with a direct gap at the center of the Brillouin zone. It gives rise to an exciton series labeled  $Z_3$ . Its ground state has  $\Gamma_2$  and  $\Gamma_5$  symmetries, a binding energy  $E_{ex}^b = 190\text{meV}$  and a Bohr radius  $a_B = 7 \text{ \AA}$ . Only the exciton of  $\Gamma_5$  symmetry is dipole active.

Two excitons may couple together and form biexcitons<sup>9</sup>. Its ground state of  $\Gamma_1$  symmetry has a binding energy of  $28\text{meV}$  with respect to the continuum of two-exciton states with  $\Gamma_2$  symmetry. The biexciton Bohr radius is about  $35 \text{ \AA}$ . The creation of biexcitons is allowed by two-photon absorption with a strong, resonantly enhanced transition probability. Biexcitons are quite stable with respect to perturbations, and the optical properties of CuCl are well described by a three-level system, showing strong optical nonlinearities with interesting dynamical aspects<sup>10,11</sup>. It is the aim of this publication to discuss the nonlinear optical properties of CuCl nanocrystallites and to compare them to those of bulk material.

Following Ekimov et al.<sup>12</sup>, we have prepared samples with various crystallite radii in a borosilicate glass matrix<sup>13</sup>. They show a rather large size distribution<sup>14</sup> due to the thermodynamic growing and annealing processes. For samples with nanocrystallites of a mean radius  $R > 120 \text{ \AA}$ , the exciton confinement energy  $E_c^{ex} < 0.1\text{meV}$ , leading only to a small inhomogeneous broadening of the line. In transmission measurements, at 2 K, the  $Z_3$  exciton absorption line is, however, quite broad ( $> 10 \text{ meV}$  FWHM) indicating an inhomogeneous broadening which is not due to the size distribution, but rather to potential fluctuations in the surrounding matrix. For  $R < 120 \text{ \AA}$ , a blue shift of the exciton line due to the confinement and an additional inhomogeneous broadening due to the size distribution of the nanocrystallites is observed. Following Ref. 5, the confinement gives rise to a blue shift of the exciton ground state energy :  $E_c^{ex} = \hbar^2 \pi^2 / 2M r^2$  where  $M$  is the effective exciton mass.

## 2. EXPERIMENTAL RESULTS AND DISCUSSION

We will now present different techniques of coherent and noncoherent spectroscopical methods which have been used to study the nonlinear optical properties of CuCl nanocrystallites.

### 2.1. Two-photon absorption measurements.

In order to study the absorption changes in the spectral region of the  $Z_3$  exciton line, we have performed "pump and probe" transmission measurements<sup>13,15</sup>. We measure the transmission of a weak and spectrally broad laser pulse ("test") through the samples, excited by spectrally narrow and tunable dye laser pulses. The test pulses are obtained from the superradiant emission of a dye cell, containing BiBuQ in toluene as active medium. It is pumped by UV light pulses from an XeCl excimer laser. In order to obtain dye laser pulses of 350 ps duration, we have used quenching mirrors around the dye laser cavity. The pump pulses, well synchronized with the test pulses, are obtained from a dye laser, using a grating working at grazing incidence. The duration of these pulses is about 15 ns and its spectral width  $\Delta E < 0.05\text{meV}$  (FWHM). The photon energy of the dye laser can be tuned through the  $Z_3$  exciton resonance.

The samples, containing quantum dots of various mean radii, are cooled down in a cryostat, cooled

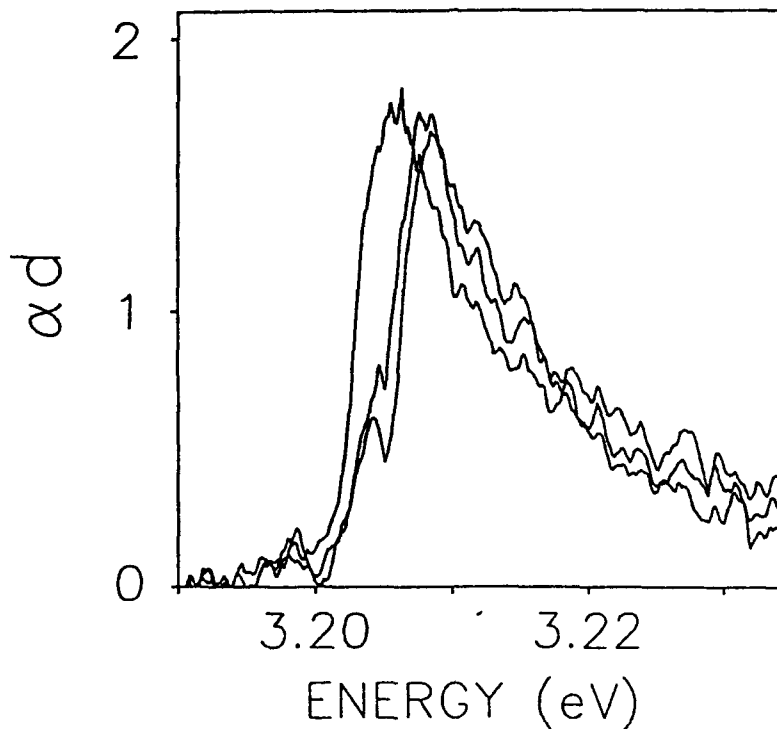


Figure 1: Holeburning observed in test and pump experiments in a sample of  $R = 50\text{\AA}$  mean radius at different excitation intensities.

down to pumped liquid helium temperature ( $2K$ ). As discussed in detail in Ref. 13 and 15, the transmission spectra depend strongly on the samples (on the mean radius of nanocrystallites they contain) and on the excitation intensity. For samples containing large nanocrystallites, the absorption bleaches below the photon energies of the exciting pump beam and increases at higher photon energies. These effects are due to exciton-exciton interactions and to the Fermion character of the quasiparticles building up the excitons <sup>7,8</sup>. Through the excitation, the pump beam fills the 1-exciton states in the nanocrystallites, and the test beam monitors the transition from the 1-exciton to the 2-exciton states. It is blue shifted because of the Pauli principle. As shown in Fig.1, for low excitation intensities, even a holeburning at the photon energy of the pump beam can be observed through the test beam. It takes place in samples containing nanocrystallites with small mean radius  $R$ , where the size distribution leads to a strong inhomogeneous broadening of the  $Z_3$  resonance. In this case, the pump pulses may selectively saturate excitons in nanocrystallites with a given size and bleach only their absorption. The homogeneous linewidth thus measured ( $< 0.5meV$ ) is comparable to that of the bulk material ( $0.1meV$ ).

Performing these measurements time resolved <sup>15,17</sup>, the bleaching as well as the absorption increase show two time constants of about 1 and 10 ns, respectively. The shorter time constant is attributed to the exciton lifetime in the nanocrystals, the second is probably due to the heating of the sample

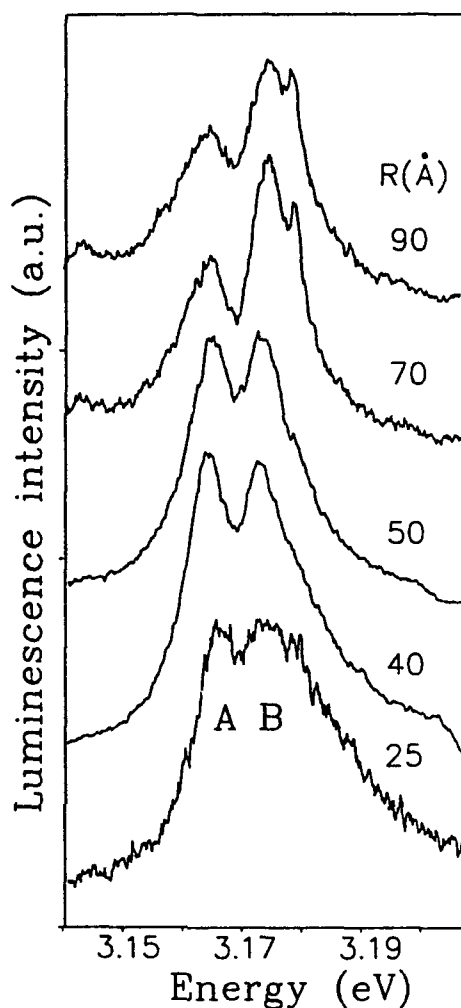


Figure 2: Biexciton luminescence of CuCl nanocrystallite samples of different mean radius  $R$ .

immersed in liquid helium. The optical nonlinearity,  $\chi^{(3)}$ , is slightly depending on the mean crystallite radius<sup>17,18</sup>  $R$ , showing a maximum around  $50\text{\AA}$ . the exciton lifetime is comparable with that of bulk material<sup>10</sup>. The absolute values of  $\chi^{(3)}$  cannot be compared between bulk material and quantum dots, since in nanocrystals excitons are excited resonantly. In bulk material, only a nonresonant excitation is possible since the material is no longer transparent at the exciton resonance.

## 2.2. Biexciton luminescence and gain experiments.

As discussed in the introduction, two excitons may couple to form biexcitons. They recombine radiatively and create an exciton. The excess energy is emitted as a photon. Fig.2 shows the emission spectra at  $8K$  of samples<sup>19</sup> containing quantum dots of different mean radii  $R$ . The samples are excited

by pulses of the third harmonic of a modelocked Nd:YAG laser (3.5eV) of 35 ps duration, giving rise to a band-to-band excitation. The emission studied is situated around a photon energy of 3.17eV, i.e. below the  $Z_3$  absorption band.

An emission line located at 3.178eV is observed at a fixed spectral position, independent of the mean radii of the quantum dots. As in bulk material, this so-called  $\nu_2$ -line is attributed to<sup>16</sup> the recombination of an exciton bound to a neutral acceptor<sup>20</sup> which, in this case, is a copper vacancy. This line is spectrally narrow and its position independent of the crystallite size. This indicates that the spatial extension of this bound exciton complex is very small since it should show a size effect otherwise.

Two additional emission bands, labeled A and B in Fig. 2, are also observed. From its spectral position, its dependence on the excitation intensity, and its excitation spectrum (which shows maxima at the exciton- and at half the biexciton energies), the A-line at 3.164eV could be identified as the radiative recombination of biexciton towards exciton states<sup>16</sup>. It is important for this identification to calculate the exciton- and biexciton energies in large nanocrystallites from their values in bulk material, taking into account only the short range exchange interaction. The long range part is absent because of the lack of translational invariance. The exciton state with  $\Gamma_5$  symmetry remains degenerated.

Fig.2 shows that the difference between biexciton- and exciton energies is independent of the size of the quantum dots, although the exciton energy increases by about 20meV when  $r$  decreases from 90 to 25 Å. The biexciton binding energy  $E_{bi}^b$  can be expressed in terms of the position  $E_A$  of the A-line through :

$$E_{bi}^b = 2E_{ex} - E_{bi} = E_{ex} - E_A$$

where  $E_{bi}$  denotes the biexciton energy. This indicates that the biexciton binding energy increases with decreasing radii of quantum dots. This is in agreement with theoretical predictions<sup>21-23</sup> and cannot be explained in the frame of the simple model in which biexcitons are just confined inside the quantum dot, leading to a quantification of the kinetic energy only, without changing the biexciton wave function.

When analyzing the lineshape of the A-line in detail<sup>16</sup>, we also find that, independently of the photon energy or the intensity of excitation, the initial state of recombination is always the biexciton ground state. Recombination from higher (rotational) states would lead to a blue shift of the emission which has not been observed.

Concerning the origin of the B-line, centered at 3.173eV, it slightly shifts to lower energies when decreasing the dot radius. Its dynamics follows that of A-line<sup>19</sup>, but the excitation spectrum is quite different<sup>16</sup>. Since it is absent if a NaCl matrix instead of borosilicate glass is used, we believe that it involves exciton surface states of the dots.

When using a test and pump configuration and exciting at 3.5eV with an intensity of 25MW/cm<sup>2</sup>, optical gain is observed in the spectral region of Fig.2. Exceeding this excitation intensity, the samples are damaged irreversibly. As shown in Fig.3, a maximum gain of  $G = 12\text{cm}^{-1}$  is observed with a sample of  $R = 50\text{Å}$ . The spectral shape of the gain follows closely that of the A- and B-bands. In time resolved experiments, a double exponential decay with time constants of 160 ps and 6 ns is found for both, the

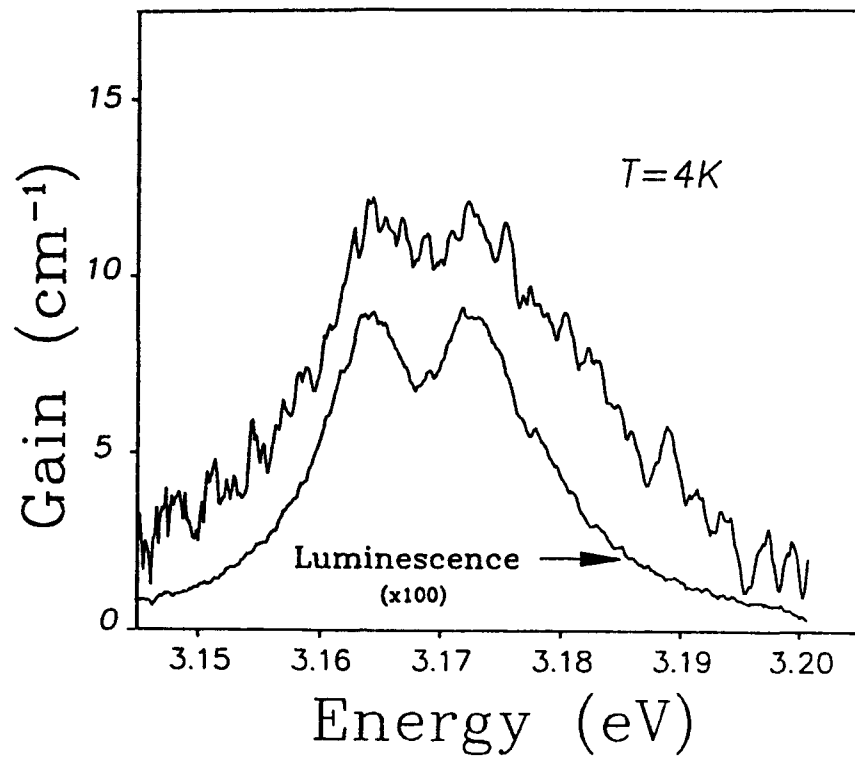


Figure 3: Optical gain spectrum (full line) and luminescence (dotted line) of CuCl nanocrystallites with  $R = 50 \text{ \AA}$ .

A- and B-band. Because of stimulated emission processes involved, these time constants are not directly related to exciton- or biexciton lifetimes in the quantum dots.

### 2.3. Light induced grating spectroscopy.

In order to determine the coherence time  $T_2$  (and the energy lifetime  $T_1$  with a higher precision than discussed in 2.1), we have performed light-induced grating (LIG) and energy transfer measurements<sup>24,25</sup>. In LIG experiments, we use the emission of a tunable dye laser with pulses of 20 ps duration. This emission is split into two beams, which excite the sample in spatial coincidence in a spot of about  $150 \mu\text{m}$  diameter. Both beams of equal intensities interfere on the surface of the sample, creating a spatially modulated intensity. It gives rise to modulations of the absorption of the sample and of its refractive index. These modulations act as a transient grating, on which both beams can be self-diffracted. A second process is also possible. A two photon-absorption followed by a recombination induced by the test beam. The signals thus generated are emitted in the same direction but have different temporal behaviours<sup>25</sup>. If one delays the pulses of one beam with respect to the pulses of the other beam, one changes the modulation of the grating since it depends on the coherence time of the material  $T_2$ . Therefore, the measurement of the intensities of the different orders of diffraction as function of the time delay is

a good tool to determine  $T_2$ . It is a background-free spectroscopy which can be used even if the signal intensity varies over several orders of magnitude. In order to obtain a good signal to noise ratio, one spatially filters the signal and may thus almost eliminate the stray light from the exciting beams.

When we perform this type of experiments at the exciton resonance, the signal is very weak and its intensity has the shape of the laser auto-correlation function<sup>27</sup>, indicating that  $T_2$  is less than 3 ps. This is the limit of the time resolution of our setup. It corresponds, however, to an exciton coherence time  $T_2$  of about 1 ps, estimated from the holeburning experiments discussed in 2.1.

Because of the difficulties to obtain an important signal with thin samples (which have to be used since the Bragg condition is not fulfilled in degenerate LIG measurements), we have rather studied the energy transfer between two degenerated beams. In this case, the same setup as above is used, but one beam is strongly attenuated with respect to the other one (in our case by a factor of 100). Then, we measure the intensity of the transmitted (test) beam as function of the time delay between the two exciting pulses. Its intensity changes in the presence of the pump beam due to two effects. As discussed above, both beams interfere, creating a grating which diffracts the pump beam into the direction of the test beam. Compared to the LIG experiment discussed above, the Bragg condition is fulfilled here<sup>25</sup>, and samples of important thicknesses (several mm) can be used. This process gives information on the coherence time  $T_2$  of the states involved. In addition, as discussed in 2.1, the pump beam bleaches the absorption (holeburning) of the sample and the time delayed test beam is transmitted with a higher intensity<sup>25</sup> than without excitation. This process gives information on the energy relaxation time  $T_1$  of the excitons.

Fig.4 shows the time-resolved sample transmission when deconvoluted with the different processes. Concerning the coherent part, we notice that induced recombination is more efficient than the light induced grating contribution. This is due to the low modulation of the complex index of refraction achieved in this experiment. The coherence time of 17 ps obtained is that of the state excited by two-photon absorption, not the exciton coherence time. The bleaching time constant is  $T_1 = 2$  ns.

### 3. CONCLUSION

We have discussed the dynamical nonlinear optical properties of CuCl nanocrystallites in a borosilicate matrix. From holeburning and light-induced grating measurements, we have determined the exciton coherence time to be about 1 ps, comparable to bulk material. The coherence time of states excited by two-photon absorption (17 ps) is also comparable to those of biexcitons in bulk material<sup>10</sup> (25-40 ps). Only the energy life time  $T_1$  of nanocrystallites (2 ns) is longer than that of excitons in bulk material<sup>10</sup> (250 ps). Thermal effects with a time constant of 6 to 10 ns have been observed here compared to 4 ns in bulk material. This difference is probably due to the bad thermal conductivity of the glass matrix. Biexcitons exist in nanocrystallites as in bulk material and have the same high transition probability. In quantum dots, their binding energy increases with decreasing crystallite radius. Biexcitons may be created by two-photon absorption as well as by coupling of two excitons. While they recombine into excitons and photons from a given distribution in bulk material, obeying to energy and momentum conservation, they mainly recombine in nanocrystallites from the biexciton ground state. The nonlinear optical susceptibility is size dependent, showing a maximum<sup>18</sup> around 50 Å. The main advantage of quantum dots compared to bulk material is the fact that one may work close to the maximum value of the optical nonlinearity, i.e. close to the exciton resonance. In this spectral region, saturation intensities of about  $100 \text{ kW/cm}^2$



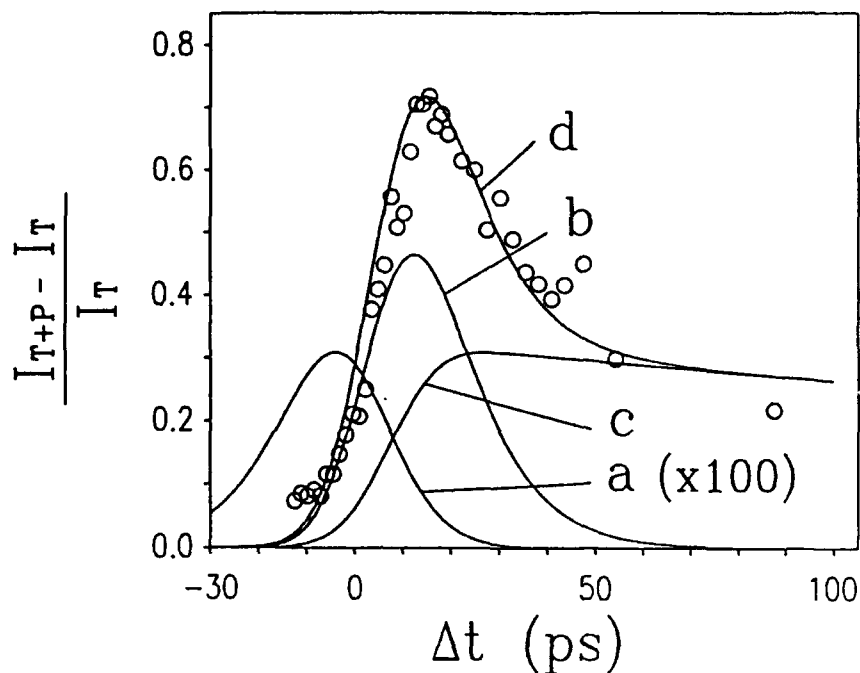


Figure 4: Transmission of the test beam in function of time delay in an energy transfer experiment. a) LIG contribution, b) induced recombination, c) bleaching, d) sum of a) to c).

have been found under nanosecond excitation conditions. The exciton absorption line is inhomogeneously broadened in samples containing quantum dots due to their size distribution and to fluctuations of the surrounding matrix.

In conclusion, the optical nonlinear properties of CuCl nanocrystallites can be globally understood from the bulk parameters if the excitation intensity is kept low enough in order not to damage the system. This situation is very different from nanocrystallites made of materials in which the exciton binding energy is small and the elementary excitations are strongly confined<sup>28,29</sup>.

#### ACKNOWLEDGMENTS

The authors gratefully acknowledge helpful discussions with Drs P. Faller, P. Gilliot, and J. B. Grun.

#### References

- [1] E. Hanamura. *Phys. Rev. B* 37 (1988) 1273.
- [2] S. Schmitt-Rink, D.A.B. Miller, and D.S. Chemla. *Phys. Rev. B* 35 (1987) 8113.

- [3] D.S. Chemla and D.A.B. Miller. *Opt. Lett.* 11 (1986) 522.
- [4] K.C. Rustagi and C. Flytzanis. *Opt. Lett.* 9 (1984) 344.
- [5] A.L. Efros and A.L. Efros. *Sov. Phys. Semicond.* 16(7) (1982) 772.
- [6] L. Banyai and S.W. Koch. *Atomic, Molecular and Optical Physics 2 : Semiconductors Quantum Dots*. World Scientific Publishing, Singapore, 1993.
- [7] L. Belleguie, L. Banyai, and B. Hönerlage. *Ann. Phys. (Paris)* 16 (1991) 55.
- [8] L. Belleguie and L. Banyai. *Phys. Rev. B* 44 (1991) 8755.
- [9] B. Hönerlage, R. Lévy, J.B. Grun, C. Klingshirn, and K. Bohnert. *Phys. Rep.* 124 (1985) 161.
- [10] M.J.M. Gomes, B. Kippelen, B. Hönerlage, R. Lévy, and J.B. Grun. *J. Lumin.* 46 (1990) 319.
- [11] B. Hönerlage, R. Lévy, and J.B. Grun. *Progress of Electron Properties of Solids*. Kluwer Academic Press, Amsterdam, p.275, 1989.
- [12] A.I. Ekimov, A.L. Efros, and A.A. Onushchenko. *Sol. Stat. Commun.* 56 (1985) 921.
- [13] P. Gilliot, J.C. Merle, R. Lévy, M. Robino, and B. Hönerlage. *Phys. Stat. Sol. (b)* 153 (1989) 403.
- [14] I.M. Lifshitz and V.V. Slezov. *Sov. Phys. JEPT* 8 (1958) 331.
- [15] P. Gilliot, B. Hönerlage, R. Lévy, and J.B. Grun. *Phys. Stat. Sol. (b)* 159 (1990) 259.
- [16] R. Lévy, L. Mager, P. Gilliot, and B. Hönerlage. *Phys. Rev. B* 44 (1991) 11286.
- [17] B. Kippelen, L. Belleguie, P. Faller, P. Gilliot, J.B. Grun, B. Hönerlage, and R. Lévy. Optics of excitons in confined systems. *Proc. Int. Conf. Nazos* (1991) 171.
- [18] A. Nakamura, T. Tokizaki, H. Akiyama, and T. Kataoka. *J. Lumin.* 53 (1992) 105.
- [19] P. Faller, B. Kippelen, B. Hönerlage, and R. Lévy. *Opt. Materials*. 2 (1993) 39.
- [20] M. Certier, C. Wecker, and S. Nikitine. *J. Phys. Chem. Sol.* 30 (1968) 1281.
- [21] L. Banyai. *Phys. Rev. B* 39 (1989) 8022.
- [22] Y.Z. Hu, M. Lindberg, and S.W. Koch. *Phys. Rev. B* 42 (1990) 1713.
- [23] T. Takagahara. *Phys. Rev. B* 39 (1989) 10206.
- [24] P. Faller, V. Netiksis, R. Lévy, and J.B. Grun. *Nonlin. Optics* 5 (1993) 191.
- [25] P. Faller, V. Netiksis, R. Lévy, and B. Hönerlage. *J. Appl. Phys.* (1993) to be published.
- [26] H.J. Eichler, P. Günter, and D.W. Pohl. *Laser-Induced Dynamic Gratings*. Springer Series in Optical Sciences, Vol. 50, Springer-Verlag, Berlin, 1986.
- [27] P. Gilliot. *Private communication*.
- [28] P. Roussignol, D. Ricard, Ch. Flytzanis, and N. Neuroth. *Proc. SPIE* 1127 (1989) 109.
- [29] D. Ricard, P. Roussignol, F. Hache, and Ch. Flytzanis. *Phys. Stat. Sol. (b)* 159 (1990) 275.

## Novel technique for porous Si films preparation.

V.I.Beklemishev, V.M.Gontar, V.V.Levenets\*, and I.I.Makhonin  
Department of Materials Science, Research Institute of Physical  
Problems, Russia, 103460, Moscow, Zelenograd.

\*Chemical Vapor Deposition Laboratory, High Purity Materials  
Institute, Russia, 103575, Moscow, K-575, Panfilova, D.15 "A"

### ABSTRACT.

Nucleous layer of amorphous silicon has been used for chemically etched porous Si preparation in solution HF:H<sub>2</sub>O (HF:HNO<sub>3</sub>:H<sub>2</sub>O). This effect has been utilized to produce selective-area photoemission in porous Si with submicrometer resolution for the first time. This technique can be easily incorporated into conventional semiconductor fabrication technology.

### 1. INTRODUCTION.

Since the recent discovery of visible luminescence from porous silicon, a large number of papers have been published, mainly discussing possible mechanisms interpreting this observation, as well as dealing with the morphology, degradation, and methods of fabrication of porous Si. However, luminescence mechanism and microstructure of porous silicon are still not clear.

Some of the articles have stated that porous Si has a wirelike structure and that the luminescence is due to two-dimensional carrier confinement<sup>1-4</sup>. There is report states that porous Si has particlelike structure and that the luminescence is due to three-dimensional carrier confinement<sup>5</sup>. Another mechanisms proposed

for interpretation of Si-based luminescence are: hydrogen passivation of the dangling Si bonds involving silicon monohydride (SiH) and silicon dihydride (SiH<sub>2</sub>)<sup>6,7</sup>, molecular chemisorption and subsequent luminescence of fluorine<sup>4,8</sup>, luminescence from siloxene (Si<sub>6</sub>O<sub>3</sub>H<sub>6</sub>)<sup>9</sup> or involvement of amorphous Si<sup>10,11</sup>.

Porous Si on silicon wafers are generally produced by electrochemical (anodic) etching of p-type Si in hydrofluoric acid, often followed by an immersion in aqueous HF<sup>3</sup> or HF vapor phase etching<sup>12</sup>. It has been shown that luminescent porous Si can be produced by photoelectrochemical<sup>13</sup> and spark-erosion technique<sup>14</sup>. But chemical (stained) etching technique for porous Si preparation takes advantage because of its simplicity. Some investigations have utilized simple etching of Si in solutions of HNO<sub>3</sub> in HF, NaNO<sub>2</sub> in HF, or CrO<sub>3</sub> in HF and have produced this way stained films which structures are similar anodic porous Si structures<sup>15-17</sup>.

## 2. SAMPLE PREPARATION, MEASUREMENTS, AND MAIN RESULTS.

This paper reports an alternate technique for obtaining chemically etched porous Si (CPoSi). We have used p-type (100)Si wafers (B-doped) with resistivity ranging from 0.1 to 20 Ω-cm. The nucleus layer has to be done for fabricating porous Si film. Ion implantation (Si, Cl, and F fluxes, 100kV with a dose of 10<sup>15</sup>/cm<sup>2</sup>) was being used for amorphous layers preparation. Then samples were etched in solution H<sub>2</sub>O: HF or HF: HNO<sub>3</sub>: H<sub>2</sub>O. (Chemicals used in this work were commercial reagents guaranteed as: HF (49%), HNO<sub>3</sub> (70%) - electronic grade; deionized water -18 MΩ-cm.) Etching time ranging to 24 hours. Then samples were rinsed with deionized water, dried with nitrogen.

We have not found out significant distinctions between the porous Si films formed on the different types of Si wafers because of these wafers have not strong difference in the doping degree. Porous Si films prepared under different conditions: ion implantation fluxes, etching time, etching solutions had thicknesses ranging to 2  $\mu\text{m}$  and shown stable photoluminescence (PL) (wavelength ranging from 600 to 800 nm, quantum efficiency - 0.5%) at room temperature under the excitation of an Ar<sup>+</sup> laser

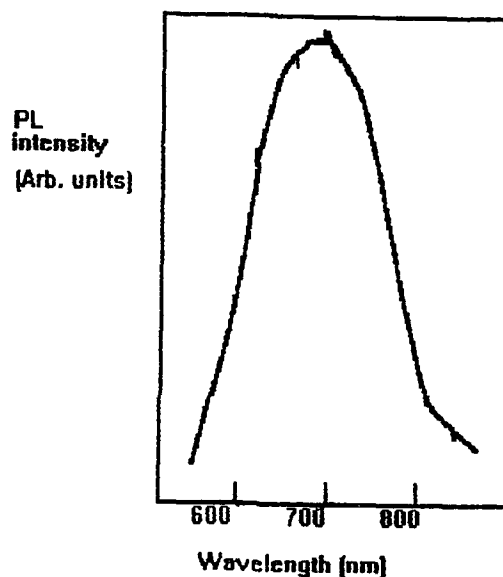


Fig. 1. PL spectra from sample etched in solution of H<sub>2</sub>O: HF for 2 hours after implantation at 100kV with a dose of  $10^{15}$  Si<sup>+</sup>/cm<sup>2</sup>.

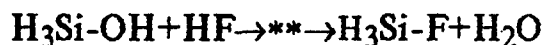
( $\lambda=514$  nm). Figure 1 shows the typical PL spectra from sample etched in solution of H<sub>2</sub>O: HF for 2 hours after implantation at 100kV with a dose of  $10^{15}$  Si<sup>+</sup>/cm<sup>2</sup>. The PL peak wavelengths shifted to a lower wavelength whenever the etching time is increased.

TEM analysis reveals that all process of CPoSi formation consists of two stages characterized by two different etching rates. The first stage etching rate is less than the second stage one. CPoSi film has sliced structure, and the pores are highly directional and propagate in the [100] direction within every slice. We haven't found a random collection of smaller pores extending out from the surface of the larger pores as been reported in the work<sup>18</sup>. However, micropores, not resolved by the TEM, may still be additionally present.

### 3. DISCUSSIONS.

CPoSi formation in 49%HF is an example of anisotropic etching of crystalline Si in aqueous HF solution. This process consists of two stages. The first stage deals with amorphous layer reorder. The nucleus centres are formed during the first stage in amorphous layer, and pores propagation starts in these nucleus centres. In the second stage, pores growth takes place due to anisotropic etching of crystal Si.

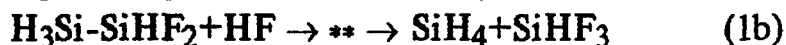
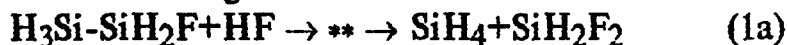
It is well known that mechanism of oxide removal in HF:H<sub>2</sub>O solution leads to F termination of the Si surface<sup>19</sup>. For the model reaction<sup>20</sup>



calculated activation barrier is equal 0.55 eV. (All spectator bonds are replaced by hydrogen; \*\* is a sign of the transition state. The activation barrier of the reaction is the difference between the total energy of the transition state and the sum of the ground-state energies of the reactants.) This extremely low activation barrier guarantees that the first step of HF acid etching of Si begins on a fluorine-terminated surface. But such fluorine-terminated surfaces are not stable and subject to further HF attack.

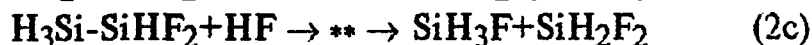
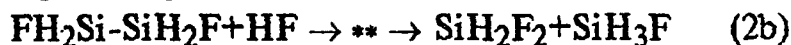
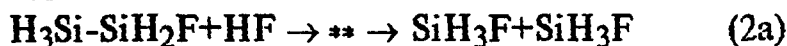
In examining further HF attack, two orientations of HF insertion into Si-Si bonds are possible. In the first, the F from HF attaches to the surface Si and H attaches to the underlying Si leaving behind a H-terminated surface. The other possible HF attack is with the HF oriented such that the hydrogen bonds with the surface silicon. This reaction leaves a F-terminated surface. Another words, this leaves the same morphology as befor; therefore, if this orientation were favorable, it would result in a continuous etch. Thus, the final surface state depends on the selectivity of HF attack on Si-Si bonds after the initial oxide removal.

The reactions leading to H termination are modeled as



Activation barrier for all these reactions equals 1.0 eV, and these reactions are also thermodynamically favorable (exothermic by 1.8-2.0 eV). This mechanism ultimately results in removal of Si as SiF<sub>4</sub>.

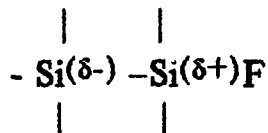
The analogous reactions which would lead to F termination are modeled as



These reactions are somewhat less exothermic ( $\approx 1.6$  eV), and they have activation barriers of 1.4 eV which are 0.4 eV higher than reaction (1). This comparatively large activation barrier ensures that this reaction can be ignored.

The reason for preferential attack of HF at F-Si-Si sites is

due to induced polarization of the Si-Si bonds<sup>21</sup>.



Additional contribution to the activation barriers gives lattice constraints. This contribution (e.g., by maintaining a tetrahedral Si-Si-Si bond angle) was found to be very small ( $\approx 0.02$  eV). But when we discuss mechanism of CPoSi formation (in HF:H<sub>2</sub>O solution) it has to be taken into account another contribution in the activation barriers due to strain of pores surface. The distribution of surface strain is sensitive to pore geometry, and its maximum occurs at the tip of an elliptical pore. In this point due to high strain of pores surface activation barriers for reactions (2) are less than activation barriers for reactions (1). Hence, continuous etch with the surface Si being removed as either SiH<sub>3</sub>F, SiH<sub>2</sub>F<sub>2</sub> or SiHF<sub>3</sub> takes place at the tip of pore.

#### 4. CONCLUSIONS.

In summary, we have used nucleous layer of amorphous silicon for chemically etched porous Si preparation in solution HF:H<sub>2</sub>O (HF:HNO<sub>3</sub>:H<sub>2</sub>O). This effect has been utilized to produce selective-area photoemission in porous Si with submicrometer resolution for the first time. This technique can be easily incorporated into conventional semiconductor fabrication technology. Process of porous Si growth can be divided into two stages characterized by two different etching rates. Anisotropic Si etching in aqueous HF solution takes place at the tip of pore due to high strain of pores surface.



## REFERENCES

1. H. Koyama, M. Araki, Y. Yamamoto and N. Koshida, Jpn. J. Appl. Phys., 30, 254 (1991)
2. J. M. Zhu, O. Li, L. C. Wang and H. P. Xu, J. Phys.: Condens. Matter, 5, L157 (1993)
3. L. T. Canham, Appl. Phys. Lett., 57, 1046 (1990)
4. Z. Y. Xu and M. Gross, Appl. Phys. Lett., 60, 1375 (1992)
5. A. Nishida, K. Nakagawa, H. Kakibayashi and T. Shimada, Jpn. J. Appl. Phys., 31, L1219 (1992)
6. M. A. Tischler, R. T. Collins, J. H. Stathis and J. C. Tsang, Appl. Phys. Lett., 60, 639 (1992)
7. C. Tsai, K. -H. Li, J. Sarathy, S. Shih and J. C. Campbell, Appl. Phys. Lett., 59, 2814 (1991)
8. E. Corcoran, Sci. Am., 266, 102 (1992)
9. H. D. Fuchs, M. S. Brandt, M. Stutzmann and J. Weber, Mater. Res. Soc. Symp. Proc., 256, 159 (1992)
10. R. P. Vasquez, R. W. Fathauer, T. George, A. Ksendzove and T. L. Lin, Appl. Phys. Lett., 60, 1004 (1992)
11. C. Pickering, M. I. J. Beale, D. J. Robb, P. J. Pearson and R. Greef, J. Phys., C17, 6535 (1984)
12. S. Shih, K. H. Jung, D. L. Kwong, M. Kovar and J. M. White, Appl. Phys. Lett., 62, 1904 (1993)
13. V. V. Doan, R. M. Penner and M. J. Sailor, J. Phys. Chem., 97, 4505 (1993)
14. R. E. Hummel and Sung-Sik Chang, Appl. Phys. Lett., 61, 1965 (1992)
15. J. Sarathy, S. Shih, K. Jung, C. Tsai, K.-H. Li, D.-L. Kwong, J. C. Campbell, S.-L. Yau and A. J. Bard, Appl. Phys. Lett., 60, 1532 (1992)
16. R. Herino, G. Bomchil, K. Barla, C. Bertrand and J. L. Ginoux, J. Electrochem. Soc., 134, 1994 (1987)

17. R. W. Fathauer, T. George, A. Ksendzov and R. P. Vasquez, Appl. Phys. Lett., 60, 995 (1992)
18. S.-F. Chuang, S. D. Collins and R. L. Smith, Appl. Phys. Lett., 55, 1540 (1989)
19. J. S. Judge, J. Electrochem. Soc., 118, 1772 (1971)
20. G. W. Trucks, Krishnan Raghavachari, G. S. Higashi and Y. J. Chabal, Phys. Rev. Lett., 65, 504 (1990)
21. H. Ubara, T. Imura and A. Hiraki, Solid State Commun., 50, 673 (1984)

## Near infrared laser production of fullerenes

L. Láška, J. Krása, L. Juha, V. Hamplová and L. Soukup

Institute of Physics, Academy of Sciences of the Czech Republic  
Na Slovance 2, 180 40 Praha 8, Czech Republic

### ABSTRACT

We performed graphite vaporization by an iodine photodissociation laser and obtained  $C_{60}$  as the first by IR laser. We obtained sufficient macroscopic amount of fullerene, which enabled us to apply solvent extraction method and UV spectrophotometry.

### 2. INTRODUCTION

Laser vaporization of different solid targets is a commonly used technique for many purposes. Considering wide spectrum of these possibilities we remember at least two of them: deposition of high quality thin films and production of metallic or carbon clusters. The effectiveness and quality of results are conditioned by the wavelength and energy of laser, power density, local temperature of the target as well as surrounding atmosphere and by other experimental details.

The study of cluster species is of wide-spread interest in recent years. In particular, carbon clusters have been the focus of intensive experimental and theoretical research, reviewed e.g. in<sup>1,2</sup>. The first technique used to produce them involved the vaporization of carbon species from a surface of graphite target by the second harmonics of Nd:YAG pulsed laser either inside a high pressure pulsed supersonic nozzle<sup>3-9</sup> or into vacuum<sup>10,11</sup>. Excimer laser ionization and time-of-flight mass spectrometry were necessary to identify products created in this way.

The laser vaporization of graphite produces clusters whose size ranges from two atoms to several hundreds atoms<sup>3</sup> and the shape of which may be linear, planar or spheroidal. Main attention is devoted to those even-numbered and greater than 32 atoms in size and especially to extremely stable  $C_{60}$  with a unique structure - truncated icosahedron - formed by <sup>60</sup> twelve pentagons and twenty hexagons. These quasi-spherical molecules, named in 1985 by Kroto et al.<sup>4</sup> "buckminsterfullerenes", constitute the third and simultaneously the purest form of carbon, in addition to graphite and diamond structure. However, only the new production method with much greater effectiveness, based on an arc discharge evaporation of graphite

electrodes and presented by Kratschmer et al.<sup>12</sup> in 1990, yielded macroscopic amount of this substance. It was possible to extract fullerenes from the produced soot by chemical way and to indicate them by mass spectrometry, UV-VIS spectrometry, IR spectrometry or even to see them directly in microscope. Since that time the avalanche of studies has started, supposing to find new and unexpected properties of fullerenes and their compounds.

The question arose, why the laser technique was not successful as the latter one. According to Curl and Smalley<sup>13</sup> C<sub>60</sub> appears to result inevitably when carbon condenses slowly enough<sup>60</sup> and at high enough temperature. From the previous experiments it was possible to summarize:

1. Nd:YAG laser operating at  $\lambda = 532$  nm (second harmonics) and with pulse length from 5 ns to about 25 ns was used for vaporization in all experiments; the power density was mostly above  $10^8$  W/cm<sup>2</sup>.
2. Excimer lasers were used for fullerene (soot) desorption and ionization.
3. The reactions in flowing helium occurred at different temperatures over a contact time of 100 - 500  $\mu$ s<sup>5-7</sup>.
4. Varying the length of the nozzle extender channel - with longer extender, larger clusters as well as C<sub>60</sub> are produced much easier<sup>3,4,8</sup>.
5. In another experiment Haufler et al.<sup>14</sup> explored the effect of wall temperature on fullerene yields by laser vaporization: only when the walls of the tube were heated above 1000°C, any fullerenes were obtained.
6. With only one exception<sup>10</sup> the target was rotated or translated to expose a constantly fresh surface.
7. Complete decomposition of fullerenes was carried out with an ultra-violet lamp under 10 - 16 hour exposures<sup>15</sup>.

Analyzing the above information, we suggested and tested NIR iodine laser as a more advantageous for this purposes<sup>16</sup>. A further study is presented here.

### 3. EXPERIMENT

The experimental setup of the deposition reactor is sketched in Fig.1. A3 amplifier of high power photodissociation iodine laser system PERUN<sup>17</sup>, working in an oscillator regime, was used for this purposes. It operates at  $\lambda = 1.315$   $\mu$ m with a pulse energy of about 25 J, with a pulse length of 150  $\mu$ s and at a repetition frequency of 1 pulse per 3 minutes. The laser beam was focused by the lens with  $f = 50$  cm on the fixed graphite target. The evaporated carbon was deposited on the inner surface of a cylindrical glass collector in a static helium atmosphere of varying pressures. A set of experiments with 100 shots to the same spot of 1 mm in diameter was performed at helium pressures 2, 12.5, 25 and 65 kPa. After these 100 shots approximately

2 mm deep hole appeared.

In contrast to the previous laser vaporization experiments<sup>3-11</sup> we obtained on the collector wall soot with a macroscopic amount of fullerenes, sufficient to apply chemical extraction method and UV absorption spectroscopy for its determination<sup>2,18-21</sup>. Extraction was performed in a Soxhlet reactor<sup>20</sup>, where C<sub>60</sub> was extracted in 250 ml redistilled hot HCCl<sub>3</sub> for 4 hours. After<sup>60</sup> that the solution was evaporated in vacuum, the residual solid extract was dried and finally dissolved in 3 ml n-hexane. We registered the presence of most pronounced absorption peak of C<sub>60</sub> in n-hexane solution at 257 nm in all cases. Contaminations by<sup>60</sup> "UV impurities" complicate the evaluation of these spectra. The peak of C<sub>60</sub> at 213 nm may, e.g., be covered by the band, corresponding to the<sup>60</sup> traces of trichlormethan, which cannot be completely removed. We found the largest amount of C<sub>60</sub> at 12.5 kPa of He (Fig. 2, curve 2). It is worth mentioning that after a period about 1 month the 257 nm absorption band was missing (Fig. 2, curve 3). This fact confirms the idea of Taylor et al.<sup>15</sup> about possibility of C<sub>60</sub> degradation by light. The reference experiment was performed too, in<sup>60</sup> which 0.5 g of graphite from the unexposed target was extracted; there was no peak at this wavelength in the UV spectrum (Fig. 2, curve 1). UV/VIS spectra of pure C<sub>60</sub> (Aldrich, C<sub>60</sub>/C<sub>70</sub> mixture 10:1) were also measured for comparison<sup>60</sup> (the spectrum of<sup>70</sup> 1.5 x 10<sup>-5</sup> M C<sub>60</sub> n-hexane solution is in Fig. 4, the spectrum of 10<sup>-8</sup> M solution<sup>60</sup> is equivalent to Fig. 2, curve 2).

Another set of experiments was performed with the target, in which the hole of 5 mm in diameter and 5 mm deep was drilled. Moreover, separating the glass collector of about 120 mm height into three parts space distribution of deposit was studied. Toluene was used for extraction of fullerenes (8 hours) in this case after only 50 shots. UV spectrum in Fig. 3 represents the peak at 257 nm of fullerenes obtained on the middle collector at 12.5 kPa He atmosphere. The most yield was indicated not on the collectors, but directly on the target.

#### 4. DISCUSSION

The exact mechanism of fullerene formation as well as the optimum conditions especially for their laser production are not completely known. The experiments by Kratschmer et al.<sup>12</sup> and observations by Haufler et al.<sup>14</sup> can be interpreted as indicating that the processes forming C<sub>60</sub> require elevated temperatures for some time, i.e., involve reactions<sup>60</sup> with substantial activation energies. From the experiments performed up to now it follows that the crucial problems are heating of the target and cooling of the vaporized carbon; both processes should not be too fast<sup>13</sup>.

The range of laser irradiances where evaporation really proceeds stretches from some 10<sup>5</sup> W/cm<sup>2</sup> up to above 10<sup>10</sup> W/cm<sup>2</sup>. The vapor is tenous and transparent below 10<sup>6</sup> W/cm<sup>2</sup>; between roughly 10<sup>7</sup> - 10<sup>10</sup> W/cm<sup>2</sup> - depending on the wavelength - the vapor becomes partially

ionized and absorbs more or less a fraction of the laser energy<sup>22</sup>. At high power densities the vapor is efficiently ionized and the resultant plasma becomes optically dense. The result of further irradiation is an extremely hot plasma with very little further vaporization<sup>23</sup>. However, substantial surface evaporation is determined not only by laser power density, but also by the time of laser interaction with matter. From this point of view the longer pulses ( $10^{-4}$  -  $10^{-5}$  s) are more convenient. The consequence of short intense pulses is fast heating and fast cooling of the target material.

In experiments of O'Keefe et al.<sup>10</sup> it has been noted, that the high-mass cluster ions ( $n > 32$ ) are produced only after a pit is drilled into a stationary graphite substratum by prolonged irradiation. This fact can be explained, as follows: The hole acts as a beam trap in which the laser energy is efficiently absorbed in multiple-reflection effect<sup>22</sup>. It provides simultaneously a confined space, higher particle densities and higher temperature for the plasma, in which clustering occurs, the "channel" produced in this way increases the convenient time of reaction. It corresponds with the "integrating cup" experiments of Kroto et al.<sup>4</sup> and/or with prolonged length of extenders in<sup>3,4,8</sup>.

Differing opinion exist concerning the role of He (or Ar) in cluster formation<sup>3,4,12,13</sup>; in most cases it provides the thermalizing collisions necessary to cool the species in the vaporized graphite plasma. According to<sup>13</sup> it also slows the migration of primary carbon chains away from the target.

Finally, as for the laser wavelength - fast degradation of fullerenes by UV laser radiation was reported recently<sup>24,25</sup>. XeCl excimer laser radiation at 308 nm focused on a quartz cell induced very fast decomposition of fullerenes in n-hexane solution. Fig. 4 shows the UV-VIS absorption spectra of non-irradiated C<sub>60</sub> n-hexane solution and this solution, irradiated by 1500 and 4500<sup>60</sup> laser shots (pulse length was 30 ns, energy 290 mJ and repetition rate 10 Hz). The decomposition rate is most clearly shown by decreasing of C<sub>60</sub> band at 329 nm and C<sub>70</sub> band at 378 nm. This solution was aerated. Similar results gave XeCl laser irradiation of the fullerene solution under helium atmosphere, but results of GC/MS analysis shows different decomposition products under air and under helium. It is most probable that this fast decomposition is connected with multiphoton absorption.

## 5. CONCLUSIONS

The following conclusions can be made from our experiments:

1. Macroscopic amounts of C<sub>60</sub> can be prepared by using the laser vaporization method.
2. Accepting the fact that UV radiation degrades the fullerene

- clusters, the tested IR iodine laser might prove to have an advantage over the excimer ones.
3. Laser pulses in the microsecond scale region and power density lower than  $10^8$  W/cm<sup>2</sup> are more advantageous for the fullerene production.
  4. Carbon evaporation from the hole in the stationary positioned graphite target makes the clustering process much effective.

In spite of a relatively low effectiveness it is worth studying the processes of carbon cluster formation by the laser technique. First - it enables easy to change the experimental conditions in an extremely wide region (laser energy and pulse length, temperature, ambient atmosphere etc.). Secondly - the selectivity of photochemical processes is generally a great advantage of laser chemistry (monoenergetic sources of radiation with tunable wavelength enable atoms or molecules to be excited to any quantum state within energy range about of 0.1 eV to 10 eV), which can be utilized in modification of fullerenes and/or in formation of its compounds.

## 6. REFERENCES

1. M.A. Wilson, L.S.K. Pang, G.D. Willett, K.J. Fisher and I.G. Dance, "Fullerenes - preparation, properties, and carbon chemistry", Carbon, Vol. 30, pp. 675 - 693, 1992.
2. R.F. Curl, "On the formation of the fullerenes", Phil. Trans. R. Soc. Lond. A, Vol. 343, pp. 19 - 31, 1993.
3. E.A. Rohlfing, D.M. Cox and A. Kaldor, "Produktion and characterization of supersonic carbon cluster beams", J. Chem. Phys., Vol. 81, pp. 3322 - 3330, 1984.
4. H.W. Kroto, J.R. Heath, S.C. O'Brien, R.F. Curl and R.E. Smalley, "C<sub>60</sub>: Buckminsterfullerene", Nature, Vol. 318, pp. 162 - 163, 1985.
5. L.A. Bloomfield, M.E. Geusic, R.R. Freeman and W.L. Brown, "Negative and positive cluster ions of carbon and silicon", Chem. Phys. Lett., Vol. 121, pp. 33 - 37, 1985.
6. Q.L. Zhang, S.C. O'Brien, J.R. Heath, Y. Lin, R.F. Curl, H.W. Kroto and R.E. Smalley, "Reactivity of large carbon clusters: spheroidal carbon shells and their possible relevance the formation and morphology of soot", J. Phys. Chem., Vol. 90, pp. 525 - 528, 1986.
7. M.E. Geusic, M.F. Jarrold, T.J. McIlrath, R.R. Freeman and W.L. Brown, "Photodissociation of carbon cluster cation", J. Chem. Phys., Vol. 86, pp. 3862 - 3869, 1987.
8. D.M. Cox, K.C. Reichmann and A. Kaldor, "Carbon clusters revisited: the "special" behavior of C<sub>60</sub> and large carbon clusters", J. Chem. Phys., Vol. 88, pp. 1588 - 1597, 1988.
9. S.C. O'Brien, J. R. Heath, R.F. Curl and R.E. Smalley, "Photo-physics of buckminsterfullerene and other carbon cluster ions", J. Chem. Phys., Vol. 88, pp. 220 - 230, 1988.
10. A. O'Keefe, M.M. Ross and A.P. Baronavski, "Produktion of large carbon cluster ions by laser vaporization", Chem. Phys. Lett., Vol. 130, pp. 17 - 19, 1986.

11. G. Meijer and D.S. Bethune, "Laser deposition of carbon cluster on surface: a new approach to the study of fullerenes", J. Chem. Phys., Vol. 93, pp. 7800 - 7802, 1990.
12. W. Krätschmer, L.D. Lamb, K. Fostiropoulos and D.R. Huffman, "Solid C<sub>60</sub>: a new form of carbon", Nature, Vol. 347, pp. 354 - 358, 1990.
13. R.F. Curl and R.E. Smalley, "Fullerenes", Scientific American, pp. 54 - 63, October 1991.
14. R.E. Haufler et al. "Carbon arc generation of C<sub>60</sub>", Mater. Res. Soc. Proc., Vol. 206, pp. 627 - 638, 1991.
15. R. Taylor, J. P. Parsons, A. G. Avent, S. P. Rannard, T. J. Dennis, J. P. Hare, H. W. Kroto and D. R. M. Walton, "Degradation of C<sub>60</sub> by light", Nature, Vol. 351, pp. 277, 1991.
16. L. Láská, J. Krása, L. Juha, V. Hamplová and L. Soukup, "Production of fullerenes by a near infrared laser", Czech. J. Phys. Vol. 43, pp. 193 - 195, 1993.
17. M. Chvojka, V. Hermoch, B. Králiková, J. Krása, L. Láská, K. Mašek, J. Musil, S. Polák, K. Rohlena, J. Schmiedberger, J. Skála and J. Sulek, "100 GW pulsed iodine photodissociation laser system PERUN I", Czech. J. Phys., Vol. B38, pp. 1337 - 1356, 1988.
18. R Taylor, J.P. Hare, A. Abdul-Sada and H.W. Kroto, "Isolation, separation and characterization of the fullerenes C<sub>60</sub> and C<sub>70</sub>: the third form of carbon", J. Chem Soc., Chem. Commun., Vol. 20, pp. 1423 - 1425, 1990.
19. H. Ajie, M.M. Alvarez, S.J. Anz, R.D. Beck, F. Diederich, K. Fostiropoulos, D.R. Huffman, W. Krätschmer, Y. Rubin, K.E. Shriver, D. Sensharma and R.L. Whetten, "Characterization of the soluble all-carbon molecules C<sub>60</sub> and C<sub>70</sub>" J. Phys. Chem. Vol. 94, pp. 8630 - 8633, 1990.
20. J.P. Hare, H.W. Kroto and R. Taylor, "Preparation and UV-VIS spectra of fullerenes C<sub>60</sub> and C<sub>70</sub>", Chem. Phys. Lett., Vol. 177, pp. 394 - 398, 1991.
21. J.B. Howard, J.T. McKinnon, Y. Marakovsky, A.L. Lafleur and M.E. Johnson, "Fullerenes C<sub>60</sub> and C<sub>70</sub> in flames", Nature, Vol. 352, pp. 139 - 141, 1991.
22. M. von Allmen, "Laser-beam interaction with materials", Springer Series in Material Science 2, Springer Verlag, 1987.
23. T.G. Dieck, M.A. Duncan, D.E. Powers and R.E. Smalley, "Laser production of supersonic metal cluster beams", J. Chem. Phys., Vol. 74, pp. 6511 - 6512, 1981.
24. L. Juha, J. Krása, L. Láská, V. Hamplová, L. Soukup, P. Engst and P. Kubát, "Fast degradation of fullerenes by UV laser radiation", Appl. Phys., Vol. B57, pp. 83 - 84, 1993.
25. L. Juha, J. Krása, L. Láská, V. Hamplová, L. Soukup, P. Engst and P. Kubát, "XeCl excimer laser induced decomposition of fullerenes in solutions", LASERION '93, Munich, 1993, Post-deadline papers, 3.



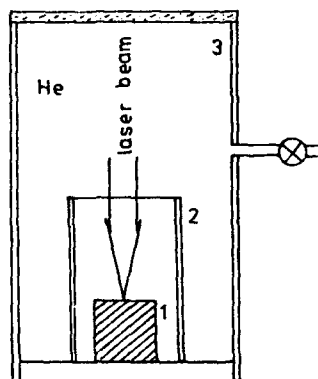


Fig.1. Experimental setup: 1 - graphite target, 2 - glass collector, 3 - experimental chamber.

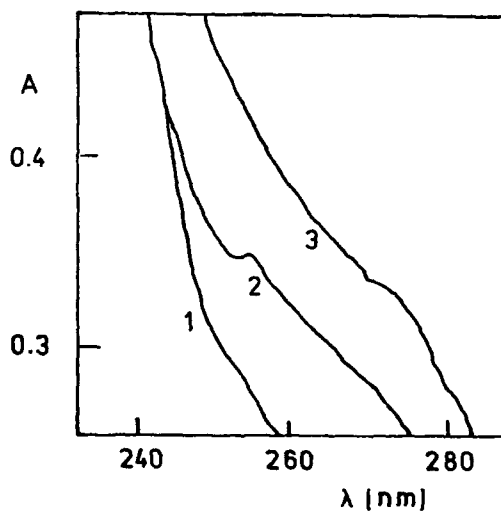


Fig.2. UV absorption spectra of n-hexane solutions of fullerenes: 1 - reference solution of unexposed graphite (diluted 1:10), 2 - solution prepared after  $\text{HCCl}_3$  extraction from the carbon soot sputtered by iodine laser at 12.5 kPa<sup>3</sup> of He atmosphere, 3 - the same solution after 34 days of daylight exposure (the lower transmission is due to evaporation of part of the solvent).

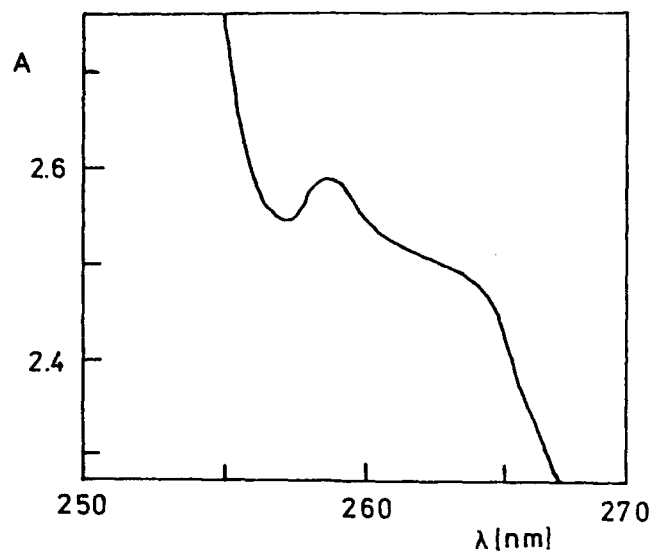


Fig.3. UV absorption spectra of n-hexane solution of fullerene prepared after toluene extraction from the carbon soot sputtered by iodine laser at 12.5 kPa of He atmosphere (target with the hole, middle collector).

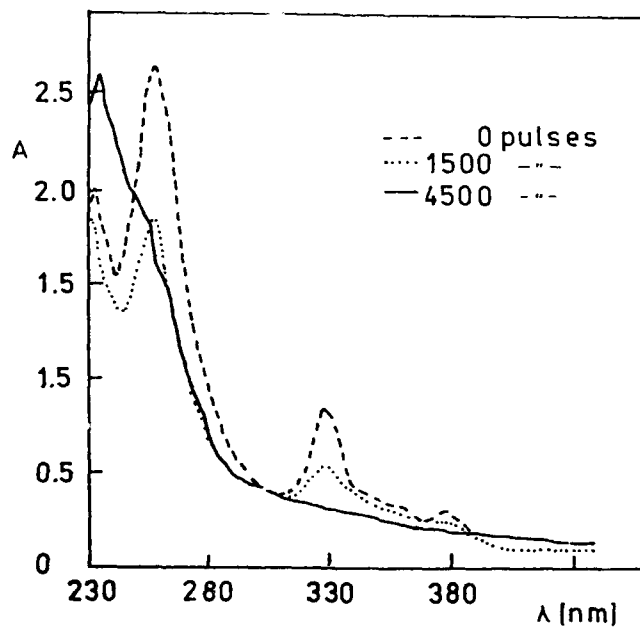


Fig.4. UV-visible absorption spectra of: (a) nonirradiated n-hexane solution of  $C_{60}$  (containing small amount of  $C_{70}$ ) and the same solution irradiated by 1500 (b) and 4500 pulses (c) of XeCl excimer laser.

## Pulsed laser deposition of multilayered structures

M. Jelínek, V. Olšan, V. Trtik

Institute of Physics, Czech Academy of Sciences, Na Slovance 2, 180 40 Prague 8, Czech Republic

### ABSTRACT

Epitaxial superconductive and ferroelectric thin films, buffer layers and multilayers were created by laser ablation deposition on monocrystalline and technological substrates. Deposition of complex multilayer systems composed of YBaCuO, YSZ, ZrO<sub>2</sub>, CeO<sub>2</sub>, SrTiO<sub>3</sub>, PZT, PLZT, and PMN layers, and some properties of these systems characterized by XRD and electrical measurements are presented.

### 1. INTRODUCTION

Pulsed laser deposition (PLD) is based on the fast ablation of target material with following condensation on the substrate. This technique employs a high intensity pulsed laser beam to deliver the energy required to evaporate the target material. This very fast heating results in stoichiometric transfer of multicomponent target material to the deposited film. The advantages of the technique include congruent transfer of target material, a high deposition rate, a lower processing temperature, highly oriented or epitaxially grown films, and in-situ deposition of multilayers. The PLD is an especially useful and powerful method for deposition of complex materials such as superconductors and ferroelectrics. The integration of superconductivity and microwave technology requires the deposition of YBa<sub>2</sub>Cu<sub>3</sub>O<sub>7- $\delta$</sub>  (YBaCuO) superconducting thin films on suitable technological substrates. Such systems have potential applications for transmission lines, resonators, filters, antennas, etc. Sapphire is one of the preferred substrates for technological applications of YBaCuO because of its low dielectric constant, low loss tangent, good mechanical strength and low price<sup>1</sup>. In the direct deposition of YBaCuO on sapphire the layer obtained has poor superconducting properties due to a reaction between the sapphire substrate and the YBaCuO layer and due to a poor lattice match of sapphire to YBaCuO. To avoid this problem, buffer layers are created. As buffer usually the layers of Yttria Stabilized Zirconia (YSZ), ZrO<sub>2</sub>, CeO<sub>2</sub>, or SrTiO<sub>3</sub> are used.

Thin ferroelectric films have attracted much attention for their potential applications including ferroelectric nonvolatile memory, capacitors, optoelectronic, piezoelectric and pyroelectric devices due to their multifunctional properties: polarization switching, a high value of dielectric constant and pyroelectric<sup>2</sup>, piezoelectrical and electrooptical coefficients, etc.<sup>2</sup>. Recent research interest has been focused on the development of a radiation hard nonvolatile memory with the most intensively investigated material Pb(Zr<sub>x</sub>Ti<sub>1-x</sub>)O<sub>3</sub> (PZT). Transparent ferroelectric materials as Pb<sub>1-x</sub>La<sub>x</sub>(Zr<sub>y</sub>Ti<sub>2- $\delta$ (x+y)</sub>)O<sub>3</sub> (PLZT) and PbMg<sub>1/3</sub>Nb<sub>2/3</sub>O<sub>3</sub> (PMN) are interesting for electrooptic devices. Research on optical application is only starting. PLZT thin films in morphotropic phase boundary compositions are studied also for memory devices<sup>3</sup>. The PMN is a typical representative of relaxor ferroelectrics with a diffuse phase transition. This material serves as a model for a physical description of this type of ferroelectrics. Therefore PMN thin films are interesting for fundamental research in theoretical and applied physics. The PMN is a promising dielectric material for future capacitors. The application of ceramic multilayer capacitors is growing quickly because of its large capacitance per volume. PMN thin films are also convenient for use in microactuators.

Thin ferroelectric films have been developed using different methods such as sol-gel, ion-beam sputtering, electron-cyclotron resonance plasma assisted-deposition, metalorganic chemical-vapor deposition and PLD<sup>4</sup>. The PLD, with its considerable success in the growth of high-quality, epitaxial thin films of high temperature superconductors, has been recently used to produce oriented (single crystalline) thin ferroelectric films (PZT, PLZT,  $\text{PbTiO}_3$ ,  $\text{Bi}_4\text{Ti}_3\text{O}_{12}$ ,  $\text{BaTiO}_3$ ,  $\text{LiNbO}_3$ )<sup>5, 6, 7, 8, 9</sup> multilayer heterostructures with superconductors and ferroelectrics. Cuprate superconductor thin films can be used as a base electrode underneath ferroelectric films for electrical measurement, because of the same perovskite structure, the close matching in the lattice constant, and similar thermal expansion coefficients<sup>10</sup> as important ferroelectric materials. Consequently, this yields highly-oriented epitaxial ferroelectric film on top of the high-quality YBaCuO bottom electrode without the problems of interfacial reactions that occur between metal electrodes and ferroelectric films.

In this paper we describe the properties of superconducting and ferroelectric multilayer thin films deposited by PLD. The following films and multilayers were created: YBaCuO on monocrystalline  $\text{SrTiO}_3$  and  $\text{NdGaO}_3$ , YBaCuO on technological substrates as sapphire coated by laser ablated buffer layers of  $\text{ZrO}_2$ , YSZ,  $\text{CeO}_2$ , or  $\text{SrTiO}_3$ , and ferroelectric thin films of PZT(0.52, 0.48), commercial PZT(0.75, 0.25), PLZT(0.09, 0.65, 0.35) and PMN on (100) and (110) $\text{SrTiO}_3$  substrates coated with YBaCuO bottom electrode.

## 2. EXPERIMENTAL

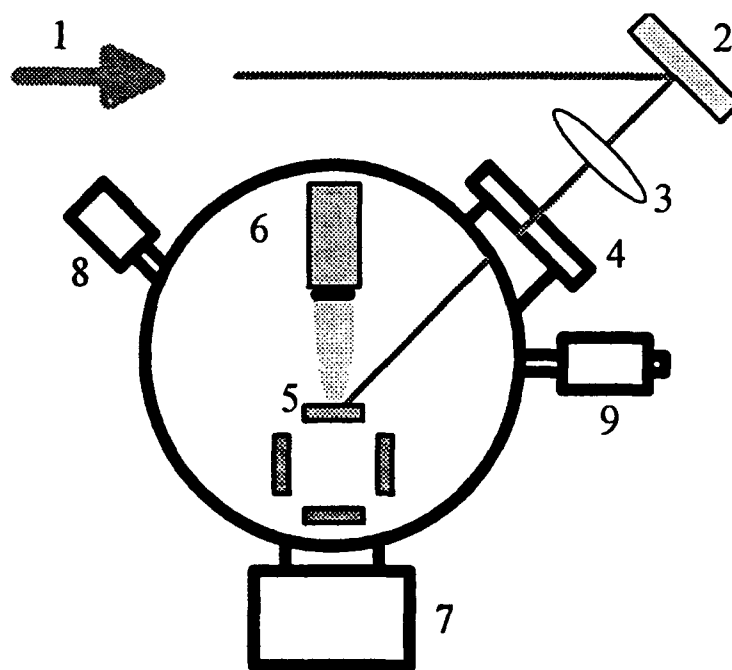


Figure 1. Experimental setup. 1. KrF laser beam ( $\lambda=248$  nm,  $\tau=25$  ns,  $E=200$  mJ), 2. dielectric mirror, 3. focusing lens, 4. fused silica window, 5. targets, 6. heated substrate holder, 7. vacuum pump, 8. vacuum gauge, 9. oxygen filling.

The structures and heterostructures were grown *in situ* using a KrF excimer laser, which was focused onto a rotating, sintered ceramic target of the required material and the resulting plume was caught on heated substrate (see Figure 1). The laser beam energy density was about 2-5 J/cm<sup>2</sup>. The targets were mounted on a four-target moving carousel, thus enabling *in-situ* deposition of multilayered structure. The substrate temperature was measured by a Ni-NiCr thermocouple fixed on the surface of the heater. The substrate heater was maintained at a temperature of 715°C for deposition of the YBaCuO layers<sup>11</sup> and at a temperature in the range from 430°C to 650°C for the ferroelectric layers. The deposition was performed in an ambient of 27 Pa oxygen for YBaCuO and ferroelectric layers. After both the layers are deposited, the heterostructure was cooled down in 1 atm of oxygen. Epitaxial superconductive YBaCuO films were created on monocrystalline substrates as (100)NdGaO<sub>3</sub>, (100) SrTiO<sub>3</sub>, (110) SrTiO<sub>3</sub>, or on technological substrates as (1102) sapphire. On the sapphire substrates the high-quality buffer layers ( ZrO<sub>2</sub>, YSZ, CeO<sub>2</sub>, or SrTiO<sub>3</sub> ) were deposited also by PLD. The overview of created buffer layers and used targets are summarized in Table 1. Data and schema of created multilayers with buffers are in Figure 2. For

| Material           | Target           |
|--------------------|------------------|
| ZrO <sub>2</sub>   | metallic Zr      |
| YSZ                | sintered ceramic |
| CeO <sub>2</sub>   | sintered ceramic |
| SrTiO <sub>3</sub> | monocrystalline  |

Table 1. Materials and responsible targets used for deposition of epitaxially grown buffer layers.

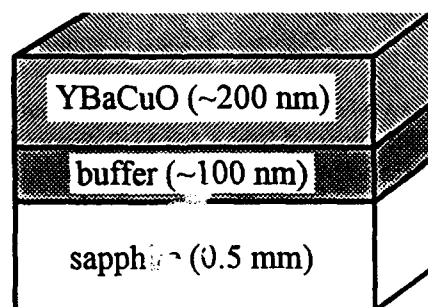


Figure 2. Schema of YBaCuO/buffer/sapphire multilayer

deposition of YSZ and ZrO<sub>2</sub> buffer layers the chamber was evacuated to 1 Pa of oxygen and  $T_s$  in the region of 950°C-980°C<sup>11, 12</sup> was usually maintained. The epitaxial CeO<sub>2</sub> and SrTiO<sub>3</sub> buffer layers were deposited at the similar conditions as for YBaCuO (oxygen pressure = 20Pa,  $T_s$  = 700°C - 720°C). The experimental conditions for deposition of YBaCuO and ferroelectric films are summarized in Table 2. The PZT, PLZT and PMN ferroelectric targets were fabricated

|                                       |                       |
|---------------------------------------|-----------------------|
| Laser                                 | KrF excimer laser     |
| Wavelength                            | 248 nm                |
| Repetition rate                       | 5-20 Hz               |
| Pulse duration                        | 25 ns                 |
| Laser fluence                         | 2-5 J/cm <sup>2</sup> |
| Deposition rate per pulse             | 0.05-0.1 nm           |
| Target-substrate distance             | 5-6 cm                |
| O <sub>2</sub> gas pressure           | 27 Pa                 |
| Substrate temperature: YBaCuO         | 715 °C                |
| Substrate temperature: ferroelectrics | 420-650 °C            |

Table 2. Summary of experimental conditions

with standard ceramic technology. The thickness of YBaCuO layers was typically 100-200 nm for PZT and 40-50 nm for PLZT and PMN heterostructures. Thinner semitransparent or transparent YBaCuO electrodes are needed for electrooptical and optical measurements of transparent ferroelectrics. The thickness of ferroelectric films was 200-500 nm. For electrical characterization, the Ni top electrodes of 8.7x10<sup>-4</sup> cm<sup>2</sup> dimension were magnetron sputtered on the PZT/YBaCuO multilayers at a pressure of 0.6 Pa , and at room substrate temperature. For optical characterization, SnO<sub>2</sub> transparent top electrodes of 28x10<sup>-3</sup> cm<sup>2</sup> dimension were sputtered on PLZT/YBaCuO and PMN/YBaCuO heterostructures at the pressure of 3 Pa and the temperature of ~250°C.

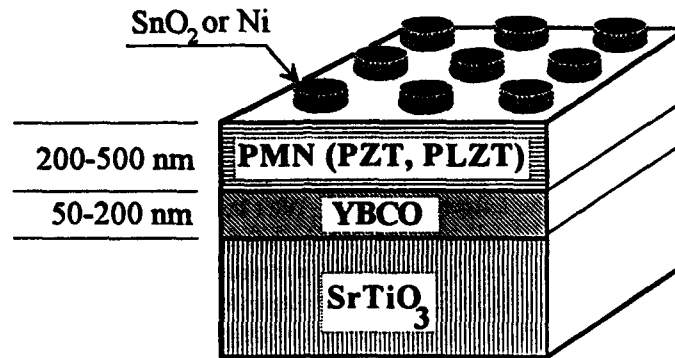


Figure 3. Schema of multilayers with ferroelectric and superconductive films.

Figure 3 shows a schematic of the ferroelectric/superconductor heterostructures. The resulting films were analyzed by means of electrical measurement, the standard Rutherford backscattering spectrometry (RBS), X-ray diffraction (XRD), and scanning electron microscopy (SEM). Capacitance and conductance of ferroelectric films measurement were made over the frequency range of 40 Hz -  $5 \times 10^4$  Hz using an impedance analyzer, and ferroelectric hysteresis studies were carried out with the Sawyer-Tower circuit at 90 Hz at room and liquid nitrogen temperature.

### 3. RESULTS AND DISCUSSION

#### 3.1. Superconductors

Film properties of YBaCuO superconductors were studied by XRD, temperature-resistance  $R(T)$  measurement and SEM. A YBaCuO unit cell is orthorhombic with the longest dimension in  $c$  axis and film orientation is important from application viewpoint. The film orientation, phase purity, and film crystallinity were obtained from XRD. Figure 4 shows a typical  $\Theta$ - $2\Theta$  scan of YBaCuO film deposited on monocrystalline (100)  $\text{NdGaO}_3$  substrate. It is seen that the film with  $c$  unit cell axis is oriented perpendicularly to the plane of the substrate. We can see the presence of (001) Bragg peaks of YBaCuO in addition to those of the substrate. The XRD patterns indicate strong crystallographic alignment of the films.

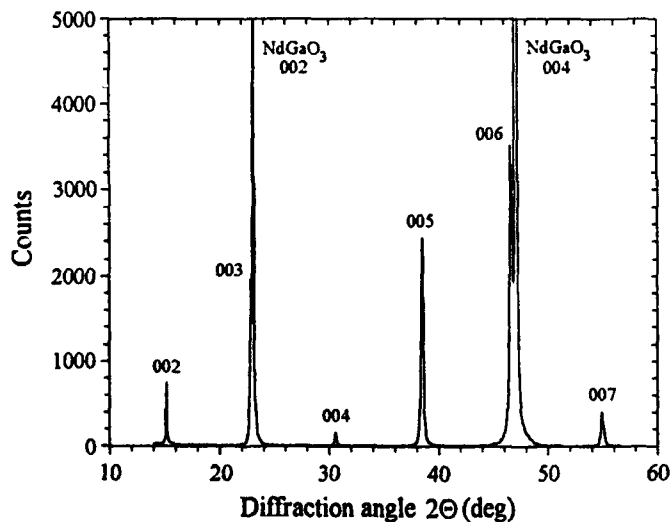


Figure 4. X-ray diffraction pattern for YBaCuO film on (100)  $\text{NdGaO}_3$  substrate

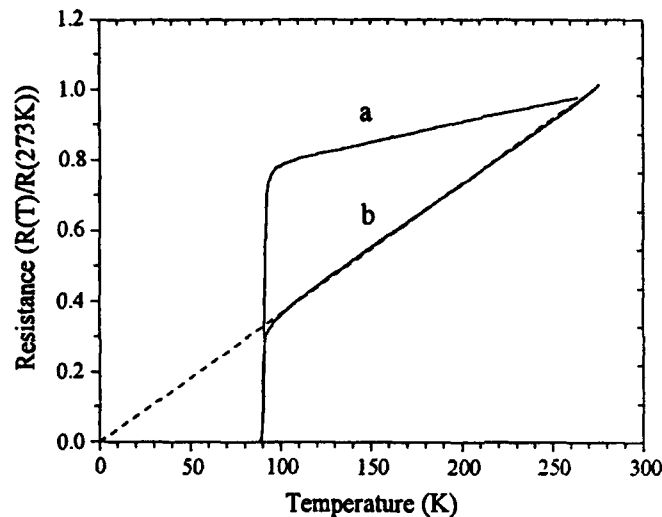


Figure 5.  $R(T)$  dependence for YBaCuO films on (110)  $\text{SrTiO}_3$  (a) and (100)  $\text{SrTiO}_3$  (b)

Figure 5 shows the  $R(T)$  dependence of YBaCuO/(100) $\text{SrTiO}_3$  and YBaCuO/(110) $\text{SrTiO}_3$  films measured by a four-point method. The zero-temperature  $T_c$  of the both layers is high ( $\sim 90\text{K}$ ). It means that film stoichiometry is good. But we can see that behavior of these curves is different in normal state. XRD of these films resulted in conclusion that while layer b contains only YBaCuO with  $c$ -axis perpendicular to substrate, layer a is a mixture of both orientations. It means that resistivity temperature dependence may be used as a measure of the film quality.

For technological applications the sapphire is one of preferred substrates. Unfortunately, sapphire is not compatible with the YBaCuO at the deposition temperature. Diffusion of Al atoms causes strong degradation of superconductive properties, and poor lattice match results in poor film microstructure. The solution of these problems uses the buffer layers. The buffer materials have to be chemically and structurally compatible with both sapphire and YBaCuO. The example of the XRD spectra of  $\text{ZrO}_2$  buffer layer deposited on (1102)sapphire is in Figure 6.

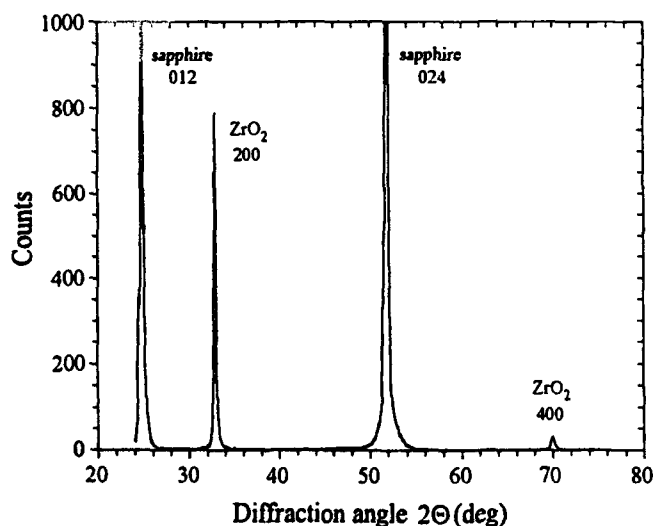


Figure 6. X-ray diffraction pattern for  $\text{ZrO}_2$  buffer layer on (1102) sapphire substrate.

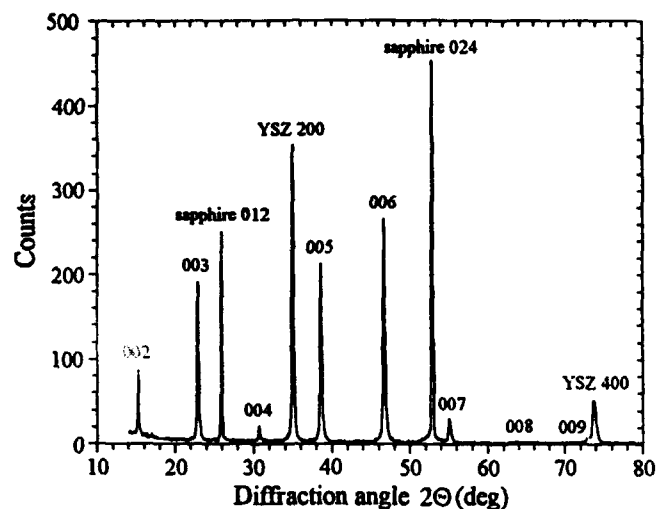


Figure 7. X-ray diffraction pattern for YBaCuO film on YSZ/(1102)sapphire substrate.

The XRD spectra of YSZ are in Figure 7. We see that in the both cases the epitaxially grown buffer layers were created. From  $R(T)$  dependencies (see Figure 8) of YBaCuO/YSZ/(1102)sapphire follows that using buffer layers, the superconductive films of very good quality can be obtained.

Higher  $T_c$  and critical current densities  $J_c$  (77K), were usually measured for YBaCuO layers on monocrystalline SrTiO<sub>3</sub> or NdGaO<sub>3</sub> substrates. But for sapphire coated with ZrO<sub>2</sub> or YSZ buffer layers comparable results were also reached ( $T_c = 89.5$  K,  $J_c$  (77K)  $\approx 1.5 \times 10^6$  Acm<sup>-2</sup>)<sup>12</sup>.

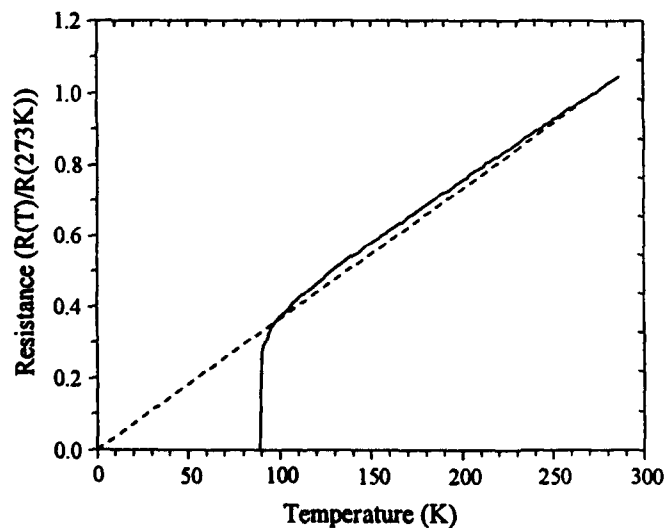


Figure 8.  $R(T)$  dependence for YBaCuO film on YSZ/(1102)sapphire substrate



### 3.2. Ferroelectrics

#### A. PZT

The XRD of laser deposited PZT(0.52, 0.48)/YBaCuO/STO(100) heterostructure is in Figure 9. Only c-axis orientation of both YBaCuO and PZT, in addition to the substrate (h00)<sub>STO</sub> peaks of substrate were grown. The rocking curves full width at half-maximum (FWHM) for the (005)<sub>YBaCuO</sub> and (200)<sub>PZT</sub> were in the range of 0.4°-0.6° and 0.8°-1°, respectively.

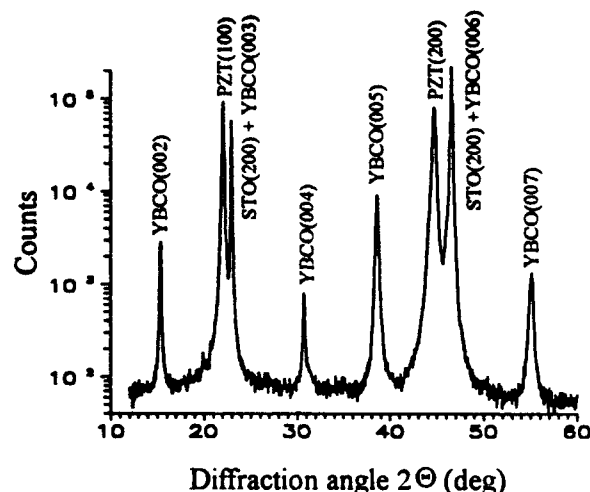


Figure 9. XRD patterns of PZT/YBCO/(100)SrTiO<sub>3</sub> heterostructure (PZT film was deposited at the temperature of 550 °C).

Figure 10 shows hysteresis loops of multilayer ferroelectric system of Ni/PZT(0.52, 0.48)/YBaCuO/(100)SrTiO<sub>3</sub> for room and liquid nitrogen temperatures. The hysteresis data were obtained at 90 Hz and an applied bias of 15 V. The hysteresis loops obtained from the epitaxial PZT were asymmetric due to an internal bias field. The internal bias field was estimated to be approximately 15 kVcm<sup>-1</sup>. The hysteresis remanence of the PZT(0.52, 0.48) and PZT(0.75, 0.25) films deposited at the same temperature was approximately 42 μCcm<sup>-2</sup> and 24 μCcm<sup>-2</sup> with a coercive field estimated at 55 kVcm<sup>-1</sup> and 80 kVcm<sup>-1</sup>.

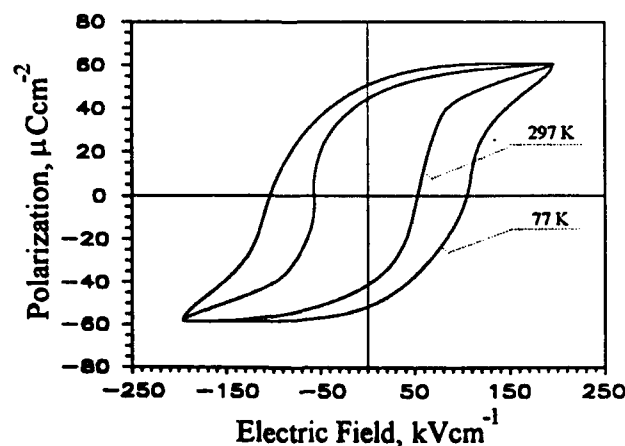


Figure 10. The dielectric hysteresis loops of the PZT(0.52, 0.48) film grown on YBaCuO/(100)SrTiO<sub>3</sub> structure, at room and liquid nitrogen temperature (PZT film thickness 500 nm).

For our best-quality heterostructure, a drop of the Pr value smaller than 20% was observed after about  $10^9$  cycles of polarization switching. The resistivities of the films were in the range of  $3\text{--}8 \times 10^9 \Omega\text{cm}$ . The dielectric constant of the PZT films of  $0.5 \mu\text{m}$  thickness was about 960 at 1 kHz measuring frequency.<sup>11</sup>

## B. PLZT and PMN

The diffractogram of the laser deposited PLZT/YBaCuO/(110)SrTiO<sub>3</sub> heterostructure (Figure 11) indicate that the PLZT film exhibited a perovskite structure with orientation (110). No impurity lines were detected. The YBaCuO peaks with orientation (hk0) are hidden due to the small thickness of the YBaCuO film (40 nm).

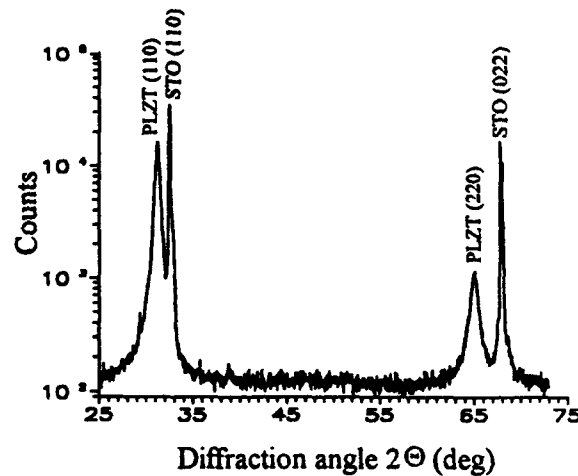


Figure 11. XRD patterns of PLZT/YBaCuO/(110)SrTiO<sub>3</sub> heterostructure (PLZT film was deposited at the temperature of 520 °C).

The XRD patterns of ferroelectric/superconductor heterostructure of PMN/YBaCuO/(100)SrTiO<sub>3</sub> are shown in Figure 13. Only (00l) peaks for YBaCuO were measured, the PMN film has preferential (00l) orientation with a small amount of pyrochlore phase.

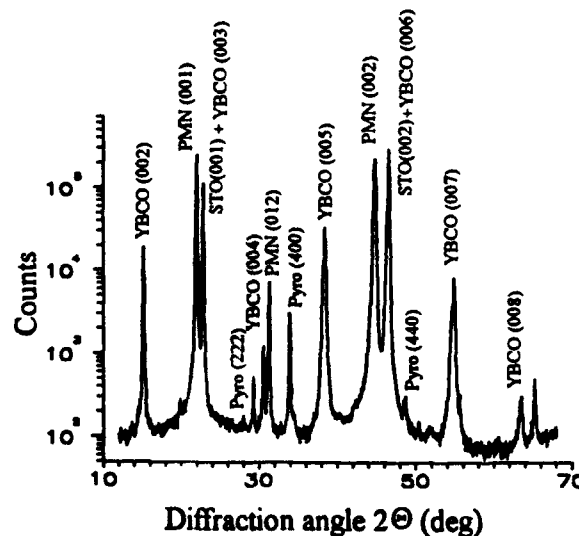


Figure 12. XRD patterns of PMN/YBCO/(100)SrTiO<sub>3</sub> heterostructure (PMN film was deposited at the temperature of 550 °C).

The XRD spectra of PLD deposited PMN on (110)SrTiO<sub>3</sub> for different deposition temperatures are in Figure 12. The pure perovskite-like phase was grown only at the temperature of deposition of about 550 °C. For lower temperatures there arises a mixture of perovskite phase with preferential orientation (110) and pyrochlore with dominant texture (100). The pyrochlore (nonferroelectric) structure arises due to the low migration energy of particles deposited on the substrate surface during the growth of a film. A higher substrate temperature provided higher mobility for ejected species, and they could thus relax to lower energy sites; therefore, the proportion of perovskite phase increases with an increase of deposition temperature. A polycrystalline pyrochlore phase was formed for deposition temperature over 600 °C due to reevaporation of volatile Pb from growing layer. loss of volatile Pb in a layer. From the RBS analysis it follows that the stoichiometry of the PMN surface layer was the same as that of the PMN target for deposition temperature lower than 570 °C. The composition of PMN films deposited at a temperature of 610°C was estimated by the RBS analysis to Pb<sub>1.42</sub>Mg<sub>1.04</sub>Nb<sub>1.8</sub>O<sub>6</sub>, which is conform to pyrochlore PMN structure with Pb deficiency.

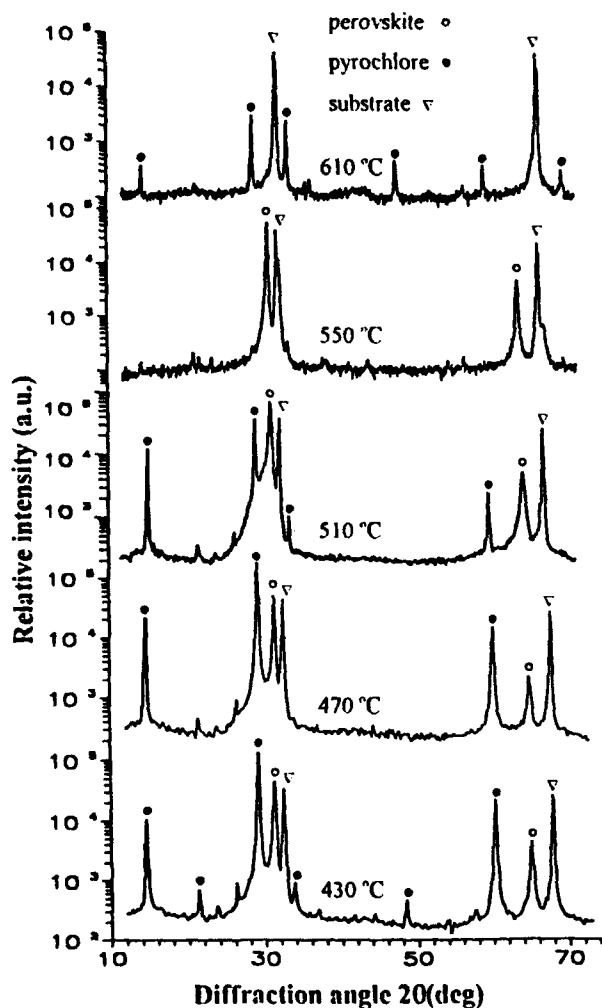


FIGURE 13. XRD patterns of PMN/(110)SrTiO<sub>3</sub> structure for different deposition temperatures.

#### 4. CONCLUSION

In summary, thin YBaCuO superconductive and ferroelectric films of PZT, PLZT, PMN, buffer layers and multilayer systems have been successfully grown by the laser ablation technique on crystalline NdGaO<sub>3</sub>, (100)SrTiO<sub>3</sub>, (110)SrTiO<sub>3</sub>, and on technological substrates. The high-quality ferroelectric films were deposited on epitaxial YBaCuO layers prepared also by pulsed laser ablation. The pure ferroelectric phase of PZT, PLZT, and PMN was grown only in a narrow window of deposition parameters. The most important parameters are the substrate temperature and the oxygen deposition pressure; therefore, film composition was extremely sensitive to these parameters. In a oxygen ambient of 27 Pa the optimum deposition temperatures of 550°C, 520 °C, and 550 °C was found for PZT, PLZT, and PMN, respectively. XRD studies of the PZT/YBaCuO show that the layers grow in the c-axis orientation, with a rocking angle - (FWHM) for the (005)<sub>YBaCuO</sub> and (200)<sub>PZT</sub> reflections in the range of 0.4°-0.6° and 0.8°-1°, respectively. The remanent polarization and coercive fields of the PZT(0.52, 0.48) film were 42 μCcm<sup>-2</sup> and 55 kVcm<sup>-1</sup>, and for PZT(0.75, 0.25) the value of 24 μCcm<sup>-2</sup> and 30 kVcm<sup>-1</sup> were reached.

From the experiments follows, that PLD is a very powerful method for creation of different multilayered systems. Because the deposition time is very short and there is no problem with the change of the targets during the deposition, the PLD is a very suitable tool mainly for fast laboratory experiments. The disadvantage of this method are in droplets which occurred on the surface of created films. The droplets on bottom layer "prick" upper layer and such a short connection has influenced the quality of electric parameters of the whole multilayer system. From our experimental experiences follows that the density of the droplets in YBaCuO layer was much higher in comparison with that in buffer or ferroelectric films. Using special deposition configuration it is possible to decrease the YBaCuO droplets density to about 10<sup>4</sup> cm<sup>-2</sup>.<sup>14</sup>

#### 5. ACKNOWLEDGMENT

The authors wish to thank V. Studnička, R. Černý, and M. Chládek for their technical assistance in XRD measurement. This work was supported by the Grant Agency of Czech Republic under grant No. 202/93/0464.

#### 6. REFERENCES

1. X.D. Wu, R.E. Muechenhausen, N.S. Nogar, A. Pique, R. Edwards, B. Wilkens, T.S. Ravi, D.M. Hwang, and C.Y. Chen, "Epitaxial yttria-stabilized zirconia on (1102) sapphire for YBaCuO", *Appl. Phys. Lett.*, 58, p. 304, 1991.
2. S.L. Swartz and V.E. Wood, "Ferroelectric thin films", *Cond. Matter News*, 1, p. 4, 1992.
3. G.H. Haertling, "Recent developments in bulk and thin film PLZT materials and devices", *Ferroelectrics*, 131, p. 1, 1992.
4. D. Roy and S.B. Krupanidhi, "Pulsed excimer laser deposition and characterization of ferroelectric Pb(Zr<sub>0.52</sub>Ti<sub>0.48</sub>)O<sub>3</sub> thin films", *J. Mater. Res.*, 7, p. 2521, 1992.
5. S.B. Krupanidhi, N. Maffei, D. Roy, and C.J. Peng, "Growth of ferroelectric oxide thin films by excimer laser ablation", *J. Vac. Sci. Technol.*, A 10, p. 1815, 1992.
6. S.G. Ghone, E. Goo, R. Ramesh, T. Sands, and V.G. Keramidas, "Microstructure of epitaxial La<sub>0.5</sub>Sr<sub>0.5</sub>CoO<sub>3</sub>/ferroelectric Pb<sub>0.9</sub>La<sub>0.1</sub>(Zr<sub>0.2</sub>Ti<sub>0.8</sub>)<sub>0.975</sub>O/La<sub>0.5</sub>Sr<sub>0.5</sub>CoO<sub>3</sub> heterostructures on LaAlO<sub>3</sub>", *Appl. Phys. Lett.*, 63, p. 1628, 1993.
7. H. Tabata, T. Kawai, S. Kawai, O. Murata, J. Fujioka, and S. Minakata, "Preparation of PbTiO<sub>3</sub> thin films at low temperature by an excimer laser ablation technique", *Appl. Phys. Lett.*, 59, p. 2354, 1991.
8. W. Jo, G-C. Yi, T.W. Noh, Y.S. Cho, and S-I. Kwun, "Structural and electro-optic properties of laser ablated Bi<sub>4</sub>Ti<sub>3</sub>O<sub>12</sub> thin films on SrTiO<sub>3</sub>(100) and SrTiO<sub>3</sub>(110)", *Appl. Phys. Lett.* 61, p. 1516, 1992.
9. Y. Shibata, K. Kaya, K. Akashi, M. Kanai, T. Kawai, and S. Kawai, "Epitaxial growth of LiNbO<sub>3</sub> films on sapphire substrates by excimer laser ablation method and their surface acoustic wave properties", *Jpn. J. Appl. Phys.*, 32, p. L745, 1993.
10. R. Ramesh, A. Inam, W.K. Chan, B. Wilkens, K. Myers, K. Remschnig, D.L. Hart, and J.M. Tarascon, "Epitaxial cuprate superconductor/ferroelectric heterostructures", *Science*, 252, p. 944, 1991.
11. M. Jelinek, L. Jastrabik, V. Olšan, L. Soukup, M. Šimečková, R. Černý, E.B. Kluevov, and L. Mazo, "Laser deposited YBaCuO thin films", p. 661, *Czech. J. Phys.*, 43, 1993.
12. A.J. Basovich, S.V. Gaponov, L. Jastrabik, M. Jelinek, N.A. Kiselev, E.B. Kluevov, O.I. Lebedev, L.A. Mazo, L. Soukup, M.D. Strikovskij, V.V. Talanov, and A.L. Vasiliev, "Laser deposition of Y-Ba-Cu-O on ZrO<sub>2</sub> coated sapphire substrates", *Thin Solid Films*, 228, p. 193, 1993.
13. M. Jelinek, J. Brádler, V. Trtík, L. Soukup, S.V. Gaponov, L.A. Suslov, E.B. Kluevov, Y. N. Drozdov, T.A. Shaplygina, and V.A. Trepakov, "Preparation and investigation of laser ablated PZT, PLZT, and PMN ferroelectric films", The Eight International Meeting on Ferroelectricity, Gaithersburg, MA, USA, August 1993. Abstract book p. 39. Full text will be published in *Ferroelectrics*.
14. S. Gaponov, J. Gavrilov, M. Jelinek, E. Kluevov, and L. Mazo, "YBaCuO and ZrO<sub>2</sub> laser deposition on sapphire using two crossed beams", *Supercond. Sci. Technol.*, 5, p. 645, 1992.